EXPERIMENTAL STUDY OF GEODESIC ACOUSTIC MODE IN THE STOR-M TOKAMAK

A Thesis Submitted to
the College of Graduate Studies and Research
in Partial Fulfilment of the Requirements
for Master of Science
In the Department of Physics and Engineering Physics
University of Saskatchewan
Saskatoon

By
Masaru Nakajima

Permission to Use

In presenting this thesis in partial fulfilment of the requirements for a Postgraduate degree from the University of Saskatchewan, I agree that the Libraries of this University may make it freely available for inspection. I further agree that permission for copying of this thesis in any manner, in whole or in part, for scholarly purposes may be granted by the professor or professors who supervised my thesis work or, in their absence, by the Head of the Department or the Dean of the College in which my thesis work was done. It is understood that any copying or publication or use of this thesis or parts thereof for financial gain shall not be allowed without my written permission. It is also understood that due recognition shall be given to me and to the University of Saskatchewan in any scholarly use which may be made of any material in my thesis.

Requests for permission to copy or to make other use of material in this thesis in whole or part should be addressed to:

Head of the Department of Physics and Engineering Physics
116 Science Place
University of Saskatchewan
Saskatoon, Saskatchewan
S7N 5E2

To my parents

Abstract

In this experimental study, we used a set of Langmuir probes in order to observe geodesic acoustic mode (GAM) in plasmas created in the STOR-M tokamak. At four locations of STOR-M, we measured floating potential and ion saturation current. Around 9 ms into the discharge, the end of ramp-up region and the beginning of the flat-top region, we found a dominant peak around 30 kHz in the power spectral densities of ion saturation current. The ion saturation current signals showed the $sin\theta$ dependence of the oscillation amplitude, which is one of the characteristics of GAM. Furthermore, the cross spectral analysis on the ion saturation current signals suggested the poloidal mode number of $m = 1$. As for the floating potential signals, while 30 kHz peak was present around 9 ms, the cross spectral analysis indicated the poloidal mode number of $m = 1$, which is not expected for GAM. In comparison to the theoretical calculations of GAM frequency, the frequency predicted by the fluid model matched with the experimental results. Based on the above findings, it is concluded that the plasmas in the STOR-M tokamak have a signature of GAM.

Acknowledgements

First and foremost, I would like to express my sincere gratitude to my supervisor Professor Akira Hirose for his guidance, support, and encouragement. I learned not only from his deep knowledge in plasma physics and keen insights, but also from his ever-seeking attitude toward physics. His leadership, generous and humorous, showed me the capacity I should seek to have. The advice, "An experimentalist must always be ready show the data", is one of the many important pieces of guidance I received from Professor Hirose. It was truly a privilege to study under his supervision.

I would also like to show my appreciation for Dr. Debjyoti Basu, who acted as an informal supervisor and guided me in all the practical matters regarding my thesis work. Ranging from experimental ideas to data analysis, I received from him an invaluable training in experimental plasma physics.

My appreciation also goes to Professor Chijin Xiao, who has taught me the basics of plasma diagnostics and provided helpful advice and guidance for my thesis work. I would like to thank Dr. Takumi Onchi for the training in electronics, which formed the basis for my skills in developing electronic circuits for the experiment. Technical assistance provided by Mr. David McColl, Ms. Jiping Zhang, and the Physics Machine Shop staff has been highly instrumental. Lastly but not least, I like to thank my fellow graduate students, Akbar Rohollahi, Adedapo "Joseph" Adegun, Gregory Tomney, Ekow Lewis, Reza Behbahani, Michael Patterson, and post-doctoral fellow Dr. Sayf Elgriw, for their support, discussions, and friendship.

Contents

List of Tables

List of Figures

List of Abbreviations

GAM	Geodesic Acoustic Mode
STOR-M	Saskatchewan Torus Modified
GUI	Graphical User Interface

Chapter 1

Introduction

Energy is indispensable in today's human life. From a single home to a large-scale factory, energy is consumed through various processes such as light, mechanical work, heat, etc. One of the major ways to distribute energy is electricity, in which electrical power is provided through metallic wires. Today, different methods are being developed for sustainable electricity generation in terms of source reserve and effect on the environment. Nuclear fusion energy is one such method, as it does not produce carbon dioxide and is safer, at least in principle, than the conventional nuclear fission energy. As any other energy source, however, nuclear fusion energy has drawbacks. One of the major problems is the shear difficulty of making the fusion reaction happen in a controllable way. In order to overcome this challenge, the behaviour of plasma, ionized gas in which fusion reaction can occur, needs to be understood. This thesis work involves experiments conducted in attempt to enhance the knowledge of so-called magnetically confined plasmas created in laboratories. This chapter provides the motivation, the scope, and the purpose of the research and the outline of the thesis.

1.1 Need for Alternative Energies

The last couple of decades have seen a rapid economic growth around the world. Accompanying this growth were increased energy consumptions in industry, transportation, agriculture and residences. The world's energy consumption in 2012 was twice as that in

1973, which was 4,672 million tons toil equivalent (Mtoe) [1]. This growing energy demand has been supported primarily by natural resources such as coal, oil and natural gas. In 2012, over 80% of the world energy supply was provided by the above fossil fuels [1]. The heavy dependence on the carbon-based energy sources has two major problems.

The first problem is that the fossil fuels are not renewable, and their reserves limited. As of 2014, the reserve-to-production ratios of oil, coal and naturals gas were estimated to be 80, 164 and 59 years, respectively [2]. This simple fact indicates that the current way of producing energy is not sustainable in the long run. Moreover, since reserve-to-production ratio is defined as the ratio of the total reserve to the usage per year, increasing use of the fuels can lead to earlier depletion.

The second problem, and perhaps the more serious one, is the effect of use of fossil fuels on earth's climate. Earth's atmosphere both absorbs and reflects radiation, which keeps the planet's temperature higher than it would be if there were no atmosphere. Gases responsible for this effect, i.e. greenhouse effect, include water vapour, carbon dioxide, methane, etc. While greenhouse effect is necessary for keeping the earth's temperature moderate, changes in the contents of greenhouse gases can cause global climate change. It has been reported that the earth's surface temperature has successively increasing over the past three decades, and the average temperature is likely the highest among the last 1400 years [3]. One of the major factors for this effect is believed to be emission of greenhouse gases such as CO_2. The total anthropogenic CO_2 emission in 2011 (26 Gt) was nearly 4 times as high as that in 1950, and 25% percent was attributed to electricity and heat production [3]. Today, efforts are being made on coming up with alternative energies in order to have energy supplies sustainable both in terms of reserve and environment.

1.2 Nuclear Fusion Energy

One of the energy solutions is nuclear fusion energy. Nuclear fusion is a reaction in which two lighter nuclei collide and fuse into a heavier nucleus. The decrease in the total mass before and after the reaction is manifested as the kinetic energies of the products. The radiations from the Sun originate from the fusion occurring near its core. The reaction starts with:

$$p + p \rightarrow {}^{2}He + e^{+} + \nu_e + 0.42MeV, \tag{1.2.1}$$

and fusion reactions continue to make helium as an end product. The above reaction, however, has a cross section of order 10^{-47} cm^2, which makes it difficult to occur in laboratories on earth [4]. One of the candidate pairs for terrestrial fusion reaction is of deuterium and tritium,

$$d + t \rightarrow {}^{4}H + n + \ 17.5MeV, \tag{1.2.2}$$

for the relatively high pair reaction rate and output energy per reaction [4]. In Eq. 1.2.2, most of the kinetic energy is carried by the neutron, which will be absorbed by the surrounding structure to convert it into thermal energy. If made possible, fusion energy would be one of the ideal sources of energy for its attractive characteristics.

First of all, the waste product of fusion energy would be clean. In the reaction describe in Eq. 1.2.2, the end products are a neutron and a helium atom, which are stable and inert. Moreover, the radioactive waste of fusion energy would be short-lived compared to those from fission reactions. As neutrons hit the surrounding structure, it becomes radioactive, and therefore the structure must be disposed properly after replacing or decommissioning. However, the half-life of such radioactive materials would be about 50 - 100 years, while those of fission reactions are thousands of years [5]. The fusion energy would thus overcome the problems in fossil fuels and nuclear fission energy.

The second advantage of fusion energy is its safety. One of the most serious problems of fission reactors is its safety. Normal fission reactors contain fuel rods with fissionable materials for about three years of operational lifetime [6]. If the control of the fission reactions is disrupted by accidents or natural disasters, fission reactions can trigger other fission reactions in an uncontrolled manner, leading to a chain reaction. The consequence can be devastating, as seen in the accidents in Three Mile Island (1979), Chenobyl (1986), and Fukushima (2011) [7]. In contrast, in a fusion reactor, fuels must be fed constantly at a certain rate and the temperature kept high enough in order for the fusion reaction to be sustained. Therefore, in case of emergency or power shut down, the fusion reaction would simply halt. Therefore, fusion reactors can also provide electricity with higher safety than nuclear fission reactors.

The last major advantage of fusion energy is the energy gain and the abundance of fuel on earth. For the d-t reaction, 140 kg of fuel can produce energy equivalent to burning 10^6 tons of oil [8]. Deuterium is abundant on earth and readily available in, for example, ocean. Tritium, which is extremely scarce in nature, has to be provided from lithium, whose reserve is abundant. With today's energy consumption, Li^6 reserve is in the order of 20,000 years if used in d-t fusion. If d-d reaction is made, possible deuterium's reserve would amount to 2 billion years [8]. Fusion energy can be a clean, safe, and long-term energy source on earth.

1.3 Tokamak

In order for positively charged nuclei to fuse, they need to collide with enough energy to overcome the repulsive Coulomb potential between them. For d-t reaction, the optimal temperature is about 10^8 K. At this temperature, gas becomes ionized in a state of plasma. Fusion reaction involving high temperature gas is called thermonuclear fusion. In addition to the requirement for the temperature, fuels need to be in the vicinity of each other for long enough period of time. These requirements are expressed as $n\tau_E T$, where n is the number density, τ_E is the energy confinement time, and T the temperature of plasma. For a self-sustained d-t reaction, the criterion for the triple product is [9]:

$$n\tau_E T > 5 \times 10^{21} m^{-3} sKeV. \tag{1.3.1}$$

One of the major challenges in thermonuclear fusion is confining a hot plasma so as to meet the above criteria.

One of the promising devices for sustaining thermonuclear reaction is tokamak. Tokamak, a Russian acronym for *toroidal chamber with magnetic coils*, is a toroidal device which uses magnetic fields to confine a plasma. Since its invention by Artsimovich in the 1950's, tokamak devices around the world have been producing plasmas with improving parameters. Fig. 1.1 shows the progress in tokamak devices in terms of the triple product. The world record of fusion power output of 18 MW (65 % of the input power) was set by JET in Culham in 1997 [11]. Today (2015), a multinational tokamak project, International Thermonuclear Experimental Reactor (ITER), is under construction with the aim of burning d-t plasma and producing 500 MW with 50 MW input [12].

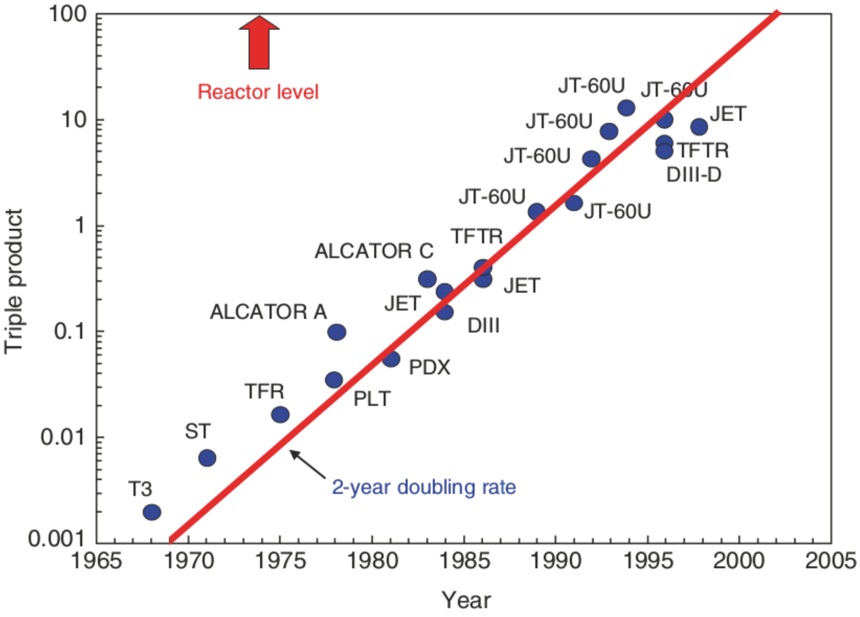

Figure 1.1: Progress in tokamak devices by the triple product (in $10^{20} m^{-3}\ keV\ s$). Points are labelled with corresponding device names. Figure was taken from [10].

1.4 Challenges in Fusion

Despite the steady improvements in plasma confinement in tokamaks, there still remain challenges to be tackled. One of the main challenges is to minimize the transport of plasma to the surrounding structure. Classical theories predict some causes for a plasma to escape the magnetic confinement such as the toroidal geometry of tokamak. Methods have been developed to suppress the loss. However, experiments have shown that the rate of loss much higher than that predicted by the classical theories [10]. The dominant plasma transport out of the confinement turned out to be turbulence, or nonlinear effects which are difficult to predict. There are many instabilities in plasmas which can cause turbulence, which can in turn lead to other instabilities. Understanding the dynamics and relationships of instabilities and turbulence is crucial for improving the confinement and thus a topic of active research today [13].

One of the phenomena which turbulence can cause is geodesic acoustic mode (GAM). According to its original prediction ([14]), GAM is an electrostatic oscillation due to toroidal geometry. First predicted in theory, the observations of GAM in toroidal devices such as tokamak led scientists to study its behavior [15]. Today, both theoretical and experimental efforts are being made for understanding its relationship to turbulence and other oscillations in toroidal plasmas. Such studies are crucial as they shed light on turbulence in plasmas, which in turn can help design a better system for harnessing nuclear fusion energy.

1.5 Purpose of the Study

The purpose of this study is to add to the research on GAM. For this purpose, we conducted an experiment with the tokamak situated in University of Saskatchewan. The aim of the experiment was first to observe GAM in the tokamak, as its existence had not been confirmed for this machine. The second goal of the experiment was to study the characteristics of GAM. We spent fair amount of time on developing devices necessary for conducting the experiment. Such devices are reported in this thesis in addition to the experiment.

1.6 Thesis Outline

In this section the motivation for fusion energy and the purpose of our study were introduced. Chapter 2 contains the review of the basic plasma physics. In Chapter 3 the physics related to plasmas in tokamaks is reviewed. Chapter 4 contains the discussion on turbulence in plasmas, the previously developed derivation of GAM frequency and previous experimental studies on GAM. In Chapter 5 the description of STOR-M, the tokamak in Plasma Physics Laboratory at University of Saskatchewan, is given. Chapter 6 contains the review of the basic principles of plasma diagnostics used in the experiment. In Chapter 7 a review on the data analysis methods used to interpret the experimental data is given. Chapter 8 contains the introduction to the devices developed to carry out the experiment. Chapter 9 contains the description of the experimental set up for GAM study in STOR-M. The results of the experiment are given in Chapter 10. Chapter 11 contains the summary of the results and draws conclusions from the experimental results.

Chapter 2

Basic Plasma Physics

In order for fusion to occur, atomic nuclei need to collide with enough energy to overcome the Coulomb repulsion. Furthermore, for commercial use of nuclear fusion for generating electricity, there has to be many nuclear reactions happening. This means that a collection of particles needs to have high temperature. At temperatures high enough for nuclear fusion, most atoms are ionized, and this state is called plasma. This chapter reviews the definition of plasma and a basic physical model to describe the nature of plasma.

2.1 Definition of Plasma

A plasma is a partially or fully ionized gas that has certain properties. One of such characteristics is Debye shielding. In an isotropic plasma, an electrical potential created by a stationary point charge decays exponentially in space. The characteristic length of the shielding is called Debye length, denoted by λ_D, and given by :

$$\lambda_D = \sqrt{\frac{\epsilon_0 k_B T}{ne^2}} \tag{2.1.1}$$

where ϵ_0 is permittivity of free space, k_B Boltzmann constant, T electron temperature, n the equilibrium ion or electron density, and e the electronic charge.

Another property of a plasma is that it exerts a restoring force on a charged particle displaced from its equilibrium, causing it to oscillate. The frequency at which electrons oscillate due to this mechanism is called plasma frequency, ω_p, and given as:

$$\omega_p = \sqrt{\frac{ne^2}{m_e \epsilon_0}} \tag{2.1.2}$$

where m_e is the electron mass. The characteristic time required to restore displaced electrons is then $\tau_p = 1/\omega_p$.

The two properties thus described demonstrate that a plasma tends to arrange itself such that the charges appear neutral when averaged in volume λ_D^3 and in time τ_p. For this mechanism plasmas are said to be "quasi-neutral". In order for an ionized gas to have quasi-neutrality, the characteristic length L and the characteristic time T of the macroscopic properties need to be larger than λ_D and τ_p, respectively. Here, the characteristics length L is defined as the distance over which a physical property, such as magnetic field (B), varies in space, i.e., $L = \frac{dB/dx}{B}$. Lastly, the number of particles in a sphere of radius λ_D, given by $N_D = \frac{4\pi}{3} n {\lambda_D}^3$, must be large so that the collective arrangement of shielding can take place. Thus, the characteristics of a plasma are:

$$\begin{cases} L & \gg \lambda_D \ , \\ T & \gg \tau_p \ \text{ and,} \\ N_D & \gg 1 \ . \end{cases} \tag{2.1.3}$$

In words, a plasma is a quasi-neutral gas of charged and neutral particles which exhibits collective behavior [16].

2.2 Ideal Magnetohydrodynamics

One of the simplest models to describe plasma dynamics is the ideal magnetohydrodynamics (MHD) model. The ideal MHD model treats a plasma as single perfectly conducting fluid ($\sigma = \infty$). This is done by defining the density as:

$$\rho \equiv n_i m_i + n_e m_e \simeq n m_i \tag{2.2.1}$$

where n_i and n_e are the number densities of ions and electrons, respectively. This approximation is valid for a plasma with single-charged ions. Accordingly, the fluid velocity, the current density and the pressure are defined as follows:

$$\mathbf{v} \equiv \frac{1}{\rho}\left(n_i m_i \mathbf{v_i} + n_e m_e \mathbf{v_e}\right) \simeq \frac{m_i \mathbf{v_i} + m_e \mathbf{v_e}}{m_i + m_e} \tag{2.2.2}$$

$$\mathbf{j} \equiv e(n_i \mathbf{v_i} - n_e \mathbf{v_e}) \simeq ne(\mathbf{v_i} - \mathbf{v_e}) \tag{2.2.3}$$

$$p = p_i + p_e. \tag{2.2.4}$$

With the parameters thus defined, the ideal MHD is described by the following equations:

$$\text{Continuity equation} \quad \frac{\partial \rho}{\partial t} + \nabla \cdot (\rho \mathbf{v}) = 0 \tag{2.2.5}$$

$$\text{Equation of motion} \quad \rho\left(\frac{\partial \mathbf{v}}{\partial t} + \mathbf{v} \cdot \nabla \mathbf{v}\right) = -\nabla p + \mathbf{j} \times \mathbf{B} \tag{2.2.6}$$

$$\text{Equation of state} \quad \frac{d}{dt}\left(\frac{p}{\rho^\gamma}\right) \equiv \left(\frac{\partial}{\partial t} + \mathbf{v} \cdot \nabla\right)\frac{p}{\rho^\gamma} = 0 \tag{2.2.7}$$

$$\text{Faraday's law} \quad \nabla \times \mathbf{E} = -\frac{\partial \mathbf{B}}{\partial t} \tag{2.2.8}$$

$$\text{Ampere's law} \quad \nabla \times \mathbf{B} = \mu_0 \mathbf{j} \tag{2.2.9}$$

$$\text{Ohm's law} \quad \mathbf{E} + \mathbf{v} \times \mathbf{B} = 0 \tag{2.2.10}$$

Here, **B** and **E** are the magnetic and electric fields, respectively. Eq. 2.2.5 is the continuity equation. In the momentum equation (Eq. 2.2.6), the viscosity term was ignored, assuming that the characteristic frequency ($\sim 1/T$) is larger than the ion collision frequency ν_i. The ideal MHD also assumes adiabatic process (Eq. 2.2.7). Eqs. 2.2.8 and 2.2.9 are Maxwell's equations with an assumption that the rate of change in the electric field is small. This is equivalent to assuming $L/T \ll c$, where c is the speed of light. Lastly, Ohm's law (Eq. 2.2.10) results from a set of assumptions, i.e.,

$$L \gg \frac{c}{\omega_p} \tag{2.2.11}$$

$$T \gg \frac{1}{\omega_{ci}} \tag{2.2.12}$$

$$R_m \equiv \mu_0 \sigma v L \gg 1. \tag{2.2.13}$$

Here, ω_{ce} and σ are the electron cyclotron frequency and the conductivity, respectively, and R_m is called the Magnetic Reynold's number. The approximations in Ohm's law are what make the MHD model ”ideal”[17].

2.3 MHD Equilibrium

In the MHD theory, an equilibrium state is characterized with $\partial/\partial t = 0$ and $\mathbf{v} = 0$. Under this condition, Eq. 2.2.6 becomes;

$$\nabla p = \mathbf{j} \times \mathbf{B} \tag{2.3.1}$$

This equation is called the force balance equation. To interpret the equation, consider a cylindrical column of plasma, as shown in Fig. 2.1. Let ∇p be in the radial direction. Given a magnetic field in the axial direction, current must flow in the azimuthal direction to cancel the gradient force. Such current is called the diamagnetic current. Using Eq. 2.2.9, Eq. 2.3.1

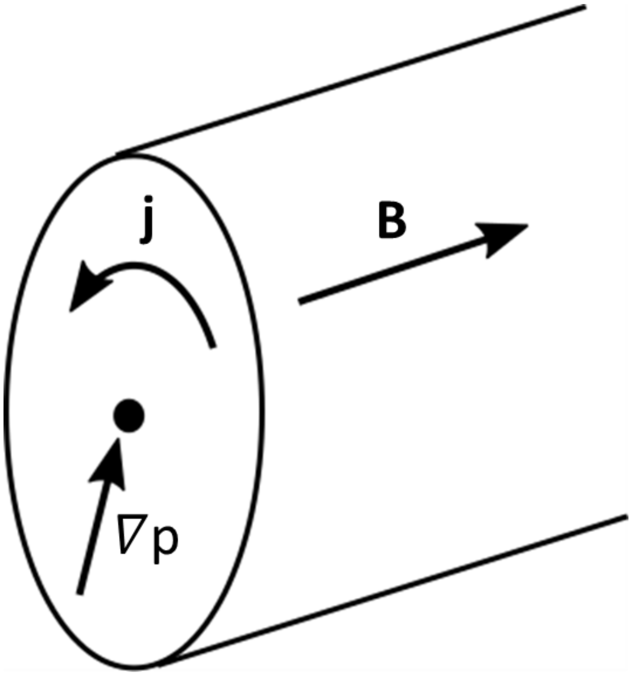

Figure 2.1: Cylindrical column of plasma in equilibrium

can be rewritten as,

$$
\begin{aligned}
\nabla p &= \mathbf{j} \times \mathbf{B} \\
&= \mu_0^{-1}(\nabla \times \mathbf{B}) \times \mathbf{B} \\
&= \mu_0^{-1}[(\mathbf{B} \cdot \nabla)\mathbf{B} - \frac{1}{2}\nabla B^2] \\
\nabla(p + \frac{B^2}{2\mu_0}) &= \frac{1}{\mu_0}(\mathbf{B} \cdot \nabla)\mathbf{B} \\
\nabla(p + \frac{B^2}{2\mu_0}) &= 0 \ .
\end{aligned}
$$

Here, $(\mathbf{B} \cdot \nabla)\mathbf{B} = 0$ by the assumption of zero curvature in $\mathbf{B}$. Therefore, an equilibrium in this case is characterised as

$$p + \frac{B^2}{\mu_0} = \text{constant} \tag{2.3.2}$$

The above equation indicates that the magnetic field must decrease toward the cylinder axis because the pressure increases toward the centre. The decrease in the magnetic field is due to the diamagnetic current, and this reduction effect is characterized by the ratio

$$\beta = \frac{p}{B^2/2\mu_0} = \frac{\text{particle pressure}}{\text{magnetic pressure}} \tag{2.3.3}$$

In magnetically confined plasmas for fusion application, β is a measure of the energy confined per the externally applied magnetic field [18].

Chapter 3

Tokamak Physics

Tokamak is a torus-shaped system for confining plasma by magnetic fields. The performance of tokamak in confining plasma has made it one of the promising candidates for the future nuclear reactors. This chapter reviews the physics of plasma confinement in tokamak devices.

3.1 Tokamak Configuration

A tokamak is a configuration with a torus, or doughnut-shaped chamber (Fig. 3.1). A current flows through the coils to create a magnetic field, or toroidal magnetic field (B_t), around the torus. The plasma current (I_p) in the toroidal direction is induced by a transformer action, with the plasma acting as the secondary coil. The plasma current in turn produces magnetic fields which encircle the plasma current. This is called the poloidal magnetic field (B_p). The resulting total magnetic field has a helical shape surrounding the plasma.

Fig. 3.2 shows a cross sectional view of a poloidal plane of plasma column contained in a tokamak. The ratio of the major radius, R_0, and the minor radius, r, is called the aspect ratio. Due to the toroidal geometry, magnetic field closer to the major axis is stronger than that farther from the major axis. This inhomogeneity creates a force which tends to push the plasma outwards. In order to compensate for this force and keep the equilibrium, a vertical magnetic field must be applied externally.

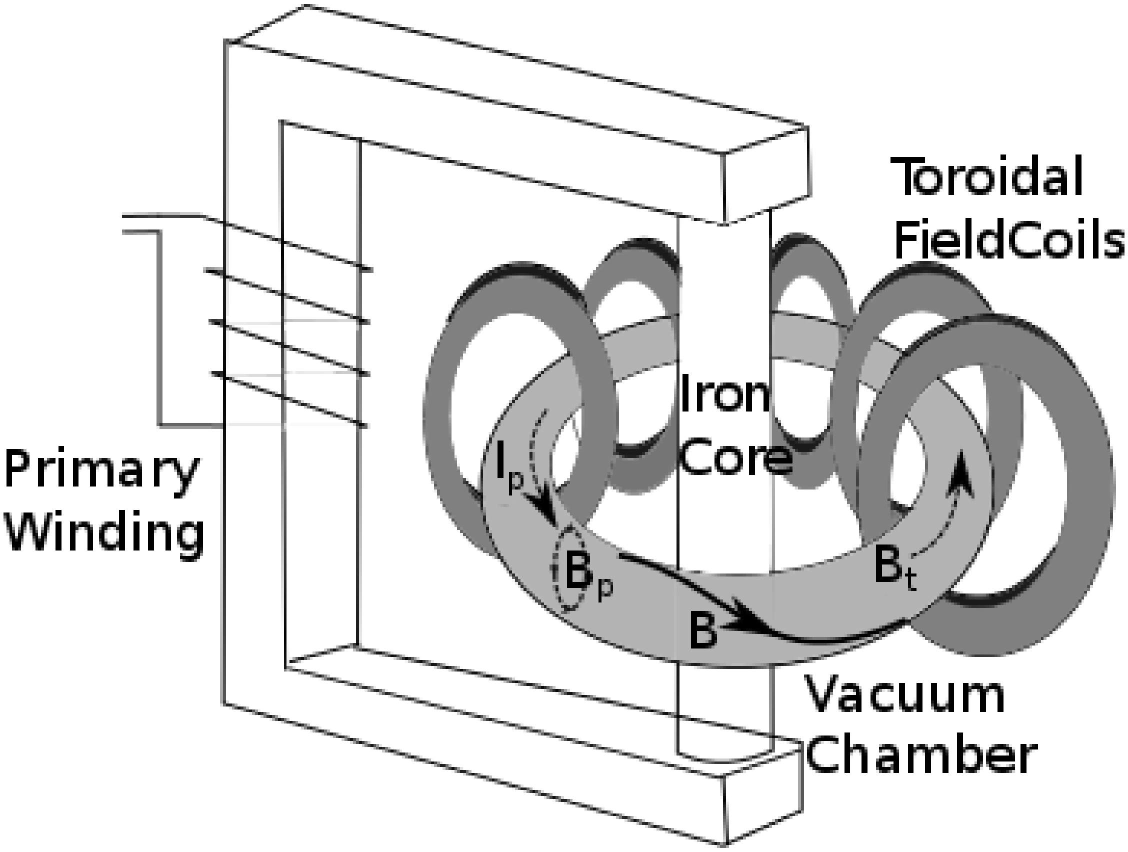

Figure 3.1: Typical configuration of a tokamak

3.2 Safety Factor

In an equilibrium, where $\partial/\partial t = 0$ and $\mathbf{v} = 0$, the fluid momentum equation (Eq. 2.2.6) becomes

$$\nabla p = \mathbf{j} \times \mathbf{B} \ . \tag{3.2.1}$$

The above equation implies that $\nabla p \perp \mathbf{B}$ and $\nabla p \perp \mathbf{j}$. In other words, the magnetic field lines and the current lie on surfaces of constant pressure. Such surfaces are called magnetic surfaces, and p is called a surface function. There can be other surface functions. In an axisymmetric case (symmetric in toroidal direction), the poloidal magnetic flux per unit toroidal angle (denoted by ψ) within a magnetic surface is also a surface function since magnetic fields do not cross flux surfaces.

On a given flux surface (Fig. 3.2), imagine traveling on a magnetic field line which starts

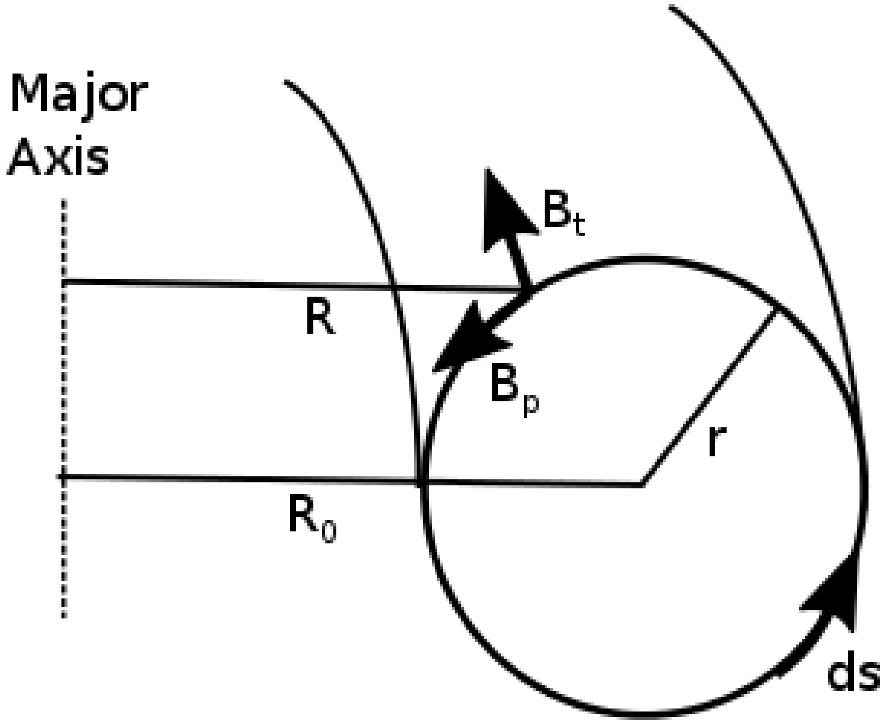

Figure 3.2: A poloidal cross section of a toroidal plasma

at an arbitrary toroidal and poloidal location. After traveling some distance in toroidal direction, the line returns to the original poloidal location. This toroidal traversal over one poloidal traversal is called the safety factor and denoted by q, i.e.,

$$q = \frac{\Delta\phi}{2\pi} \tag{3.2.2}$$

where ϕ is the toroidally traversed angle. At a given point, the ratio of the toroidal displacement to the poloidal displacement of a magnetic field line is

$$\frac{Rd\phi}{ds} = \frac{B_\phi}{B_p} \tag{3.2.3}$$

where ds is the differential poloidal displacement (Fig. 3.2). Taking the integral, the safe factor is obtained as

$$q = \frac{1}{2\pi} \oint \frac{B_\phi}{RB_p} ds \ , \tag{3.2.4}$$

where the integral is taken around the surface in the poloidal direction. For toroidal plasma with high aspect ratio, the safety factor can be approximated as

$$q \simeq \frac{rB_t}{R_0 B_p} \tag{3.2.5}$$

The safety factor is an important parameter as it pertains to the stability of equilibrium in toroidal plasmas [9].

Chapter 4

Turbulence and Geodesic Acoustic Mode

Turbulent transport of plasma is a major cause of loss of plasma energy in magnetic confinement machines such as tokamaks. Zonal flow, a low-frequency poloidal flow, has been found to suppress turbulence and thus attracted major research interests. Geodesic acoustic mode, a finite-frequency branch of zonal flow, has been predicted and detected in toroidal devices. The dynamics of turbulence and zonal flows is a topic of active research. This chapter reviews the above topics and lays the motivation for studying geodesic acoustic mode.

4.1 Drift Wave and Turbulence

Plasmas with finite pressure or density gradient can have flows across the magnetic field and associated oscillations called drift waves. An equilibrium condition is described by imposing $\partial/\partial t = 0$ and $\mathbf{v}$=0. With these conditions, Eq. 2.2.6 reads,

$$\nabla p = \mathbf{j} \times \mathbf{B}, \tag{4.1.1}$$

which indicates that pressure or density gradient is balanced by Lorentz force. The component of the current density perpendicular to $\mathbf{B}$, called the diamagnetic current, can be solved as,

$$\mathbf{j}_{\perp} = \frac{\mathbf{B} \times \nabla p}{B^2}. \tag{4.1.2}$$

The diamagnetic current consists of ion and electron currents, i.e.,

$$\mathbf{j}_{\perp\mathbf{i}} = \frac{\mathbf{B} \times \nabla p_i}{B^2} \ ,$$
$$\mathbf{j}_{\perp\mathbf{e}} = \frac{\mathbf{B} \times \nabla p_e}{B^2}.$$

The magnitudes of the current density of so-called diamagnetic drift currents are

$$\frac{J_{*e}}{n_0} = \frac{k_b T_e}{B L_n} \ ,$$
$$\frac{J_{*i}}{n_0} = \frac{k_b T_i}{B L_n},$$

where ideal gas model was used, and L_n is the length scale for density gradient. We now assume an electrostatic perturbation $\mathbf{E} = -\nabla\phi$. With the background magnetic field $\mathbf{B} = B_0\hat{z}$, equilibrium density $n_{i0} = n_{i0}(x)$, and the perturbations of the form ϕ, $n_{i1} \sim exp(i(k_y y + k_z z - \omega t))$, the continuity equation for ions reads,

$$0 = \frac{\partial n_i}{\partial t} + \nabla \cdot (n_i \mathbf{v_i}) \tag{4.1.3}$$
$$= -i\omega n_{i1} + \mathbf{v_i} \cdot \nabla n_{i0} \tag{4.1.4}$$
$$= -i\omega n_{i1} + \frac{n_{i0}}{L_n} v_{ix}, \tag{4.1.5}$$

where only the first order terms were considered. For oscillations with $\omega \ll \omega_{ci} = eB/m_i$, the dominant velocity component is that of $\mathbf{E} \times \mathbf{B}/B^2$, i.e.,

$$\mathbf{v_i} = -\frac{\nabla\phi \times \mathbf{B}}{B^2} \tag{4.1.6}$$
$$= -i\phi \frac{\mathbf{k} \times \mathbf{B}}{B^2} \tag{4.1.7}$$
$$= -i\phi \frac{k_y}{B} \hat{x} \tag{4.1.8}$$

Substituting Eq. 4.1.8 into Eq. 4.3.4 yields,

$$\omega = \frac{k_y}{B L_n} \frac{n_{i0}}{n_{i1}} \tag{4.1.9}$$

Using quasineutrality and Boltzmann distribution, i.e., $n_i = n_e = n_{i0}(1+e\phi/k_bT_e)$, Eq. 4.1.9 becomes,

$$\begin{aligned}\omega &= \frac{k_y k_b T_e}{BL_n e}\\ &= k_y v_{*e}\\ &= \omega_{*e}.\end{aligned}$$

The frequency thus obtained is called the electron drift frequency. If the finite Larmor radius is taken into account, the frequency becomes,

$$\omega = \frac{\omega_{*e}}{1+b_s}, \tag{4.1.10}$$

where $b_s = (k_\perp \rho_s)^2$ and ρ_s is the ion Larmor radius.

The drift mode can be unstable by different mechanisms. One such mechanism is dissipation. The continuity equation for electrons is, separating the perpendicular and parallel components,

$$\frac{\partial n_e}{\partial t} + \mathbf{v}_{\mathbf{E}\times\mathbf{B}} \cdot \nabla n_0 + \frac{\partial}{\partial z}(n_e v_z) = 0 \tag{4.1.11}$$

The equation of motion in z direction can be used to find v_z, i.e.,

$$0 = -eE_z n_0 - T_e \frac{\partial n_e}{\partial z} - n_0 m \nu_e v_z = 0 \tag{4.1.12}$$

where ν_e is the electron collision frequency. Eq. 4.1.11 and Eq. 4.1.12 can be used to find the perturbed density as

$$n_e = \frac{\omega_{*e} + i\omega_s}{\omega + \omega_s} \frac{e\phi}{T_e} n_0 \tag{4.1.13}$$

where

$$\omega_s = \frac{\left(k_\parallel v_{T_e}\right)^2}{\nu_e} \tag{4.1.14}$$

is the electron diffusion rate parallel to the magnetic field. The quasi-neutrality condition is used to find the dispersion relation as

$$\frac{\omega_{*e}}{1+b_s} = \frac{\omega_{*e} + i\omega_s}{\omega + i\omega_s} \tag{4.1.15}$$

The solution for ω is complex with Im$\omega > 0$, implying an instability [19].

Even in conllisionless plasmas, the instability of drift mode can occur through Landau damping. The analysis of this instability requires the kinetic theory. We introduce the notion of distribution function $f(\mathbf{r}, \mathbf{v}, t)$, where $f(\mathbf{r}, \mathbf{v}, t)d^3\mathbf{r}d^3\mathbf{v}$ is the number of particles in the phase space volume $d^3\mathbf{r}d^3\mathbf{v}$ at time t. The perturbed drift kinetic equation for electrons is given as ([19]),

$$\frac{\partial f}{\partial t} + \mathbf{v}_{\mathbf{E}\times\mathbf{B}} \cdot \nabla f_0 - \frac{e}{m}E_{\parallel} = 0 \tag{4.1.16}$$

Here, f is the perturbed electron distribution function and f_0 the unperturbed distribution function. We assume the perturbation is electrostatic and also Maxwellian distribution for the unperturbed distribution, i.e.,

$$f_0(r, v_z) = n_0(r)\sqrt{\frac{m_e}{2\pi T_e}}e^{-v_z^2/v_{T_e}^2} \tag{4.1.17}$$

Substituting the above equation to the kinetic equation yields

$$f = \left(1 - \frac{\omega - \omega_{*e}}{\omega - k_{\parallel}v_z}\right)\frac{e\phi}{T_e}f_0 \tag{4.1.18}$$

Integrating the above equation in v_z results in

$$n_e = \left(1 + i\frac{\omega - \omega_{*e}}{k_{\parallel}v_{T_e}}\right) \tag{4.1.19}$$

Here, the below approximation was used

$$\frac{1}{v_z - \omega/k_{\parallel}} = i\pi\delta\left(v_z - \omega/k_{\parallel}\right) \tag{4.1.20}$$

The quasineutrality condition leads to the frequency

$$\omega_r = \frac{\omega_{*e}}{1 + b_s} < \omega_{*e} \tag{4.1.21}$$

The growth rate of the instability is

$$\gamma = \sqrt{\pi}\frac{\omega_{*e}(\omega_{*e} - \omega_r)}{k_{\parallel}v_{T_e}} \tag{4.1.22}$$

It is evident that γ is positive, indicating an exponential growth of the fluctuation. This instability used to be called the universal instability since any magnetically confined plasma is subject to it. Later it was found that this instability can be suppressed by shear in magnetic field [19].

In toroidal devices, twist of magnetic field, or toroidicity, can also cause instability in drift mode. The ion density perturbation in a tokamak geometry can be found from continuity equation

$$\left(\frac{\partial}{\partial t} + i\mathbf{k}\cdot\mathbf{V_{D_i}}\right) n_i + \nabla\cdot(\mathbf{v_i} n_0) = 0 \tag{4.1.23}$$

where $\mathbf{V_{D_i}}$ is the ion magnetic drift velocity

$$\mathbf{V_{D_i}} = \frac{2T_i}{eB^3}\mathbf{B}\times\nabla B \tag{4.1.24}$$

Incorporating the $E \times B$ drift, ion polarization drift, and diamagnetic drift, the perturbed ion velocity can be expressed as

$$\mathbf{v_i} = \frac{\mathbf{E}_\perp \times \mathbf{B}}{B^2} + \frac{e}{M_i\omega_{ci}^2}\frac{\partial \mathbf{E}_\perp}{\partial t} + \frac{\mathbf{B}\times\nabla p_i}{neB^2} \tag{4.1.25}$$

Ion pressure perturbation can be found as

$$\left(\frac{\partial}{\partial t} + i\mathbf{k}\cdot\mathbf{V_{D_i}}\right) p_i + \mathbf{v_{E\times B}}\cdot\nabla p_{i0} = 0 \tag{4.1.26}$$

Ignoring the sound wave propagation along the magnetic field, the ion density perturbation can be approximated to

$$n_i = \frac{1}{\omega+\omega_{Di}}\left(\omega_{*e} - \omega_{De} - \frac{\eta_i\omega_{*e}\omega_{Di}}{\omega+\omega_{Di}}\right)\frac{e\phi}{T_e}n_0 = 0 \tag{4.1.27}$$

where $\omega_{Di} = \mathbf{k}\cdot\mathbf{V_{Di}}$ and $\eta_i = \frac{d\ln T_i}{d\ln n}$. Once again, quasineutrality condition is used to yield

$$(\omega+\omega_{Di})^2 - (\omega_{*e}-\omega_{De})(\omega+\omega_{Di}) + (1+\eta_i)\omega_{*e}\omega_{Di} = 0 \tag{4.1.28}$$

The instability is triggered when the pressure gradient and the magnetic gradient are in the same direction[20].

4.2 Zonal Flow

Though turbulence causes the major transport of plasma out of confinement in toroidal devices, it is said to be self-limiting; that is, the size of turbulent eddies does not grow to that of the device. This is because drift wave instability can generate layers of plasma flow perpendicular to the radial direction. This flow is called zonal flow. Zonal flow is believed to arise as a result of nonlinear coupling of drift waves. This flow is a low-frequency, poloidally and toroidally symmetric flow driven by $\mathbf{E} \times \mathbf{B}$ whose direction changes depending on the radial position [21]. It is these alternating flows that cut the turbulent eddies into smaller sizes, regulating the turbulent transport. This limiting behavior of zonal flow has attracted both theoretical and experimental interests [21, 22].

Zonal flow has a higher-frequency branch called geodesic acoustic mode (GAM). This mode is characterised by density oscillation proportional to $\sin\theta$, where θ is the poloidal angle. GAM was first predicted in theory [14] and later observed in various toroidal devices [15]. The following subsection gives a derivation of GAM frequency and a survey of the past studies on the topic.

4.3 GAM Frequency

An equilibrium state, the ideal MHD equations become :

$$0 = -\nabla p + \mathbf{j} \times \mathbf{B} \tag{4.3.1}$$

$$\nabla \times \mathbf{B} = \mu_0 \mathbf{j} \tag{4.3.2}$$

$$\mathbf{E} = 0. \tag{4.3.3}$$

For the derivation of GAM frequency, we express the quantities with their equilibrium and perturbations terms, i.e.:

$$\begin{cases} \rho &= \rho_0 + \tilde{\rho} \\ p &= p_0 + \tilde{p} \\ \mathbf{v} &= \tilde{\mathbf{v}} \\ \mathbf{E} &= \tilde{\mathbf{E}} \\ \mathbf{j} &= \mathbf{j}_0 + \tilde{\mathbf{j}} \end{cases}$$

where Q_0 indicates an equilibrium value that satisfies Eqs. 4.3.1 - 4.3.3, while $\tilde{Q}$ is the harmonic perturbation. Here, we neglect the time variation of $\mathbf{B}$, assuming an electrostatic case. Substituting the above quantities in Eqs. 2.2.5 and 2.2.10 and keeping only the terms linear to the perturbation yield:

$$\frac{\partial \tilde{n}}{\partial t} + n_0 \nabla \cdot \tilde{\mathbf{v}} = 0 \tag{4.3.4}$$

$$\rho_0 \frac{\partial \tilde{\mathbf{v}}}{\partial t} = \tilde{\mathbf{j}} \times \mathbf{B} - \nabla \tilde{p} \tag{4.3.5}$$

$$\rho_0^{-\gamma} \frac{\partial \tilde{p}_0}{\partial t} - \gamma p_0 \rho_0^{-\gamma-1} \frac{\partial \tilde{\rho}}{\partial t} + \tilde{\mathbf{v}} \cdot \nabla \left(\frac{p_0}{{\rho_0}^{\gamma}} \right) = 0 \tag{4.3.6}$$

$$\nabla \cdot \tilde{\mathbf{j}} = 0 \tag{4.3.7}$$

$$\tilde{\mathbf{E}} = \tilde{\mathbf{v}} \times \mathbf{B} \tag{4.3.8}$$

We approximate the toroidal geometry with a cylindrical geometry with r, θ, and z, which are the radius inside the poloidal plane, the poloidal angle, and toroidal displacement, respectively. This is valid for large aspect ratio, i.e., $\frac{R}{a} \gg 1$, where R and a are the major and minor radii, respectively. We express $\tilde{\mathbf{v}}$ as the $\mathbf{E} \times \mathbf{B}$ drift velocity:

$$\tilde{\mathbf{v}} = \frac{\tilde{\mathbf{E}} \times \mathbf{B}}{B^2} \tag{4.3.9}$$

For curved toroidal magnetic field, i.e., $\mathbf{B} = B_0(1 - \frac{r\cos\theta}{R})\hat{\mathbf{e_z}}$ and $\tilde{\mathbf{E}} = \tilde{E}\mathbf{e_r}$, the divergence of the velocity becomes;

$$\nabla \cdot \tilde{\mathbf{v}} = -2 \frac{\tilde{\mathbf{E}} \times \mathbf{B}}{B^3} \cdot \nabla B \tag{4.3.10}$$

$$= 2 \frac{\tilde{\mathbf{E}} \times \mathbf{B}}{B^2 R} \cdot (\cos\theta \mathbf{e_r} - \sin\theta \mathbf{e}_\theta) \tag{4.3.11}$$

$$= 2 \frac{\tilde{E}}{BR} \sin\theta \tag{4.3.12}$$

Substituting Eq. 4.3.12 into Eq. 4.3.4 and assuming the harmonic time variation, we obtain,

$$\tilde{n} = -\frac{2in_0}{\omega} \frac{\tilde{E}}{BR} \sin\theta \ . \tag{4.3.13}$$

Assuming that p_0 and ρ_0 only depend on r, and since $\tilde{\mathbf{v}} = \tilde{v}\mathbf{e}_\theta$, Eq. 4.3.6 simplifies to

$$\tilde{p} = \frac{\gamma p_0}{n_0} \tilde{n} \tag{4.3.14}$$

Substituting Eq. 4.3.14 into Eq. 4.3.5 gives

$$\rho_0 \frac{\partial \tilde{\mathbf{v}}}{\partial t} = \tilde{\mathbf{j}} \times \mathbf{B} - \frac{\gamma p_0}{n_0} \nabla \tilde{n} \tag{4.3.15}$$

Taking the volume integral of Eq. 4.3.7 yields:

$$\int \nabla \cdot \tilde{\mathbf{j}} = \int \tilde{J}_r \mathcal{J} dS = 0 \tag{4.3.16}$$

where $\mathcal{J}$ is the Jacobian of the toroidal coordinate system. For the axisymmetric system, the integration becomes $\frac{1}{2\pi}\int(\cdots)(1+\frac{r}{R}\cos\theta)d\theta$. This simplifies Eq. 4.3.15 to

$$\rho_0 \frac{\partial \tilde{v}}{\partial t} = -\frac{\gamma p_0}{n_0 2\pi} \int \tilde{n}(1+\frac{r}{R}\cos\theta)d\theta. \tag{4.3.17}$$

We substitute Eq. 4.3.13 into Eq. 4.3.17 and take a time derivative to obtain,

$$\frac{\partial^2 \tilde{v}}{\partial t^2} = -\frac{2\gamma p_0}{\rho_0 R^2}\tilde{v}. \tag{4.3.18}$$

Therefore, the lowest order GAM frequency is ([23]),

$$\omega_{GAM1}^2 = \frac{2\gamma p_0}{\rho_0 R^2} = 2\frac{C_s^2}{R^2} \tag{4.3.19}$$

where $c_s^2 = \gamma p_0/\rho_0$ is the ion acoustic speed. If the poloidal magnetic field is taken into account, the frequency becomes,

$$\omega_{GAM1}^2 = \frac{C_s^2}{R^2}(2+\frac{1}{q^2}), \tag{4.3.20}$$

where q is the safety factor.

A derivation of GAM frequency by a higher level model, called kinetic theory, has also been worked out as ([24])

$$\omega_{GAM2}^2 = \frac{2\left(T_e + \frac{7}{4}T_i\right)}{m_i R^2}. \tag{4.3.21}$$

4.4 Previous Experimental Results on GAM

As shown in the previous section, GAM is characterised by potential oscillation of $m = 0$ and $n = 0$ and density oscillation of $m = 1$ and $n = 0$, where m and n are the poloidal and toroidal mode numbers, respectively. Such mode, together with zonal flow, has been experimentally confirmed in various toroidal devices [25, 26, 27, 28]. The corresponding frequencies also match with the theoretical prediction ($\sim C_s/R$) (Fig. 4.1). The coupling between turbulence and GAM has also been detected by bicoherence analysis [26].

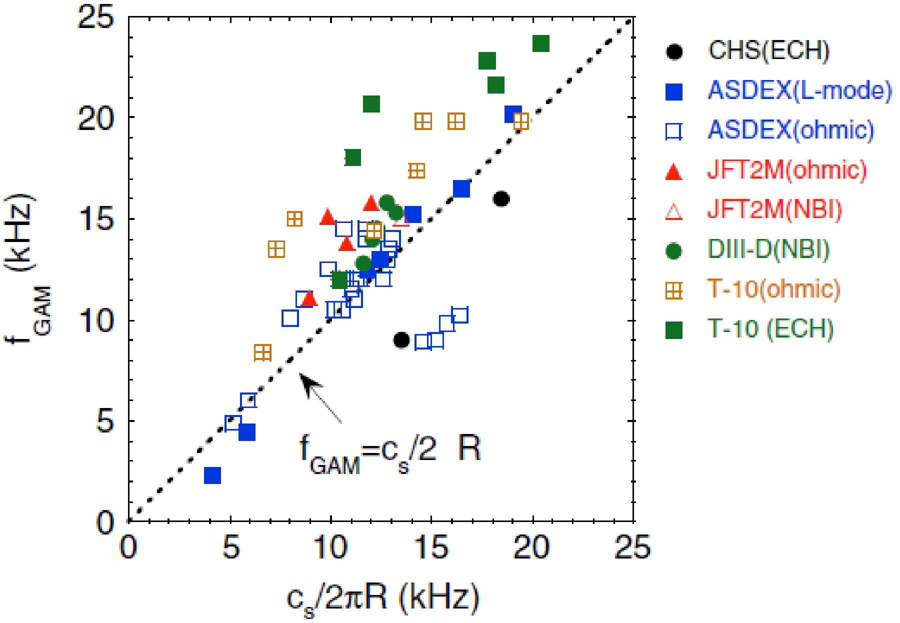

Figure 4.1: Comparison between theoretical and experimental GAM frequencies. Figure was taken from [15].

With the basic features of zonal flow and GAM experimentally confirmed, today's active studies focus on the conditions under which such modes are excited, spatial and temporal dynamics of the modes, and their interactions with other modes present in plasma [29, 30, 31, 32]

There have been attempts to detect GAM in the STOR-M tokamak. In one such experiment [33],GAM could not be confirmed. In another experiment [34], multiple electric probes were used to detect the poloidal dependence of density and potential fluctuations. However, one of the signatures of GAM, i.e., the dependence of $\tilde{\rho}$ on θ, could not be confirmed. The aim of this experimental work was to detect evidence of GAM in STOR-M tokamak, which would benefit the study on turbulence in the STOR-M tokamak in general.

Chapter 5

STOR-M

STOR-M, an acronym for Saskatchewan Torus Modified, is a tokamak situated in Plasma Physics Laboratory at University of Saskatchewan. Its predecessor, STOR-1M, was completed in 1987, and the modification was made on the toroidal magnetic field system in 1994 [35]. The major studies conducted with STOR-M include turbulent heating [36], electrode biasing [36], AC operation [37], and compact torus injection [38]. As of January 2016, STOR-M has produced over 290,000 plasma discharges and remains as the only tokamak active in Canada. This chapter gives the description of the machine and the basic diagnostics.

5.1 Machine Description

The top view of STOR-M is shown in Fig. 5.1. The vacuum chamber of STOR-M is made of two stainless elbows (304L) with circular cross-section and wall thickness of 4 mm. The two elbows are connected with a ceramic break and a bellow at each of the two joining points. A stainless limiter is circular on the side while linear at the top and bottom. A turbo-molecular pump evacuates the chamber to the base pressure of around 8.0×10^{-8} Torr. The operational pressure is controlled by a piezoelectric valve and usually kept around 1.0×10^{-4} Torr.

An iron core with magnetic flux capacity of 0.1 Wb is encircled by the toroidal chamber and used as the core of transformer action. There are three primary windings. One of them negatively biases the core so as to maximize the hysteresis swing. The fast capacitor

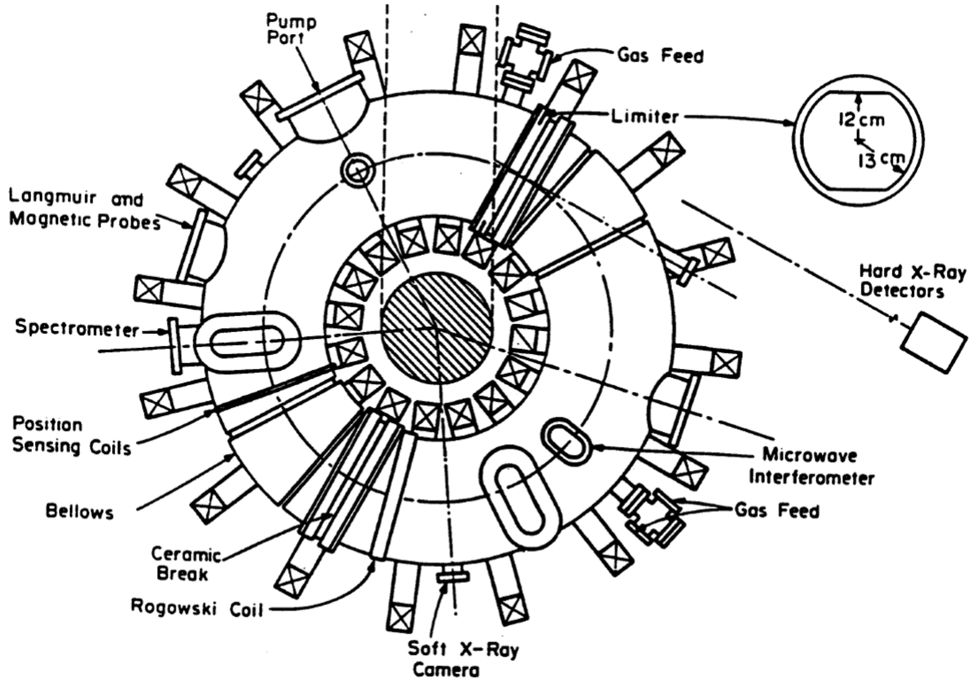

Figure 5.1: Top view of STOR-M

bank (450 V, 200 mF) drives the ramp-up plasma current while the slow bank (100 V, 10 F) drives the plasma plateau. The magnetic coil configuration is shown in Fig. 5.2. The toroidal field coil encircles the chamber to confine the plasma. Vertical coils produce supplemental magnetic fields to keep the plasma in equilibrium. Magnetic pick-up coils are placed around the chamber to detect the position of plasma column. The positions signals are used to adjust the current through the feedback coils (FB) to maintain the plasma equilibrium. The global parameters of a typical STOR-M discharge are listed on Table 5.1

The diagnostic systems available and quantities measured are listed in Table 5.2.

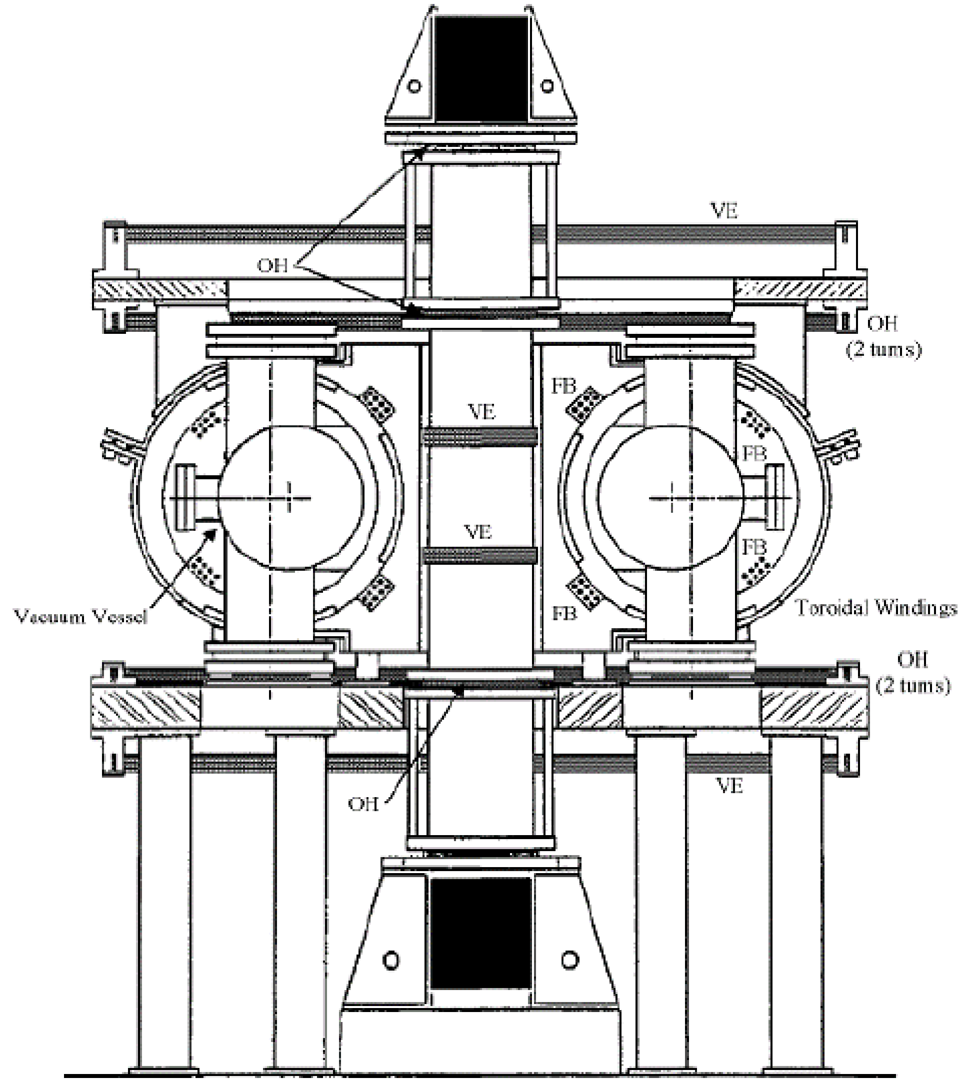

Figure 5.2: Vertical cross-section of STOR-M

Table 5.1: The global parameters of a typical STOR-M discharge.

Major radius	R	46 cm
Minor radius (limiter)	a	12 cm
Toroidal B field	B_ϕ	1 T
Plasma current	I_p	20 - 30 kA
Electron density	n_e	1-3 × 10^{13}cm^{-3}
Electron temperature	T_e	220 eV
Ion temperature	T_i	50 - 100 eV
Discharge duration	t_d	50 ms
Confinement time	τ_e	1 - 3 ms

Table 5.2: The global parameters of a typical STOR-M discharge.

Diagnostic system	Diagnosed parameter
Rogowski coils	Plasma current and toroidal field
Voltage pick-up loop	Loop voltage
Microwave interferometer (4 mm)	Line-averaged electron density
Position sensing coils	Plasma column position
Mirnov coils	Magnetic fluctuations
Soft X-ray camera	Electron density and temperature
Doppler spectrometer	Toroidal flow velocity
H-α spectrometer	H-α emission
Langmuir probes	Edge density and temperature

Chapter 6

Theories of Plasma Diagnostics

Geodesic acoustic mode was originally predicted as an electrostatic oscillations [14]. One of the simplest approaches to observe GAM is by electrostatic probes [39]. Such probes, called Langmuir probes, can be easily implemented for measuring the plasma parameters. In tokamaks with thermal plasma, Langmuir probes are used to measure the plasma parameters at the edge of the plasma, where the plasma is not hot enough to damage the probes. As we also used Langmuir probes for the experiment, this chapter gives the review of the theory of plasma diagnostics by electrostatic probes.

6.1 Probe Measurements

One of the most common ways to study plasma properties is inserting a metallic probe into them. Such probes are called Langmuir probes, named after the pioneering scientist in this approach. For high-temperature plasmas such as those used in fusion research, Langmuir probes are used mainly for studying the edge properties as the probe materials often cannot withstand the heat near the center of the plasma. Though Langmuir probes are easy to implement, the physics behind them is rather complicated, so some assumptions are needed to quantitatively study them. In this theoretical treatment, it is assumed that plasmas are collision-less and that the effect of magnetic field on the probe is negligible.

6.2 Plasma Sheath

Consider an metallic probe in a plasma with comparable electron and ion temperatures, in which the mean speed of the electrons is much higher than that of the ions. This leads to the electron flux higher than the ion flux into the probe. The probe is quickly charged negatively until the electric field is established in a way that the net electric current into the probe is zero. The potential of the probe at this point is called the floating potential and denoted by V_f. This potential is different from the surrounding potential, or plasma potential V_∞, due to the electric field around the probe. In other words, inserting a probe alters the surrounding plasma properties but only to a certain extent. The region of significant influence by the probe is called the sheath, and its thickness is a few times the Debye length λ_D in many cases.

Useful information about a plasma can be extracted by biasing a Langmuir probe and measuring the corresponding current. Following the convention, the current out of the probe is taken to be positive. A typical relationship between the bias voltage and the probe current, often called the I-V characteristics, is shown in Fig. 6.1.

When the probe potential is at the plasma potential ($V = V_\infty$), the probe does not perturb the surrounding plasma, and thus the probe current will be dominated by the electron current, I_e. The probe voltages higher than the plasma potential lead to rejected ions and collected electrons. When all electrons arriving the probe are collected, the situation is called electron saturation, corresponding to the region (A) in Fig. 6.1. In the region (B), the probe voltages lower than the plasma potential reject some electrons and collect some ions. Sufficiently negative probe voltage leads to the saturation of ion current, as shown in the region (C).

In order to study sheath around a probe, consider biasing the probe negatively (V_0) with respect to the plasma potential, which can be defined as $V_\infty = 0$. Assume that a region, thin compared to the probe dimension, establishes so that the potential changes within the region and approaches the plasma potential, as shown in Fig. 6.2. This region is called a sheath, and the sheath-plasma boundary is denoted by x_s with the corresponding potential V_s. Here, the one dimensional representation is valid for a thin sheath. The potential must

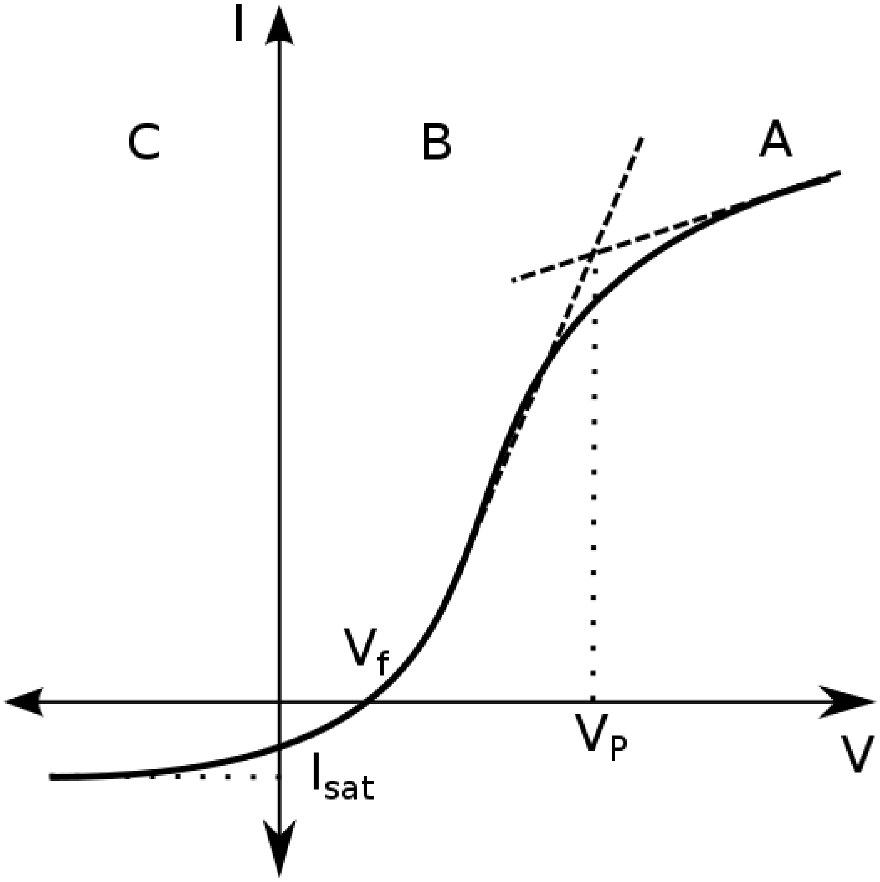

Figure 6.1: Typical relationship between the bias voltage and the probe current of a Langmuir probe

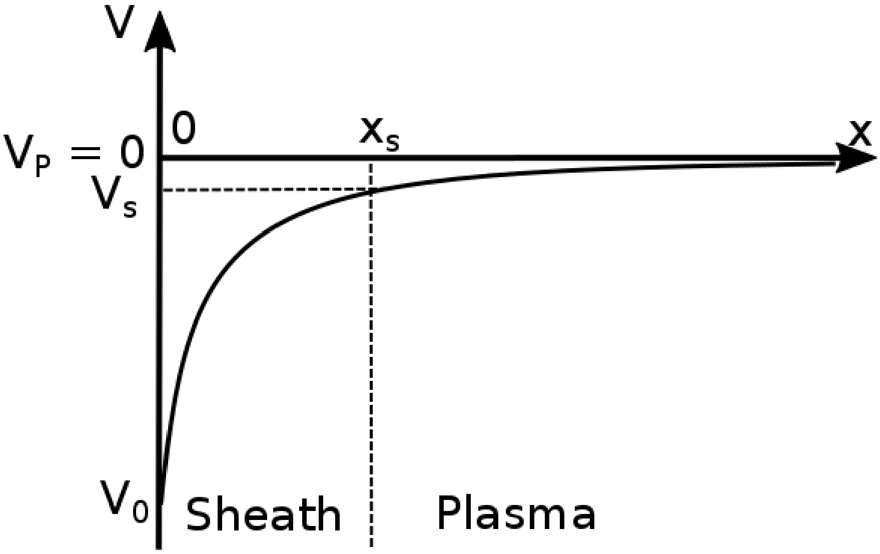

Figure 6.2: Sheath around a negatively biased probe

be solved by the Poisson's equation

$$\nabla^2 V = -\frac{\rho}{\epsilon_0} = -\frac{e}{\epsilon_0}\left(n_i - n_e\right) \ , \tag{6.2.1}$$

and the problem becomes finding the expressions for n_i and n_e.

6.3 Ion and Electron Densities

The ion current can be found with an assumption of $T_e \gg T_i$, enabling the approximation that $v_i \simeq 0$ outside the sheath. Within the sheath, therefore, conservation of energy requires that

$$|v_i| = \left(\frac{-2eV}{m_i}\right)^{1/2} \tag{6.3.1}$$

Neglecting collisions, the ions passing through the sheath-plasma boundary are all collected; i.e., the number of ions crossing a surface area $A(x)$ around the probe at x ($< x_s$) is constant. This constant, denoted by J_i, is related to the particle density as

$$J_i = A(x) n_i v_i \quad \text{or} \tag{6.3.2}$$

$$n_i(x) = \frac{J_i}{A(x)}\left(\frac{m_i}{-2eV(x)}\right)^{1/2} \tag{6.3.3}$$

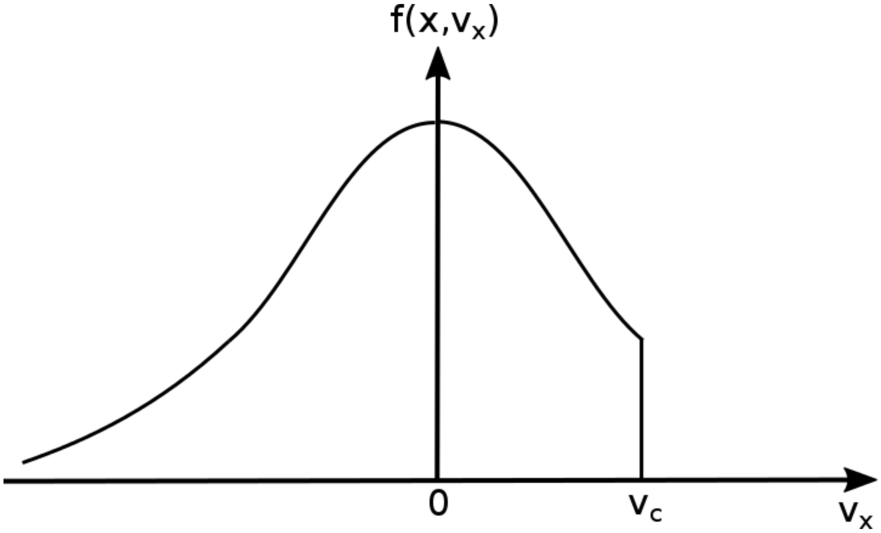

Figure 6.3: Partially depleted electron distribution within a sheath due to collection by the probe

For electrons, note that at any point in the sheath there is a distribution of electrons moving toward the probe. The distribution away from the probe, however, is partially depleted due to the collection by the probe, which is depicted in Fig. 6.3.

In other words, electrons with $v_x > v_c = \sqrt{2e(V(x) - V_0)/m_e}$ are all collected by the probe. The distribution function is thus

$$f(x,v) = \begin{cases} \sqrt{\frac{m_e}{2\pi T_e}} n_\infty \mathrm{exp}([-\frac{m_e v^2}{2} + eV(x)]/T_e) & v \leq v_c \\ 0 & v > v_c \end{cases} \tag{6.3.4}$$

where n_∞ is the number density where the potential is taken to be zero. Integrating Eq. 6.3.4 gives

$$n_e = n_\infty \mathrm{exp}(eV(x)/T_e)\frac{1}{2}\left(1 + \mathrm{erf}\{\sqrt{[V(x) - V_0]e/T_e}\}\right) \tag{6.3.5}$$

where

$$\mathrm{erf}(t) = \frac{2}{\sqrt{\pi}}\int_0^t \mathrm{e}^{-y^2} dy \ . \tag{6.3.6}$$

However, if $e(V(x) - V_0) \gg T_e$, almost all electrons are repelled by the probe and the electron density can be approximated by

$$n_e = n_\infty \mathrm{exp}(eV(x)/T_e) \tag{6.3.7}$$

Substituting Eqs. 6.3.3 and 6.3.7 into Eq. 6.2.1 gives

$$\nabla^2 V = -\frac{e}{\epsilon_0}\left[\frac{J_i}{A(x)}\sqrt{\frac{m_i}{-2eV(x)}} - n_\infty \exp\left(\frac{eV(x)}{T_e}\right)\right] \tag{6.3.8}$$

Assuming that the sheath is thin compared to the probe dimension, i.e. $x_s \ll a$, $A(x)$ can be taken to be constant around $x = x_s$. Also at the sheath-plasma boundary, quasi-neutrality must hold ($n_i(x_s) = n_e(x_s)$). The above conditions lead to a restriction, $V_s = -T_e/e$, for Eq. 6.3.8 to have an exponential decay, thus forming a sheath. Eq. 6.3.3 can now be evaluate at $x = s$ to give

$$J_i = \exp\left(-\frac{1}{2}\right) A(s) n_\infty \sqrt{\frac{T_e}{m_i}} \tag{6.3.9}$$

In other words, by biasing the probe negatively enough to repel almost all electrons and to collect all ions passing the sheath-plasma boundary, the electric current through the probe is

$$I_{sat} = -\exp\left(-\frac{1}{2}\right) eA(s) n_\infty \sqrt{\frac{T_e}{m_i}} \tag{6.3.10}$$

The dependence of the sheath thickness, and $A(s)$, on the bias voltage and the electrons temperature is given as

$$\frac{x_s}{\lambda_D} = \frac{2}{3}\left[\frac{2}{\exp(-1)}\right]^{1/4}\left[\sqrt{\frac{-eV_0}{T_e}} - \frac{1}{\sqrt{2}}\right]^{1/2}\left[\sqrt{\frac{-eV_0}{T_e}} + \sqrt{2}\right] \tag{6.3.11}$$

For the bias voltage around the floating potential, the sheath thickness is in the order of $4\lambda_D$. Therefore, the area of sheath-plasma boundary surface can often be approximated by the probe surface area, A_p, as the sheath thickness is a few times the Debye length, which is often significantly smaller than the probe dimension. Measuring I_{sat} gives the information on the product of $n_\infty \sqrt{T_e}$ [40].

6.4 Probe Current and Plasma Parameters

With Eqs. 6.3.7 and 6.3.9 one can express the general expression for the probe current as

$$I = n_\infty e A_p \sqrt{\frac{T_e}{m_i}}\left[\frac{1}{2}\sqrt{\frac{2m_i}{\pi m_e}} \exp\left(\frac{eV_0}{T_e}\right) - \frac{A_s}{A_p}\exp\left(-\frac{1}{2}\right)\right] \tag{6.4.1}$$

where a Maxwellian distribution was used for the electron thermal speed, i.e., $\bar{v} = 2\sqrt{\frac{2T_e}{\pi m_e}}$. Assuming $a \gg \lambda_D$, differentiation of Eq. 6.4.1 yields

$$\frac{dI}{dV_0} = \frac{e}{T_e}(I - I_{sat}) + \frac{dI_{sat}}{dV_0} \tag{6.4.2}$$

The last term of Eq. 6.4.2 comes from the dependence of the x_s on V_0. At $V_0 = V_f$ and for typical STOR-M parameters, $\frac{dI_{sat}}{dV_0} / \frac{dI}{dV_0} \approx 0.0003$, showing that the last term in Eq. 6.4.2 can be neglected in this region. This approximation leads to

$$\ln|I - I_{sat}| = \frac{e}{T_e}V + C \tag{6.4.3}$$

where C is a constant. Finally, taking the derivative of Eq. 6.4.3 with respect to V yields

$$T_e = 1 / \frac{d\left(\ln|I - I_{sat}|\right)}{d\,(eV)} \tag{6.4.4}$$

The above equation indicates that the electron temperature can be obtained by measuring the slope of the plot for $\ln|I - I_{sat}|$ against eV. This can be achieved in experiment by varying the probe voltage and measuring the corresponding current. Once T_e is found, Eq. 6.3.10 can be used to find n_∞, i.e.,

$$n_\infty = -\frac{I_{sat}}{\exp\left(-\frac{1}{2}\right) eA_p)\sqrt{\frac{T_e}{m_i}}} \tag{6.4.5}$$

where $A_s \approx A_p$ was used. However, the time resolution of this method is limited by the voltage sweeping frequency. For studying fluctuations higher than the sweeping frequency the best practice is to assume that the temperature is constant over one sweeping period. This assumption leads to

$$\tilde{n}_\infty \propto \tilde{I}_{sat} \ . \tag{6.4.6}$$

This approximation is used in our experiment.

Eq. 6.3.8 also leads to a relationship between the floating and plasma potential, given by

$$V_\infty = V_f + \frac{T_e}{2e}\ln\left(\frac{m_i}{2\pi m_e}\right) \tag{6.4.7}$$

where V_∞ and V_f are taken with respect to a common ground such as the chamber wall. The assumption of constant temperature again enables the approximation

$$\tilde{V}_\infty \propto \tilde{V}_f \ . \tag{6.4.8}$$

which is used in our experiment.

Chapter 7

Data Analysis Methods

The electrical signals obtained from the experiment are discrete samples of continuous phenomena, or time series. In order to find oscillations such as GAM in those signals, signal processing techniques must be employed. The foundation of the data analysis methods used in this work is Fourier analysis, which can extract frequency information from time series data. This chapter gives a review of the methods used to analyse the experimental data.

7.1 Spectral Analysis

The basis of the data analysis used in this study is Fourier analysis. This section first introduces the concept of Fourier analysis for continuous functions. It then derives the corresponding Fourier expression for discrete functions, which enables the interpretation of real, discrete signals obtained from experiments.

7.1.1 Continuous Fourier Analysis

The theorem on which Fourier analysis is based is the following. This theorem is applicable for periodic functions, i.e., those of the form $x(t+T_p) = x(t)$[41].

Theorem 7.1.1. *Let $x(t)$ be an T_p-periodic function such that $x(t)$ and its derivative are piece-wise continuous. Then the Fourier series*

$$\sum_{n=-\infty}^{\infty} c_n e^{in\frac{2\pi}{T_p}t} \quad , \textit{ with } c_n = \frac{1}{T_p}\int_{-\frac{l}{2}}^{\frac{l}{2}} e^{-in\frac{2\pi}{T_p}t} x(t)dt \ ,$$

converges uniformly to $x(t)$ in the subintervals where $x(t)$ is continuous.

The above theorem shows that a piece-wise continuous periodic function can be expressed as an infinite series of the basis function of the harmonic form $e^{in\frac{2\pi}{T_p}t}$. The above theorem leads to the following expression known as Parseval's relation.

$$P_x = \frac{1}{T_p}\int_{T_p} |x(t)|^2 dt = \sum_{n=-\infty}^{\infty} |c_n|^2 \tag{7.1.1}$$

If x expresses a voltage across a resister in an electronic circuit, for example, P_x is proportional to the power dissipated by the resistor. Therefore, the physical interpretation of the above equation in this example is that $|c_n|^2$ indicates the power due to the component with frequency $\frac{n}{T_p}$.

Physical phenomena, however, are not always periodic. The extension of theorem 7.1.1 for aperiodic functions is made by letting $T_p \to \infty$. In this limit the infinite series becomes an integral, i.e.,

$$x(t) = \int_{-\infty}^{\infty} X(f)e^{i2\pi ft} df \tag{7.1.2}$$

$$X(f) = \int_{-\infty}^{\infty} x(t)e^{-i2\pi ft} dt \tag{7.1.3}$$

Here, $X(f)$ is called the Fourier transform of $x(t)$, and $x(t)$ the inverse Fourier transform. An expression analogous to Eq. 7.1.1 can be made for this case.

$$E_x = \int_{-\infty}^{\infty} |x(t)|^2 dt = \int_{-\infty}^{\infty} |X(f)|^2 df \tag{7.1.4}$$

Here, the physical interpretation of $|X(f)|^2$ is the power of the component with frequency f. This is a highly useful relation for, for example, finding a dominant frequency in an electrical signal obtained from the experiment.

7.1.2 Discrete Fourier Analysis

The previous section introduced the concept of Fourier transform for continuous function. In experiments, however, the data are in the form of discrete points over a finite period of time. In other words, an experimental signal of length L can be expressed as a sequence $x(n)$ that has finite values for the interval $0 \le n \le L-1$ and 0 otherwise. This is a discrete aperiodic sequence. The discrete equivalent of the Fourier transform pair (Eqs. 7.1.2 and 7.1.3) is

$$x(n) = \frac{1}{2\pi} \int_{2\pi} X(\omega) e^{i\omega t} d\omega \tag{7.1.5}$$

$$X(\omega) = \sum_{n=-\infty}^{\infty} x(n) e^{-i\omega n} \tag{7.1.6}$$

It is important to know that an aperiodic discrete signal has a continuous spectrum. To discretize the spectrum, consider taking N samples of $X(\omega)$ with equal intervals, i.e.,

$$X\left(\frac{2\pi}{N}k\right) = \sum_{n=-\infty}^{\infty} x(n) e^{-i2\pi kn/N}, \quad k = 0, 1, ..., N-1 \tag{7.1.7}$$

Subdividing the summation, it can be shown that

$$X\left(\frac{2\pi}{N}k\right) = \sum_{n=0}^{N-1} x_p(n) e^{-i2\pi kn/N}, \quad k = 0, 1, ..., N-1 \tag{7.1.8}$$

where

$$x_p(n) = \sum_{l=-\infty}^{\infty} x(n - lN). \tag{7.1.9}$$

Since x_p is N-periodic, it can be expanded in Fourier series, resulting in a relation

$$x_p(n) = \frac{1}{N} \sum_{k=0}^{N-1} X\left(\frac{2\pi}{N}k\right) e^{i2\pi kn/N}, \quad k = 0, 1, ..., N-1 \tag{7.1.10}$$

The relationship shown in Eqs. 7.1.8 and 7.1.10 implies that a discrete signal of finite length, i.e., $x(n)$ with $x(n) = 0$ for $n < 0$ and $n \geq L$, can also be expressed by a discrete Fourier series. This is done by generating a periodic signal $x_p(n)$ with period $N(\geq L)$ and with the property $x(n) = x_p(n)$ for $0 \leq n \leq N-1$. The resulting Fourier pair is

$$x(n) = \frac{1}{N} \sum_{k=0}^{N-1} X(k) e^{i2\pi kn/N}, \quad n = 0, 1, ..., N-1 \tag{7.1.11}$$

$$X(k) = \sum_{k=0}^{N-1} x(n) e^{-i2\pi kn/N}, \quad n = 0, 1, ..., N-1 \tag{7.1.12}$$

The first expression is called the inverse discrete Fourier Transform (IDFT) and the second the discrete Fourier transform (DFT)[42]. The above relationship forms the foundation for the signal processing technique used for analysing the data in this study.

7.2 Methods for Estimating Spectral Properties

Due to the discrete nature of the experimental data, estimations must be made for understanding the spectral characteristics of real, continuous natural phenomena. This section introduces the estimation methods used in this study.

7.2.1 Power Spectral Density

The first spectral property to be estimated is the power spectral density of a signal. One form of an estimate power spectral density using discrete, finite signals is called periodogram, which is defined as

$$P_{xx}\left(\frac{k}{N}\right) = \frac{1}{N}\left|\sum_{n=0}^{N-1} x(n)e^{-i2\pi kn/N}\right|^2 = \frac{1}{N}\left|X\left(\frac{k}{N}\right)\right|^2 \tag{7.2.1}$$

While the above equation gives one estimate of power spectral density, an improvement can be made to reduce the variance, the expected squared deviation from the true power spectral density. One way to accomplish this is a method called Welch's method. In Welch's method, the signal $x(n)$ of length N is divided into possibly overlapping segments of a same length. A window function is applied to reduce the effect of discontinuities at the edges. The periodogram for each segment is calculated and averaged to give the estimate for the power spectral density[43]. The resulting estimate has lower variance than the method described by Eq. 7.2.1, but one drawback is the reduced frequency resolution due to the reduced number of samples per segment. In this study, Welch's method is used to estimate the power spectral density.

7.2.2 Cross Spectral Density

The previous section introduced the estimate of power spectral density, which involved one signal. However, in order to determine the mode number of oscillations such as GAM, it is necessary to compare signals from different locations. A method which can be used for this purpose is called cross spectral spectrum. Given two signals, $x(n)$ and $y(n)$, the cross spectral density of the two signals is defined as

$$P_{xy}(f) = \lim_{T\to\infty}\frac{1}{T}E\left\{X(f)^*Y(f)\right\} \tag{7.2.2}$$

where $E\left\{\bullet\right\}$ indicates an expectation value. Analogous to the estimation of the power spectral density, cross spectral density can be estimated by

$$P_{xy}\left(\frac{k}{N}\right)=\frac{1}{N}X^{*}\left(\frac{k}{N}\right)Y\left(\frac{k}{N}\right) \tag{7.2.3}$$

Here again, Welch's method can be applied to estimate the cross spectral density, i.e., taking overlapping segments and taking the average [43]. As can be seen in Eq. 7.2.3, P_{xy} is generally complex. The phase of $P_{xy}\left(\frac{k}{N}\right)$ indicates the phase difference between the two signals for the frequency $\frac{k}{N}$. Another important interpretation which can be derived from cross spectral density is the property called coherence. For two signals, the coherence for the frequency $\frac{k}{N}$ is defined as

$$C_{xy}\left(\frac{k}{N}\right)=\frac{\left|P_{xy}\left(\frac{k}{N}\right)\right|^{2}}{P_{xx}\left(\frac{k}{N}\right)P_{yy}\left(\frac{k}{N}\right)} \tag{7.2.4}$$

By Cauchy-Schwarz inequality, it can be shown that $0\leq C_{xy}\leq 1$. This normalized parameter indicates the consistency of the phase between the two signals over the sampling period. If $C_{xy}\simeq 1$, it means that the phase between the two signal is constant, and thus the phase has statistical significance. In contrast, if $C_{xy}\simeq 0$, it would indicate that the phase is random and has not significance.

Chapter 8

Developmental Work

The main purposes of our experiment are to find GAM in STOR-M Tokamak and to find its cause. Carrying out this experiment necessitated different experimental devices, not all of which were immediately available in the laboratory. In order to carry out the experiment in a cost-effective way, we developed three systems necessary for the experiment with components which were readily available in the market and also inexpensive.

The first system is a differential optoisolator system. Experimental establishment of GAM signal and turbulent modes requires high signal-to-noise ratio. Noise is particularly a serious issue for STOR-M as it has aged over the extended period of operation. Moreover, GAM observation requires simultaneous measurements of signals such as those from Langmuir probe systems. Therefore it is vital to avoid ground loops, sources of common-mode noise. In order to isolate the signals, we developed a high-bandwidth differential optoisolator system with inexpensive, high-frequency components available in the market.

The second system is a four channel sweeping power supply. A sweeping voltage can be applied to a Langmuir probe to produce I-V characteristics, from which electron temperature can be obtained (section 6.1). In order to measure the temperature at different locations, we developed a four channel sweeping voltage supply.

The third system is a gated DC power supply. In case of finding GAM in STOR-M, we planned to apply a DC electrode bias and study its effect on GAM. In order to study the effect before, during, and after the electrode bias, we designed a gated DC power supply. The above three devices are elaborated in the following sections.

Finally, as part of data analysis, we developed a Python graphical user interface which allowed us to view and make elementary anaysis on the data obtained from each STOR-M discharge.

This chapter gives the descriptions of the devices and the software we developed for the experiment.

8.1 Differential Optoisolator System

Optoisolator is a way to isolate the common for the electrical signal source from that for the receiving system. We developed a cost-effective differential optoisolator system with components available in the market. We used the system to acquire electrical signals which are subject to common-mode noise due to STOR-M discharges. The differential optoisolator system consists of two main components: differential amplifier and an optoisolator. The following subsections provide the motivation for this system and detailed description of the components as well as the entire system.

8.1.1 Motivation for Optoisolators

Data acquisition is an essential part of any experiment. Ensuring the quality of electrical signals is particularly challenging in noisy environments such as that involving a tokamak. One of the noise sources is inductive coupling, in which changing magnetic fields, produced by coils for toroidal magnetic field, position-control magnetic fields, and ohmic heating, induce voltage across a current loop. Any electrical loop can "pick up" this noise through induction, deteriorating the resulting signals.

Typically, electrical signals are transferred as a voltage difference between two points. When transferring a signal from one system to another, caution must be taken in terms of grounding the two systems. Simply grounding both systems and connecting the two leads would create a loop around one of the two leads through the common ground. The loop, known as ground loop, is depicted in Fig. 8.1. Temporal changes in magnetic flux through the ground loop would develop a voltage difference between points A and B. This difference in turn corrupts the true signal. This is particularly a serious issue in tokamak experiments,

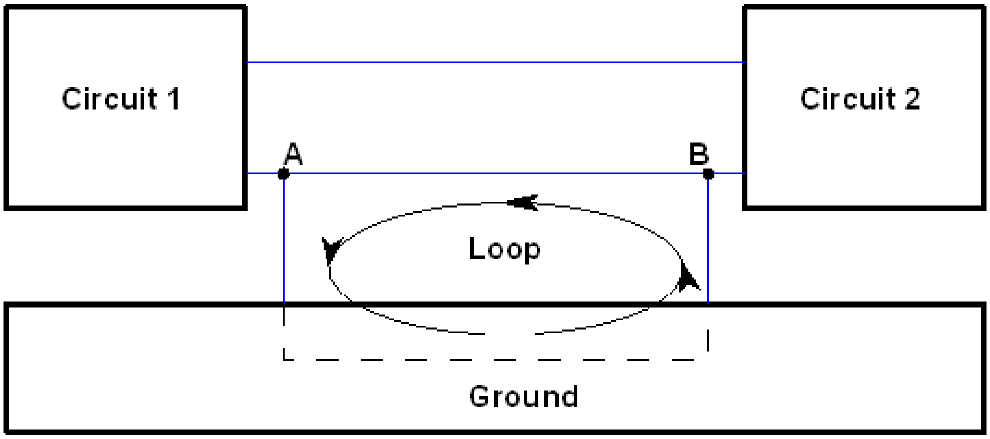

Figure 8.1: Ground loop formation when transferring an electrical signal from one system to another

in which strong magnetic fields are produced.

The solutions for the problem of ground loop include uses of transformers, common-mode chokes, and optoisolators. The method with transformers isolates the two systems electrically and transfer the signal by magnetic induction. While this method breaks the ground loop, this method suffers from some disadvantages such as the size of the transformer and its frequency response. The method with common-mode chokes also uses transformer action to cancel the noise. However, this method does not break the ground loop, and the frequency response is still an issue[44].

The method with optoisolators capitalizes the characteristics of emission and absorption of light by semiconducting materials. The schematics of an optoisolator system is shown in Fig. 8.2. This method breaks the ground loop and electrically isolates the two systems. This method has higher frequency response than the above methods, owing to the transfer of signal by light. A challenge with optoisolators, however, is the non-linearity of the system. Improvement has been made to maintain linearity in enhanced operational regions, which has made possible the application of optoisolators to transferring analog signals. In our development, we used one of the optoisolator chips which are readily available in the market.

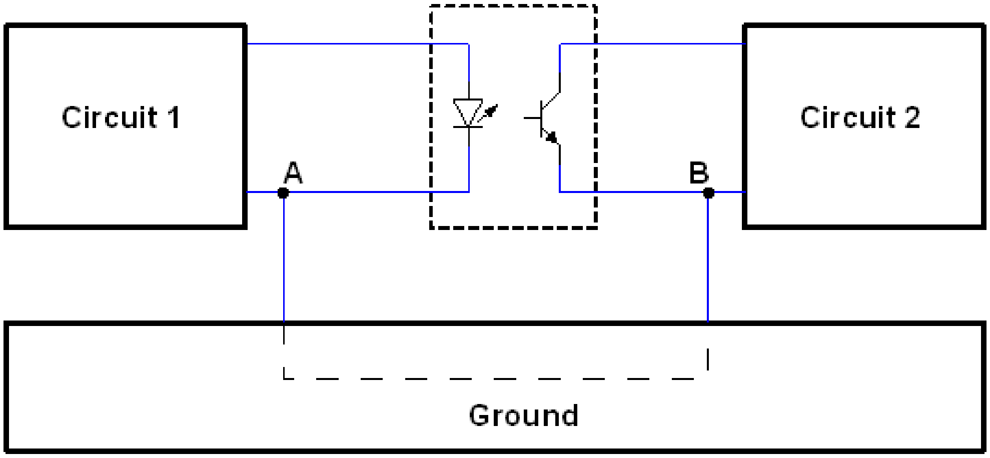

Figure 8.2: Schematics of an optoisolator system

8.1.2 Differential Amplifier

Differential amplifier takes an important role to reject common mode noise due to poor ground connections of the system. We have observed that common mode noise is one of the major issues with STOR-M. To tackle this problem, we used a differential amplifier chip INA149 ([45]). The reason for selecting this chip was that it had a high common-mode rejection ratio(90dB) and a high slew rate $2.2V/\mu s$. It has comparatively low frequency response around 500KHz, but it was sufficient our experimental requirements. The pin configuration of INA149 is shown in Fig. 8.3. The resistors are arranged such as that the chip can allow common mode of up to ±275 V and gain 1. INA149 can be used in various configurations. In our experiment, we used one of the recommended configurations, shown in Fig. 8.4

8.1.3 Optoisolator Circuit

The central part of the optoisolator system is HCNR200 (Avago), a high-linearity analog optoisolator chip[46]. We chose this chip because it had a highest frequency response among others in the market which we tested. The band width of this chip is around 1 MHz. The internal schematics of the chip is shown in Fig. 8.5. It consists of one LED and two photodiodes (PD1 and PD2). This chip can be used for many applications such as transmitting digital and analog signals. For our purpose, we used the chip for transmitting analog sig-

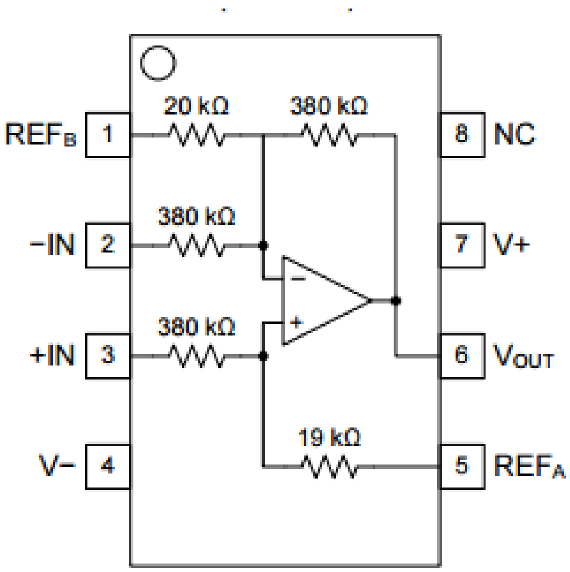

Figure 8.3: The pin configuration of INA149. The diagram was taken from the datasheet [45].

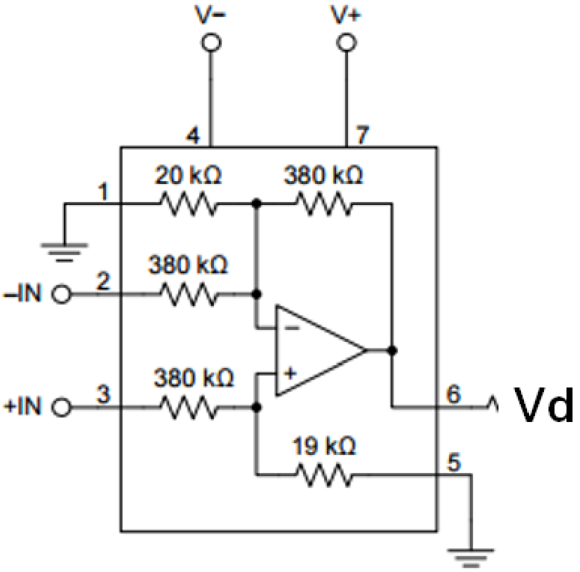

Figure 8.4: A recommended configuration of INA149. The diagram was taken from the datasheet [45].

nals. To make the isolation circuit for broad use, we used one of the company-recommended configurations as the building block (Fig. 8.6). This system transfers analog signal of value

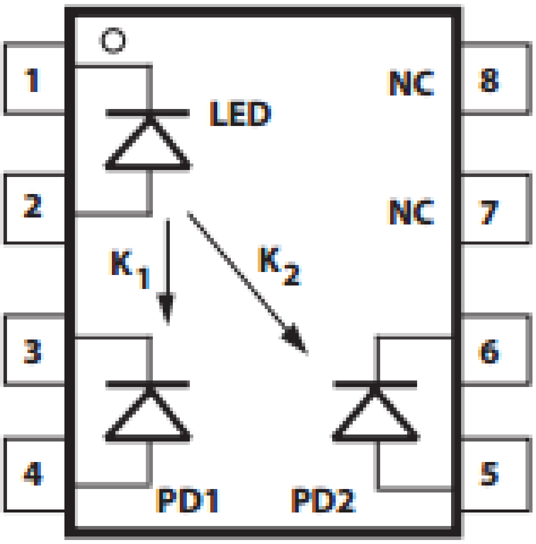

Figure 8.5: The internal schematics of HCNR200 chip. The diagram was taken from the datasheet [46].

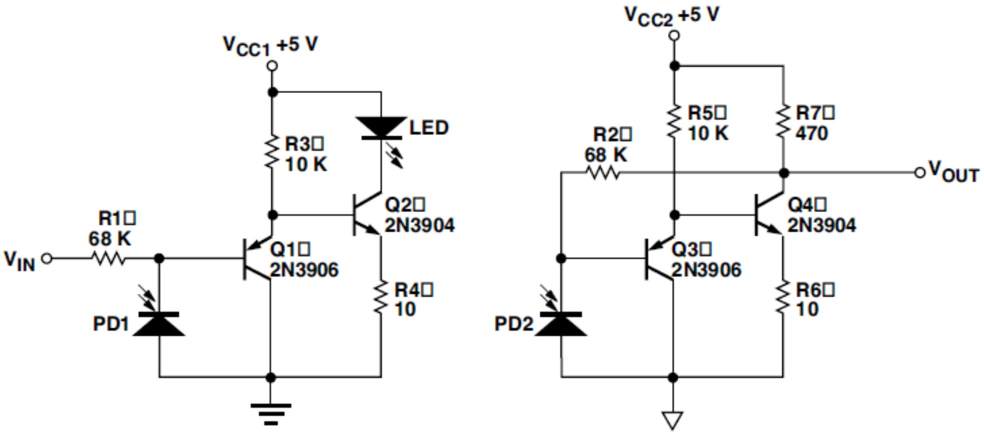

Figure 8.6: The recommended circuit of a high-frequency, low-cost analog optoisolator. The diagram was taken from the datasheet [46].

ranging from 1 - 4 V with gain 1 and bandwidth 1.5 MHz. The signal received as V_{IN} leads to a current through the LED, which in turn causes a current through PD2, rendering the output signal V_{OUT}. PD1 is the feedback photodiode in order to maintain the linearity. In this company-recommended configuration, the resistors are selected to keep the forward current through the LED within the linear region, which is from 2 to 20 mA. One disadvantage of this building block circuit is that it can only transfer analogue signal within +1V to +4 V and not negative voltage.

8.1.4 Differential Optoisolator System

With the two main chips, HCNR200 and INA149, we developed a differential optoisolator system which allows both negative and positive differential signals. The overall schematics of the system is shown in Fig. 8.7.

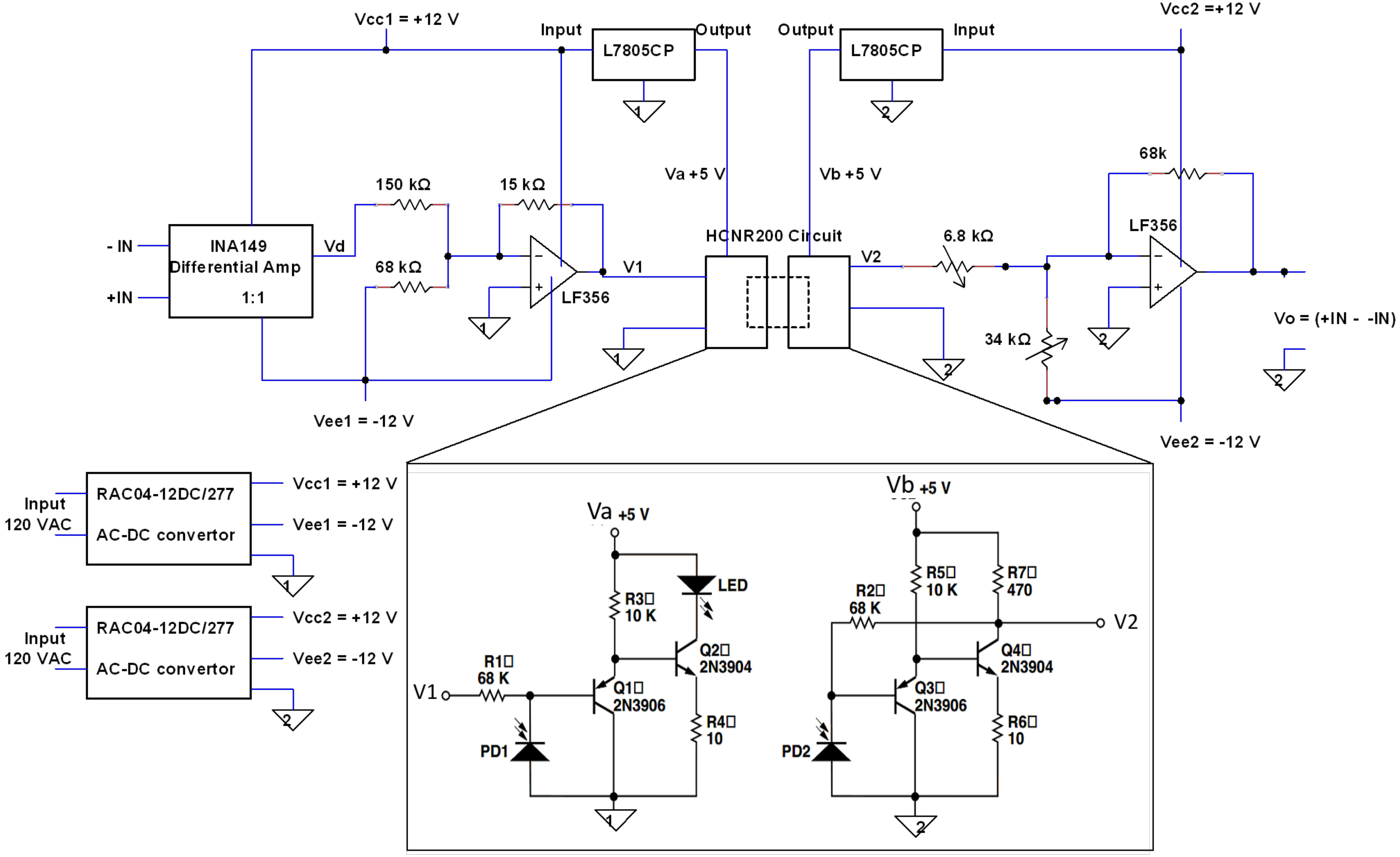

Figure 8.7: Circuit diagram of differential opto-coupler system

The system requires two independent DC power supplies, each with power outputs of ±12 V, to separate the input common from output common. Voltage regulators are used to power the company-recommended circuit Fig. 8.6, which is at the center of the system. The differential signal is fed to the inputs of a differential op-amp with gain 1. In order to allow differential voltages ranging from -10 V to +10 V, the output of the differential op-amp is attenuated by a factor of 10 through an op-amp in the inverting configuration. In order to allow the negative swing, a DC offset is also introduced such that the output of the op-amp, V1, is within the allowable range for the circuit in Fig. 8.6 (1 - 4 V). In other words, if the input differential voltage is 0 V, for example, V1 and V2 would be 2.5 V. The output of the optoisolator, V2 (= V1), is then fed to another op-amp. This op-amp does the opposite of the first op-amp; it amplifies the signal by a factor of 10 and subtracts the DC offset. The final output is then same as the differential input voltage, i.e., $V_o = (+IN - -IN)$. The frequency response of the differential optoisolator system is shown in Fig. 8.8. As shown in the plots, the bandwidth of this system is 100 kHz.

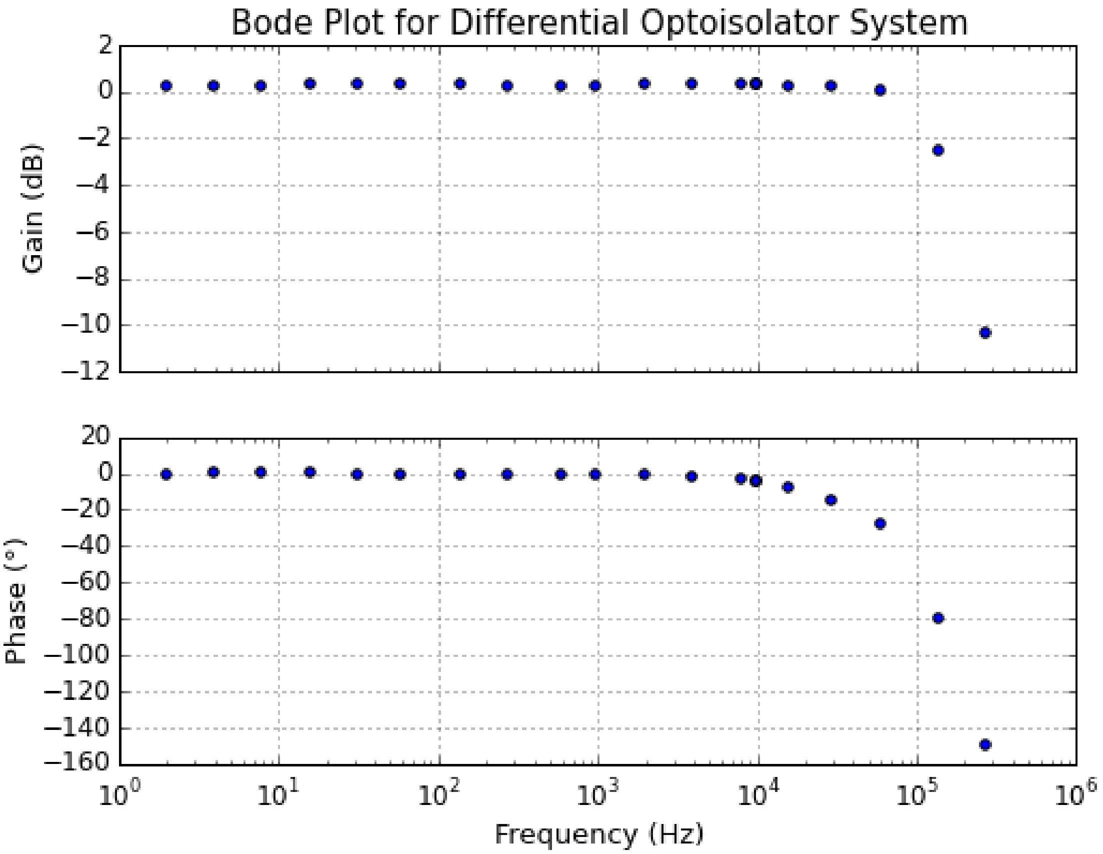

Figure 8.8: Bode plots of differential optoisolator system

8.2 Four Channel Sweeping Power Supply

8.2.1 Motivation for Developing a Sweeping Power Supply

Electron temperature is one of the important parameters which determines the GAM frequency. As discussed in section 6.1, plasma electron temperature can be obtained from the transition part of I-V characteristic of a single Langmuir probe. I-V characteristics can be obtained by either changing the applied probe voltage from discharge to discharge or sweeping the probe voltage during a plasma discharge. The first method requires more time and the assumption that the electron temperature is same for different discharges. The second method assumes that the electron temperature is constant in the time window during which the voltage is swept, which is more probable than the first assumption. Therefore, we used the second method. In this method, a sweeping power supply is required to sweep applied probe voltage from negative to positive with respect to the tokamak ground. Usually, available commercial sweeping power supplies in the market are expensive. The goal of this development was to build a low-cost power supply system that can provide sweeping voltage with tunable frequency. We also made it a four-channel system in order to obtain the temperature at multiple locations.

8.2.2 Four Channel Sweeping Power Supply Circuit

The four channel sweeping power supply consists of four separate sweeping power supplies which are driven by a single function generator. Essentially, each sweeping power supply is a combination of voltage and power amplifier fed by a function generator. The block diagram of the system is shown in Fig. 8.9. The diagram shows four identical systems, all fed by a single function generator. The function generator signal is first fed to optoisolators in order to isolate the four systems from each other. The isolated signal is then transmitted to an amplifier circuit for voltage and power amplification. The output is connected to Langmuir probes to obtain the I-V characteristics. Therefore, this system can measure T_e at four different locations simultaneously. The detail descriptions of the optoisolator and the amplifier are given below.

8.2.3 Optocoupler Circuit

The circuit of the optoisolator is shown in Fig. 8.10. This circuit is the company-recommended circuit shown in Fig. 8.6 with a slight modification. A DC offset is given by a voltage divider at the function generator input, which varies from -1 to +1 V at maximum. The output is the function generator input with the DC offset. This signal is fed to the amplifier described below.

8.2.4 Power Amplifier Circuit

The circuit of the voltage-power amplifier is shown in Fig. 8.11.

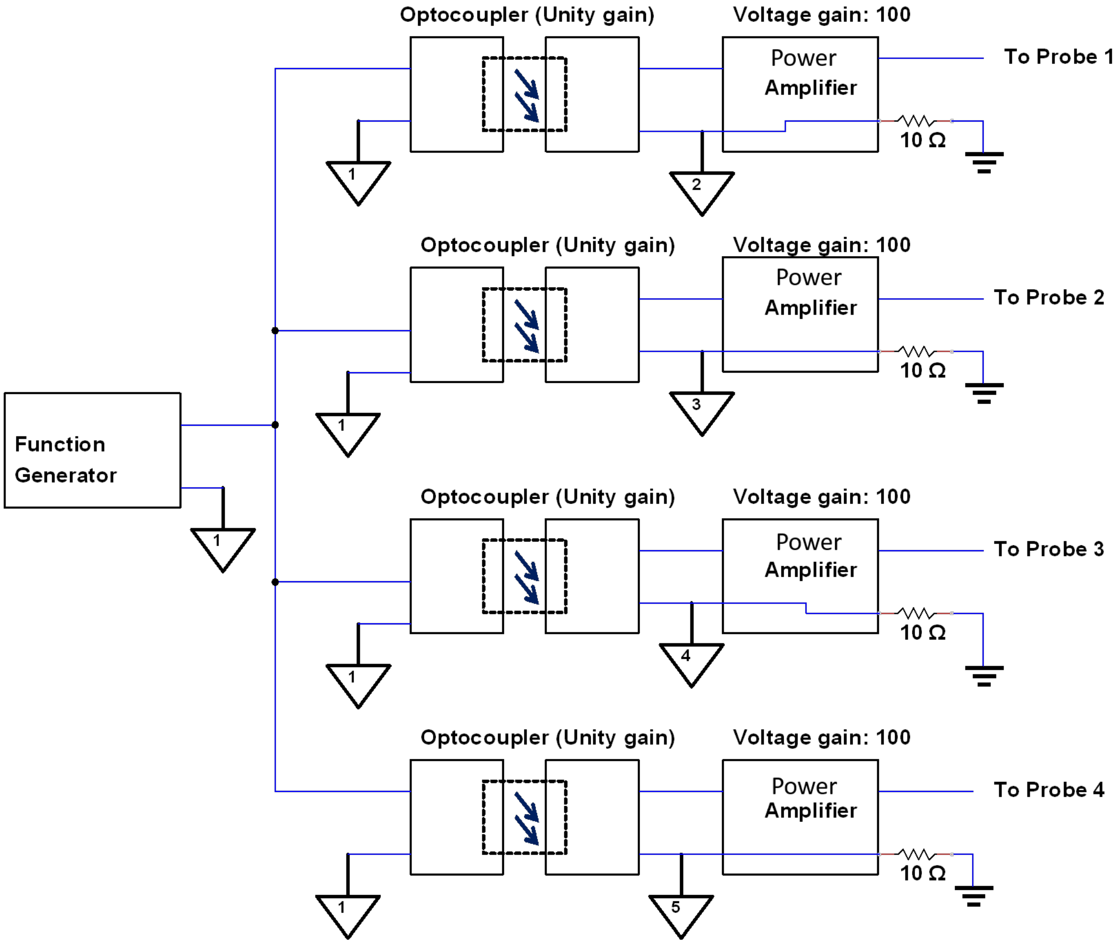

Figure 8.9: Block diagram of the sweeping voltage supply system

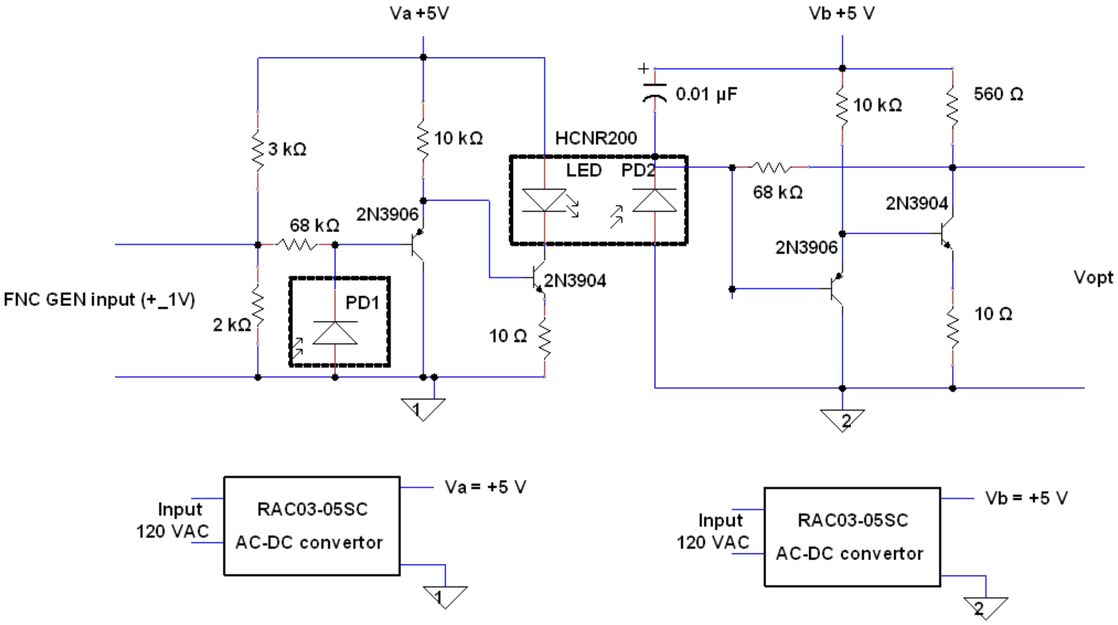

Figure 8.10: Circuit diagram of the optoisolator for sweeping voltage supply

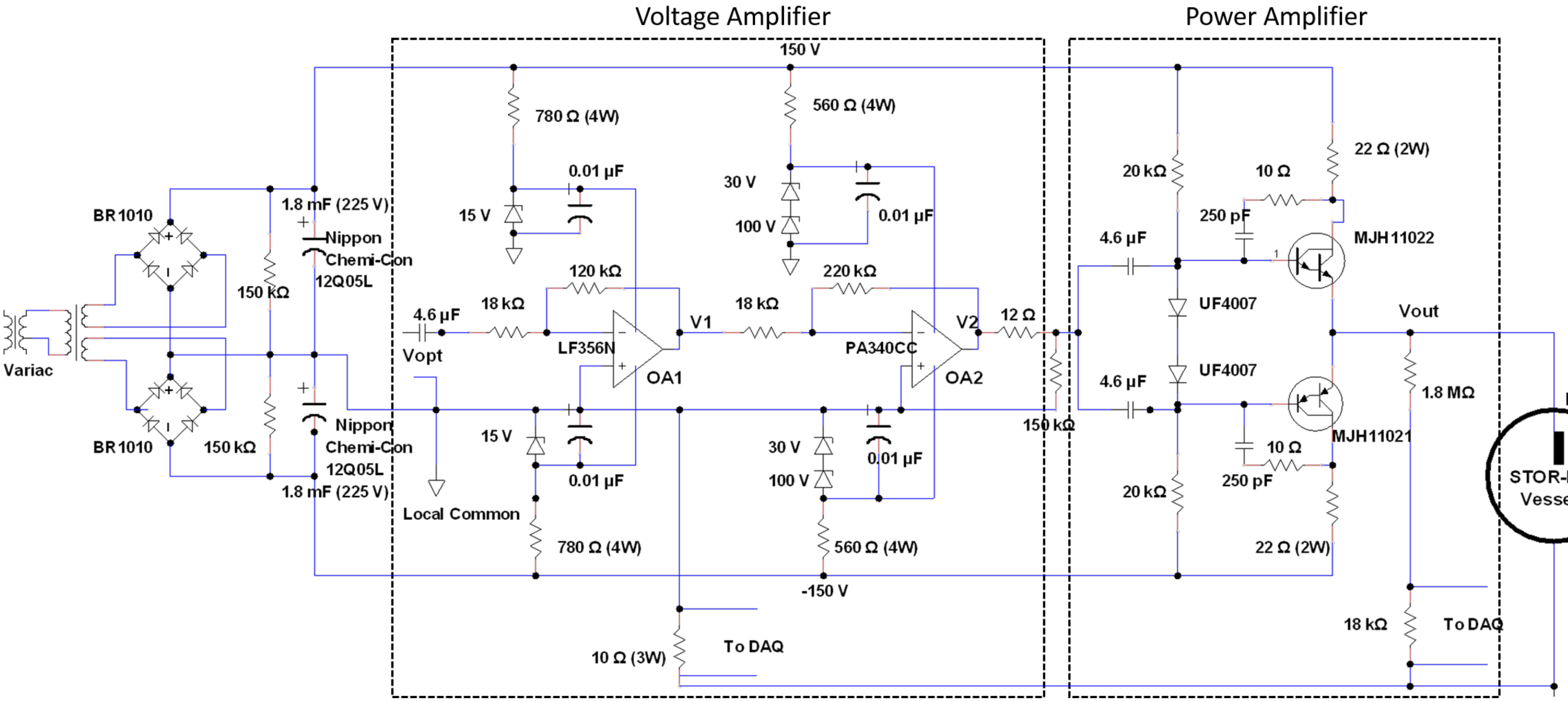

Figure 8.11: Circuit diagram of the power amplifier for the sweeping voltage supply

There are two main sections to the circuit: voltage amplifier and power amplifier. Both systems are powered by + 150 V and - 150 V power supply, which is an AC-DC converter with 1.8 mF capacitor. The supply voltages are then reduced by zener diodes to appropriate values for the op-amps OA1 and OA2.

In the voltage amplifier, the signal from the optoisolator, Vin, is first coupled by a capacitor to cancel the DC offset introduced by the optoisolator circuit. The DC-cancelled signal is amplified by op-amp OA1 in the inverting configuration by a factor of -10, i.e., $\mathrm{V1} = -10\mathrm{Vin}$. Given the function generator input of maximum amplitude 1 V, V1 would be of maximum amplitude 10 V. V1 is then fed to OA2 for further amplification by a factor of -10, i.e., $\mathrm{V2} = -10\mathrm{V1} = 100\mathrm{Vin}$. The second op-amp, OA2, is a high voltage output MOSFET OPAMP PA340CC. It is mainly used for high voltage operation, and maximum voltage range is 350V. Its current output is also high compare to other available op-amps, and its maximum current output is 120mA.

The amplified signal is then coupled to a unity-gain, push-pull power amplifier with NPN and PNP Darlington-pair transistors. The two diodes are used to provide a constant offset voltage between the bases of the two transistors in order to cancel zero crossing. Zero crossing is a phenomenon in which the sweeping signal becomes constant at 0 V for a certain period of time when swinging from positive to negative and vice versa. The offset between the bases keeps both transistors slightly ”on” and minimizes zero crossing. The resistor and capacitor between the base and the collector of each transistor provide feedback and stabilize the output signal. The values of the components were optimized by trial and error. The resulting output, Vout (= 100 Vin), is then connected to a Langmuir probe for electron temperature measurement. The probe voltage is measured by a voltage regulator and the probe current by a current-sensing resistor (10 Ω). The frequency response of the sweeping power supply is shown in Fig. 8.12. As shown in the plots, the bandwidth of this system is 10 Hz - 30 kHz.

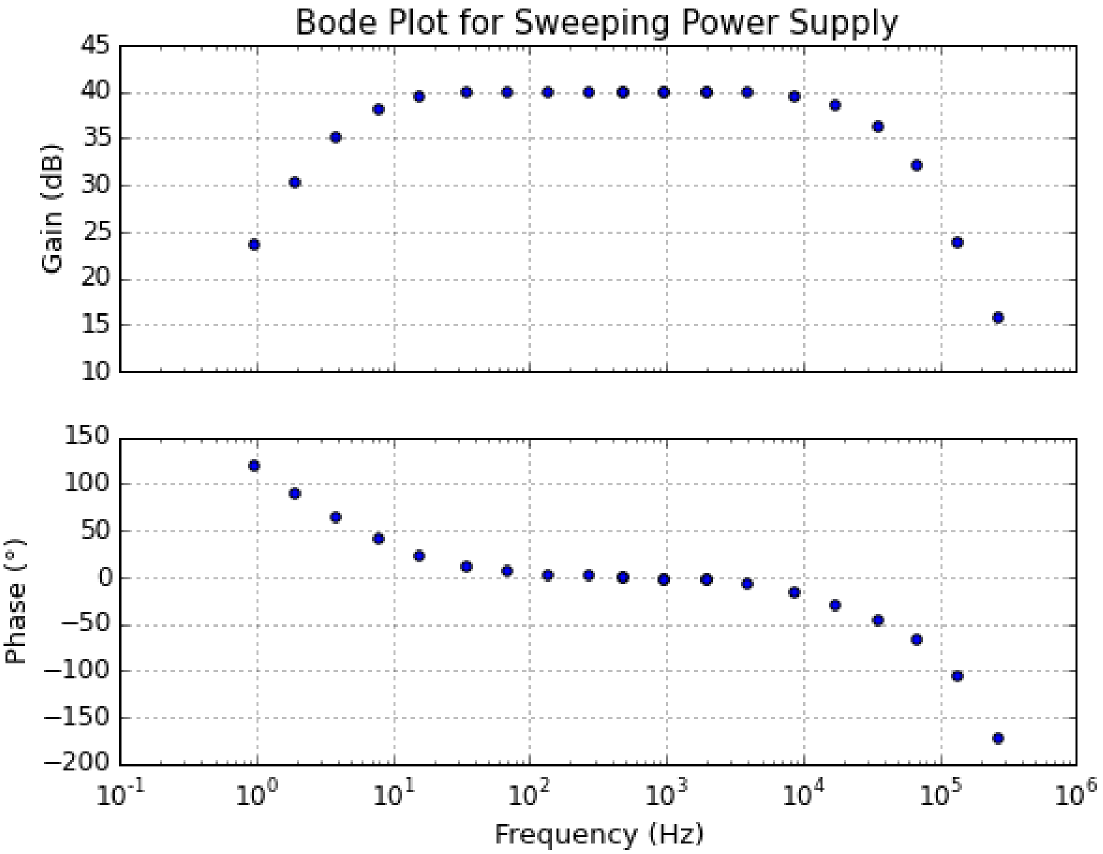

Figure 8.12: Bode plots of sweeping power supply

8.3 Gated DC Power Supply

8.3.1 Electrode Biasing on Tokamak Plasmas

Applying external electric fields on tokamak plasma has been done in many experiments [47, 48]. These experiments showed that applying an external radial electric field could lead to improved particle and energy confinements. This improved state, often called an H-mode (”H” for ”high” confinement), is characterized by sudden decrease in hydrogen light and increase in the plasma density. The reduction in hydrogen light is supposed to be due to reduced plasma flux in the radial direction. A potential mechanism for H-modes is the poloidal rotation of plasma caused by $\mathbf{E_r} \times \mathbf{B}_\phi$ force. While electrode biasing is not the only way to achieve an H-mode, it has been actively studied partially owing to its relatively easy implementation.

Electrode biasing has been done in the STOR-M tokamak, in which an -H-mode was successfully induced [49]. Negative bias was applied by an electrode at a certain time during STOR-M discharges and maintained until the end of the discharges. The results included increased electron density, increased energy confinement, decreased H-α emission, and decreased floating potential.

8.3.2 Purpose of Gated DC Supply Development

Our purpose for using a bias system is not only to induce an H-mode but also to study possible change in density and potential fluctuations at the edge of the STOR-M tokamak plasma. As zonal flow and geodesic acoustic mode are driven by radial electric field, electrode biasing could affect such modes. For example, if biasing suppresses drift turbulence, one would also expect suppression of geodesic acoustic mode.

In order to elucidate the effect of biasing, we needed a power supply system which can be gated to a certain period of time, instead of continuous bias after turning on. Such system would allow the study of fluctuations before, during, and after the electrode biasing.

8.3.3 Gated DC Bias Supply Circuit

The overall schematics of the gated DC bias system is shown in Fig. 8.13. There are two capacitor banks in the system: the main capacitor (C_{main}) and the stopping capacitor (C_{stop}), which are charged to adjustable voltages with polarities shown in the figure. The power for the biasing is provided by C_{main}, which is first triggered by SCR1. The bias is applied until SCR2 is triggered, when a reverse bias is applied across SCR1 in order to turn if off. The current flows through SCR2 and decays exponentially with factor R_pC_{stop}, where R_p is the effective plasma resistance. In actual experiments, the value of C_stop is adjusted such that the $R_pC_{stop} \simeq 1ms$. The polarity of the bias can be changed by manually switching the two leads. The charging system and the triggering system are described below.

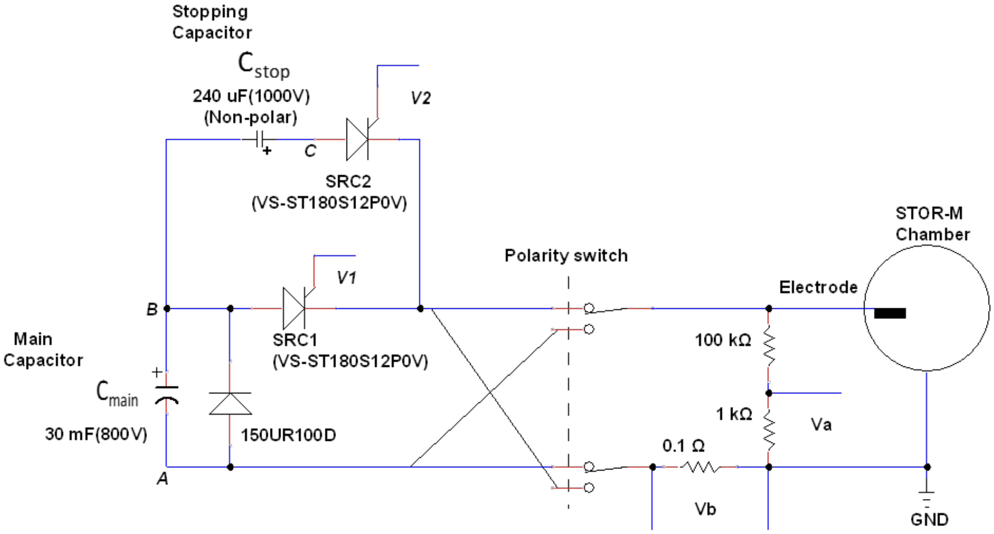

Figure 8.13: Schematics of the DC Bias System

8.3.4 Bias Supply Charging System

The circuit diagram of the charging circuit for the gated DC bias supply is shown in Fig. 8.14.

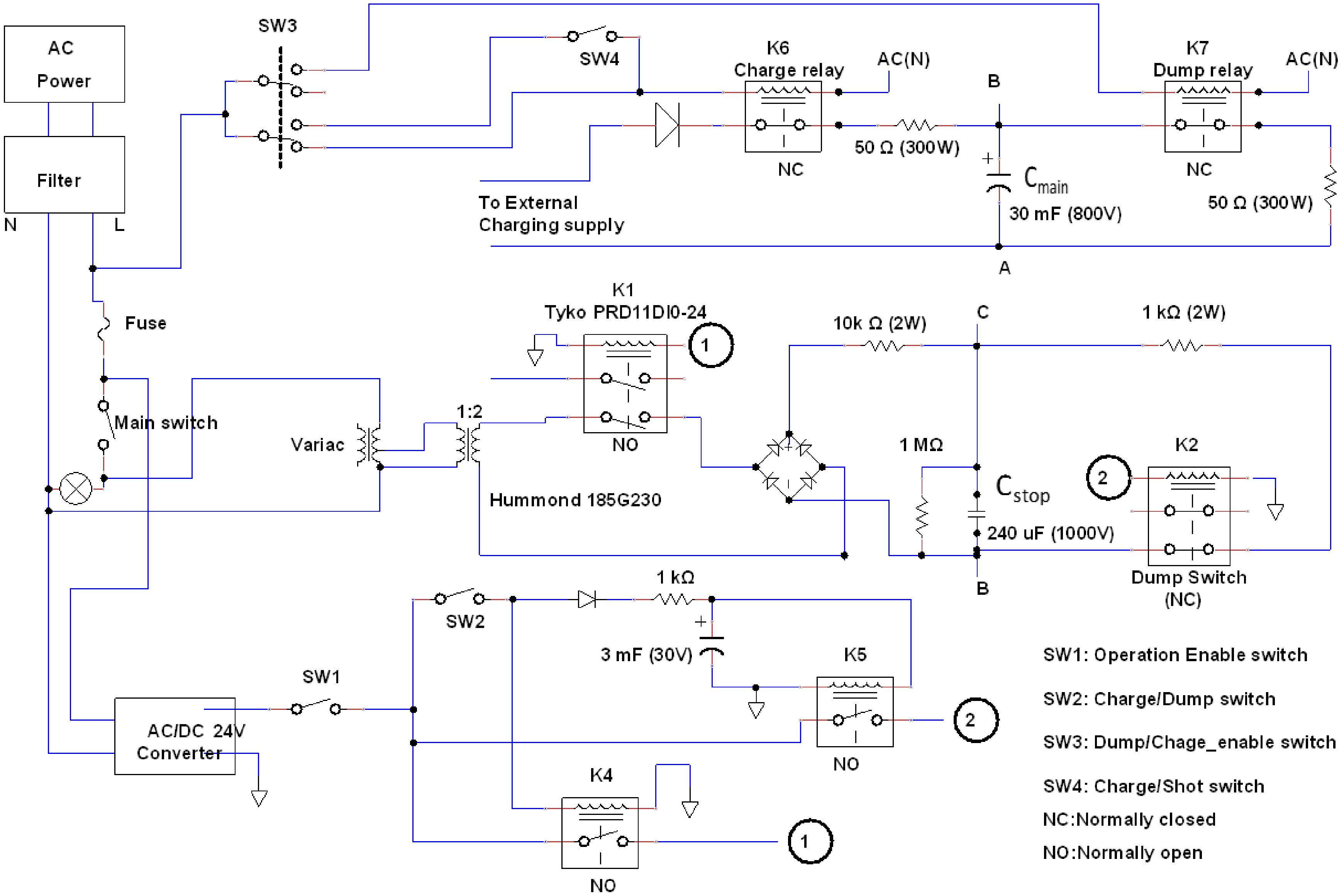

Figure 8.14: Schematics of the DC Bias charging system

The points A, B, and C correspond to those shown in Fig. 8.13. In the figure, the relays are shown as in their non-energized configurations. The main capacitor bank, C_{main}, is charged by an external charging supply, whose voltage is can be varied. The stopping capacitor, C_{stop}, is charged by an AC-DC converter fed by a variable transformer. Each bank is has relays for charging and dumping.

8.3.5 Bias Supply Triggering System

The circuit diagram of the triggering circuit for the gated DC bias supply is shown in Fig. 8.15.

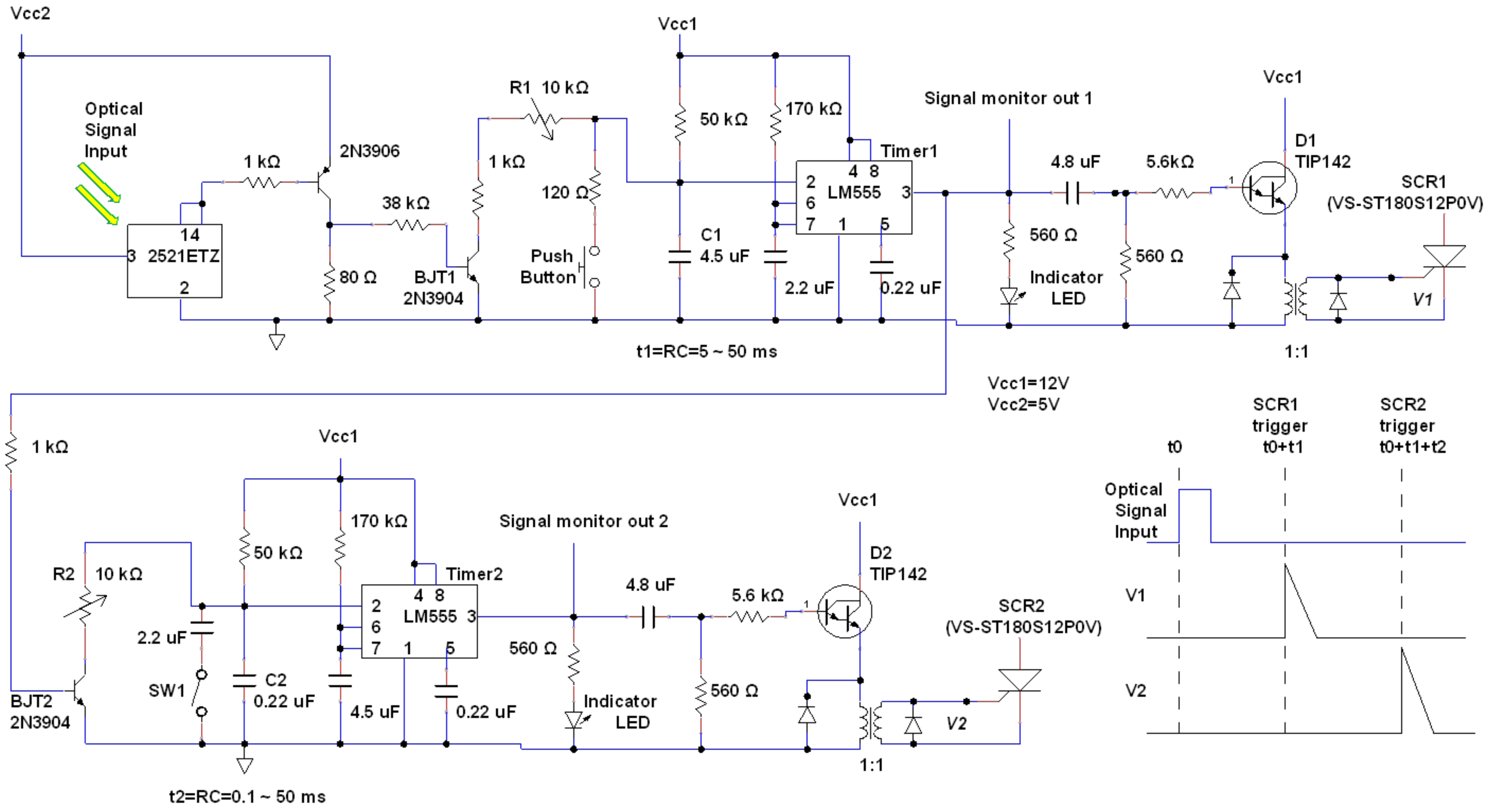

Figure 8.15: Schematics of the DC Bias triggering system

The function of this circuit is to receive an optical pulse and to produce two trigger pulses, for SCR1 and SCR2, at controllable times. In other words, defining the time of the input optical pulse to be $t = t_0$, this circuit produces a triggering pulse for SCR1 at $t = t_0 + t_1$ and for SCR2 at $t = t_0 + t_1 + t_2$, which are illustrated in the figure. First, the optical receiver receives the optical signal from the STOR-M control room and turns on BJT1. The capacitor, which is normally charged to V_{cc}, is discharged through R1. When the voltage across C1 becomes below $\frac{V_{cc}}{3}$, Timer1, in the monostable configuration, turns on. The output of Timer 1 turns on two components: D1, a Darlington-pair BJT, and BJT2. The current pulse through D1 is transmitted by a pulse transformer which applied the triggering pulse (V1) on SCR1. Timer2 is turned on with some delay (t_2) by the same mechanism and triggers SCR2. The timings, t_1 and t_2, are varied by changing the resistors R_1 and R_2. The push button is for manual triggering. SW1 is for adding capacitance and changing the scale of t_2. The two LED's are for visually checking the timer outputs. The maximum output voltage is 400 V at 20 A.

8.4 Graphical User Interface for Data Anaysis

We developed a graphical user interface in order to efficiently analyse the data obtained from each STOR-M plasma discharge. During operation, the STOR-M makes a plasma discharge every 5 minutes. Therefore, it is convenient to be able to analyse the data of each discharge quickly; it allows a quick modification of the discharge configuration based on the analysis. Toward this goal, we used the Python programs to develop a graphical user interface (GUI).

The framework of the interface is PyQt [50], which is the application of Qt software in Python framework. The main window of the GUI is shown in Fig. 8.16.

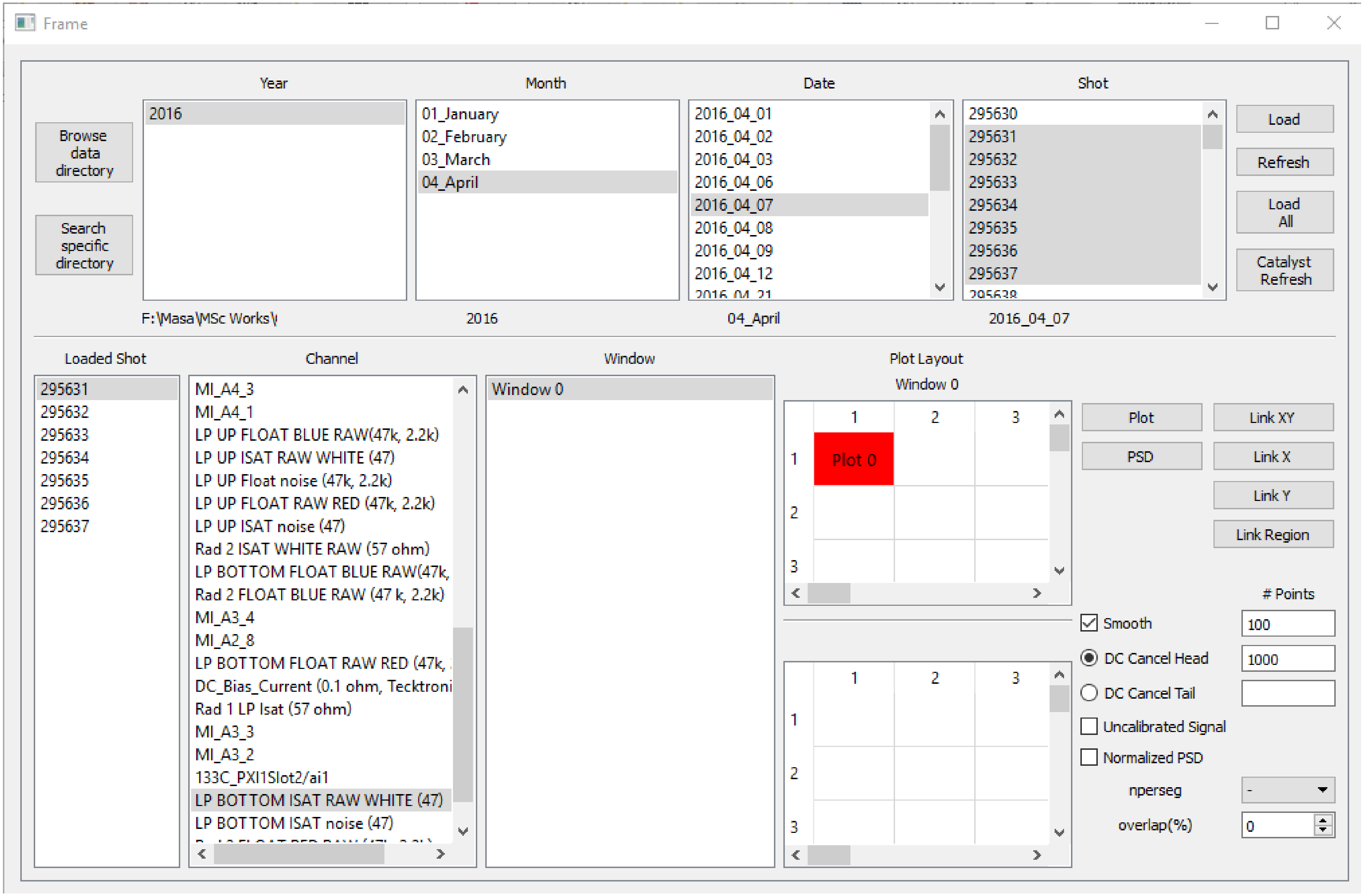

Frame

Year: 2016

Month: 01_January, 02_February, 03_March, 04_April

Date: 2016_04_01, 2016_04_02, 2016_04_03, 2016_04_06, 2016_04_07, 2016_04_08, 2016_04_09, 2016_04_12, 2016_04_21

Shot: 295630, 295631, 295632, 295633, 295634, 295635, 295636, 295637, 295638

F:\Masa\MSc Works\ | 2016 | 04_April | 2016_04_07

Loaded Shot: 295631, 295632, 295633, 295634, 295635, 295636, 295637

Channel:
MI_A4_3
MI_A4_1
LP UP FLOAT BLUE RAW(47k, 2.2k)
LP UP ISAT RAW WHITE (47)
LP UP Float noise (47k, 2.2k)
LP UP FLOAT RAW RED (47k, 2.2k)
LP UP ISAT noise (47)
Rad 2 ISAT WHITE RAW (57 ohm)
LP BOTTOM FLOAT BLUE RAW(47k,
Rad 2 FLOAT BLUE RAW (47 k, 2.2k)
MI_A3_4
MI_A2_8
LP BOTTOM FLOAT RAW RED (47k,
DC_Bias_Current (0.1 ohm, Tecktroni
Rad 1 LP Isat (57 ohm)
MI_A3_3
MI_A3_2
133C_PXI1Slot2/ai1
LP BOTTOM ISAT RAW WHITE (47)
LP BOTTOM ISAT noise (47)

Window: Window 0

Plot Layout: Window 0

Plot 0

☑ Smooth — # Points: 100

● DC Cancel Head — 1000

○ DC Cancel Tail

☐ Uncalibrated Signal

☐ Normalized PSD

nperseg: -

overlap(%): 0

Figure 8.16: The main page of the graphical use interface for data analysis

The main functions of the interface are as follows.

1. Browse the data locations
2. Load raw data for selected discharges (or shots)
3. Plot the data on interactive graphs

The main library used for plotting was PyQtGraph [51], which creates interactive graphs. An example of a plot made by the interface is shown in Fig. 8.17. We used this interface to quickly analyse the data from STOR-M discharges. For example, in order to ensure that the Langmuir probes in different locations were on a same magnetic flux surface, it was necessary to move the probes such that the ion saturation currents matched. For this goal, we plotted the ion saturation current data of each discharge, compared them, and changed the probe locations accordingly. We also used the interface to analyse the power spectral densities of the signals.

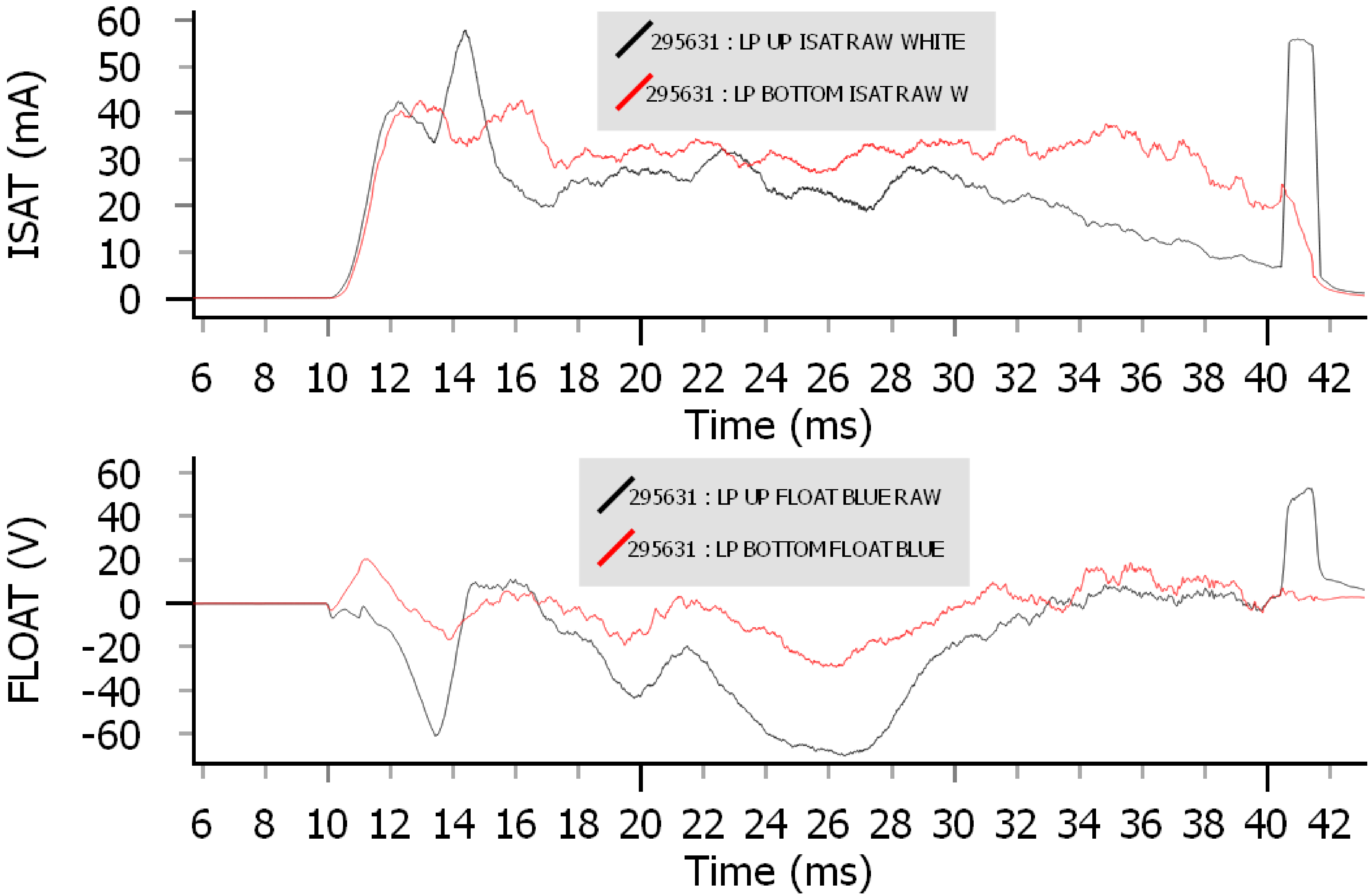

Figure 8.17: An example of a plot created by the interface. The axes can be translated and rescaled.

Chapter 9

Experimental Set-up

Experiment for conventional GAM detection requires measurement of poloidal and toroidal mode numbers for floating potential fluctuations as well as density fluctuations. Primarily, it is aimed to measure plasma parameters at the edge of STOR-M discharge. The specific objectives were to 1) use Langmuir probes to measure ion saturation current fluctuation, which provides information about density fluctuation, and floating potential, 2) study the mode numbers of such fluctuations, 3) study radial dependence of the magnitude of the oscillations, and 4) study the temperature dependence of the frequency of the fluctuations. For these objectives, we used Langmuir probe systems, installed in different locations of STOR-M.

9.1 Langmuir Probe System

The Langmuir probe system we used in our experiment is shown in Fig. 9.1. A linear feedthrough is part of the probe system for adjusting the radial location of the probe (Fig. 9.1.a). There are four electrical probe tips in the corners of a square (Fig. 9.1.b), mounted in a teflon material which is inserted in a ceramic tube. The dimensions of the probe tips are as shown in Fig. 9.1.c. Each probe tip is electrically connected to the center pin of a BNC connector. The outer parts of the BNC connectors are connected to the STOR-M chamber, which is grounded. Different measurements can be made by connecting the BNC connectors to different configurations. The configurations used in our experiment

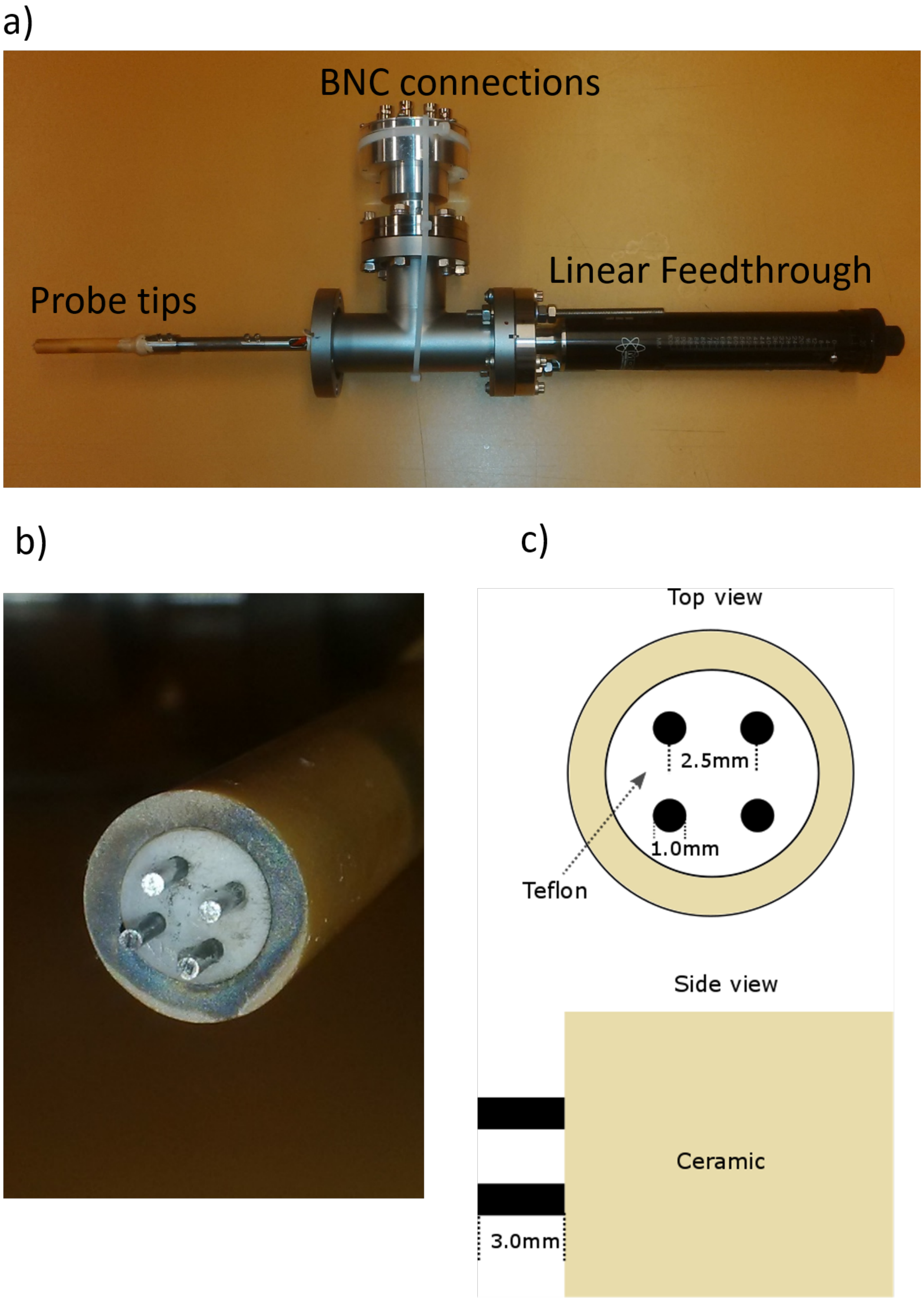

Figure 9.1: Pictures of a Langmuir probe system: a)Picture of the entire Langmuir probe system, b) Picture of the probe tips, and c) Dimensions of probe tips.

are described in the following subsection.

9.1.1 Parametric Measurements by Langmuir Probe Systems

In this experiment three types of measurements were made using Langmuir probes: floating potential, ion saturation current, and I-V characteristics. Fig. 9.2 shows the schematics of measuring floating potential. A simple voltage divider was used to measure the floating potential attenuated by a factor of 0.045. Floating potential in a typical STOR-M discharge ranges from $-80V$ to $+80V$, which corresponds to a few milliamps. This current is smaller than typical ion saturation current of order tens to hundreds of milliamperes, ensuring that the approximation of $I \simeq 0$ for the floating potential measurement is valid.

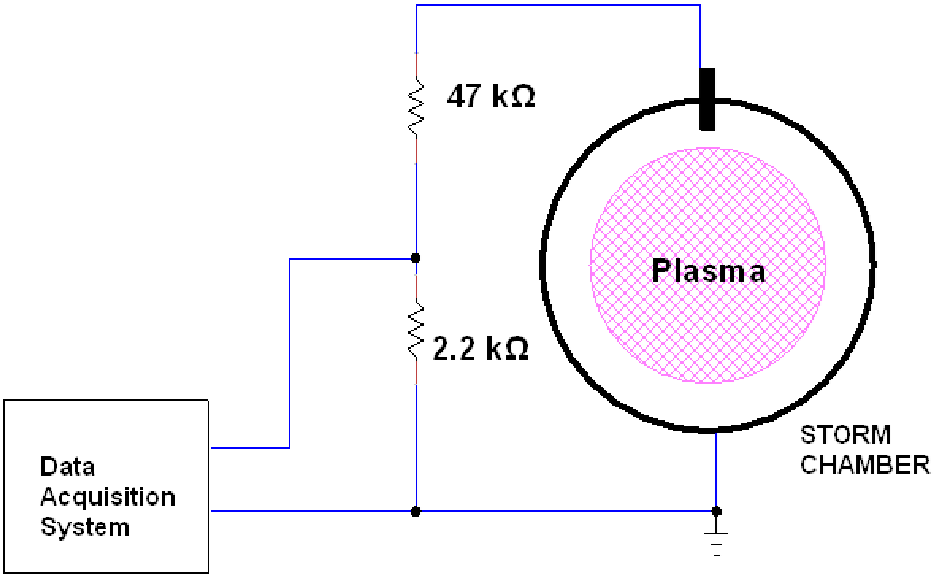

Figure 9.2: Diagram for floating potential measurement

Fig. 9.3 shows the schematics of the ion saturation current measurement. A stack of 9.5 V batteries was used to apply a negative bias to the probe with respect to the grounded STOR-M chamber. A mechanical selector was connected to vary the bias voltage from -95 V to -57 V in steps of 9.5 V. The probe current was measured by a current sensing resistor of 46 Ω.

Fig. 9.4 shows the schematics of the I-V characteristics measurement. A sweeping voltage supply (section 8.2) was used to apply time-varying probe potential. A voltage divider was used to measure the probe potential attenuated by a factor of 0.01, and the probe current was measured by a 10 Ω current sensing resistor. Each of the two signals was fed to a

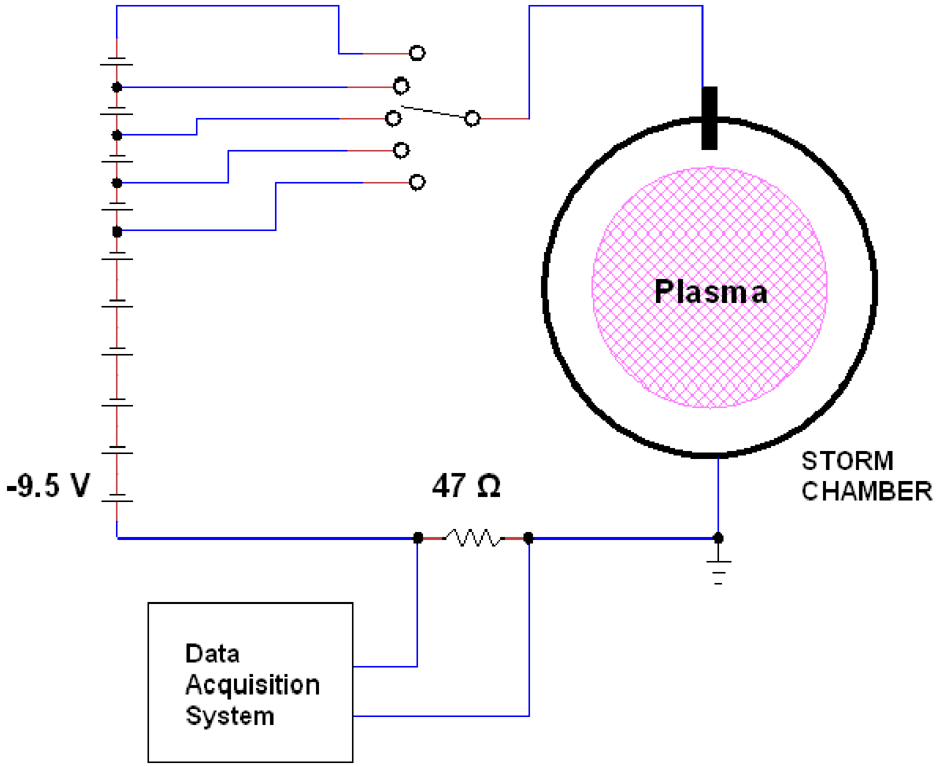

Figure 9.3: Diagram for ion saturation current measurement

differential optoisolator system (section 8.1) to cancel the common mode noise. The probe current and voltage data were then used to make a I-V characteristic curve for determining the electron temperature.

9.1.2 Probe locations

We used total of four Langmuir probe systems, situated in different locations. The locations of the probe systems are shown in Fig. 9.5. Viewing STOR-M from top, there are two toroidal locations for the Langmuir probe systems: one system in one toroidal location and three systems in another toroidal location. Probe system RADIAL1 is inserted from a radial direction. At the other toroidal location, separated by $\pi/2$, there are three probe systems. In the cross-sectional view at this toroidal location, three probes are inserted from three different poloidal locations, i.e., from top (TOP), bottom (BOTTOM), and radial (RADIAL2) directions. This allows the mode number studies in toroidal and poloidal directions. With each probe system equipped with 4 probe tips, there are total of 16 probe tips, each of which

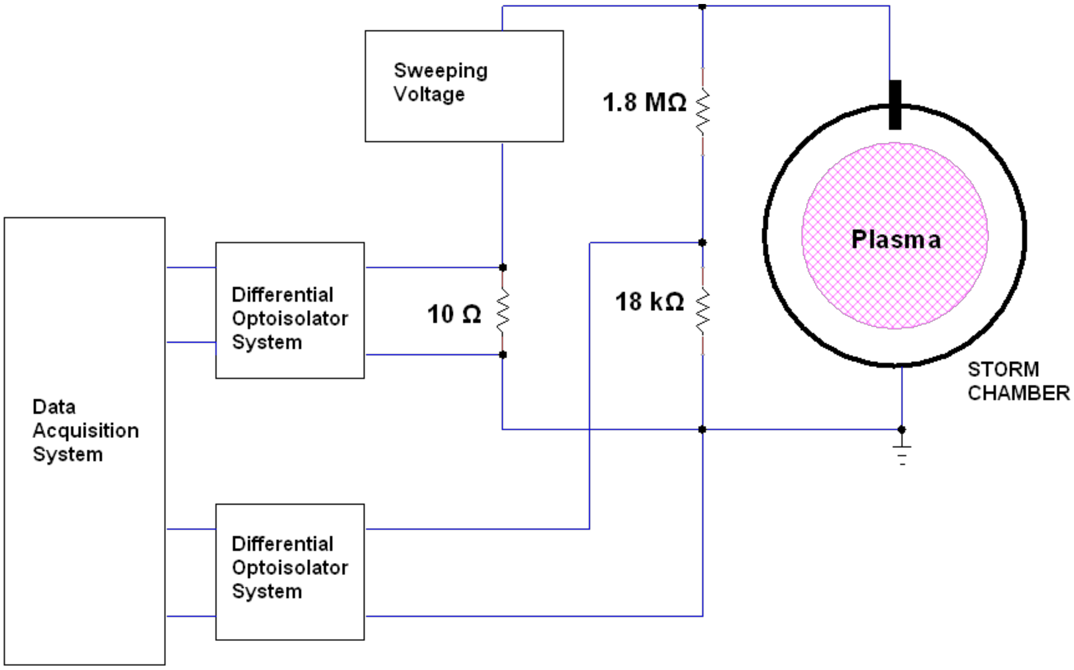

Figure 9.4: Diagram for I-V characteristics measurement

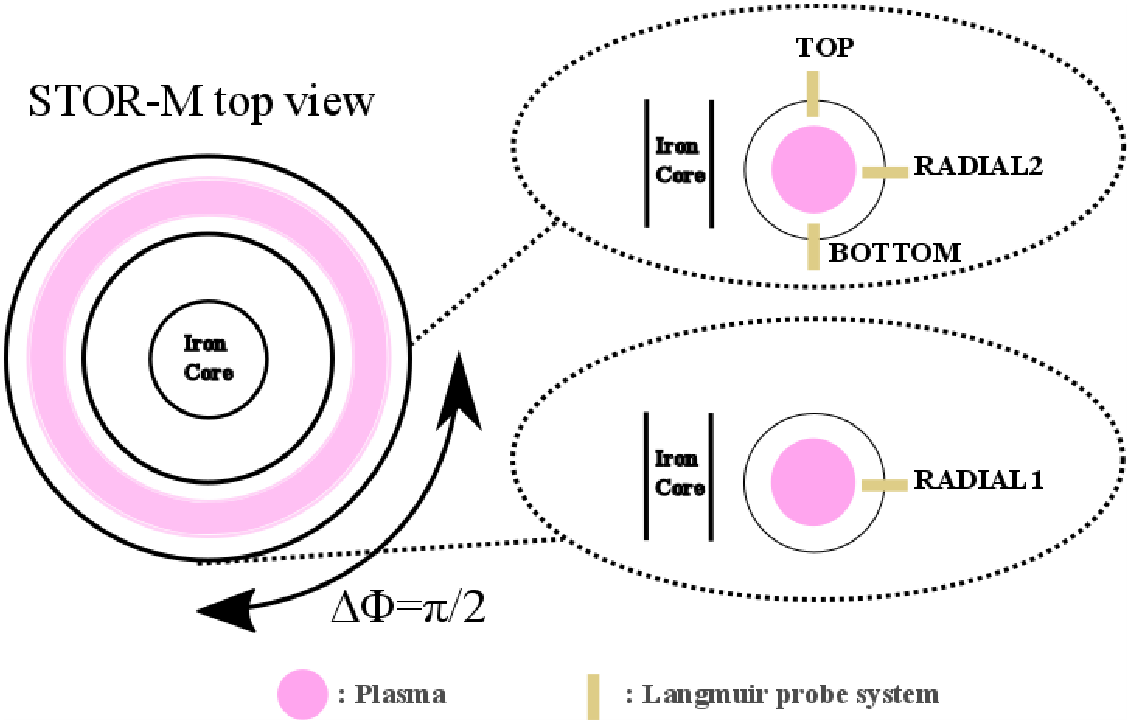

Figure 9.5: The locations of the four Langmuir probe systems. Brown bar represents a Langmuir probe system.

can be used for either of the three types of measurements introduced above.

9.2 Summary of Experimental Set-up

In order to detect GAM, we set up the Langmuir probe systems in four locations. With the experimental set-up thus described, the objectives for the experiment are accomplished in the following manner. Objective 1) is accomplished by using the Langmuir probe systems with some tips connected to ion saturation and floating potential configuration. Objective 2) is accomplished by comparing the fluctuation signals from probe systems situated at different toroidal and poloidal locations. Objective 3) is accomplished by moving the radial locations of the probes by the linear feedthroughs and taking the measurements at different radial locations. Finally, objective 4) is accomplished by using one probe tip for I-V characteristic measurement and others for ion saturation and floating potential measurements.

Chapter 10

Results and Discussions

As stated in the previous chapter, the main aim of the experiment was to detect GAM in the STOR-M tokamak. For this purpose, we made plasma discharges in the machine and recorded the data for various parameters. Along with the basics parameters, we collected fluctuations in floating potential and ion saturation current by Langmuir probe systems located in four locations. We also used Langmuir probes to measure the I-V characteristics at the edge for the electron temperature calculation. This chapter reports the results obtained from the experiment and their implications.

10.1 Raw Signal Analysis

As in any experiments with a tokamak, our first challenge was to condition a plasma in STOR-M. This task was more difficult than usual since the Langmuir probes at the four locations could introduce impurities which would affect the confinement of the plasma. We overcame the difficulty by techniques called glow discharge and discharge cleaning, which cleaned the probe tips and reduced the impurities. The basic parameters of a typical STOR-M discharge after the cleaning process are shown in Fig. 10.1.

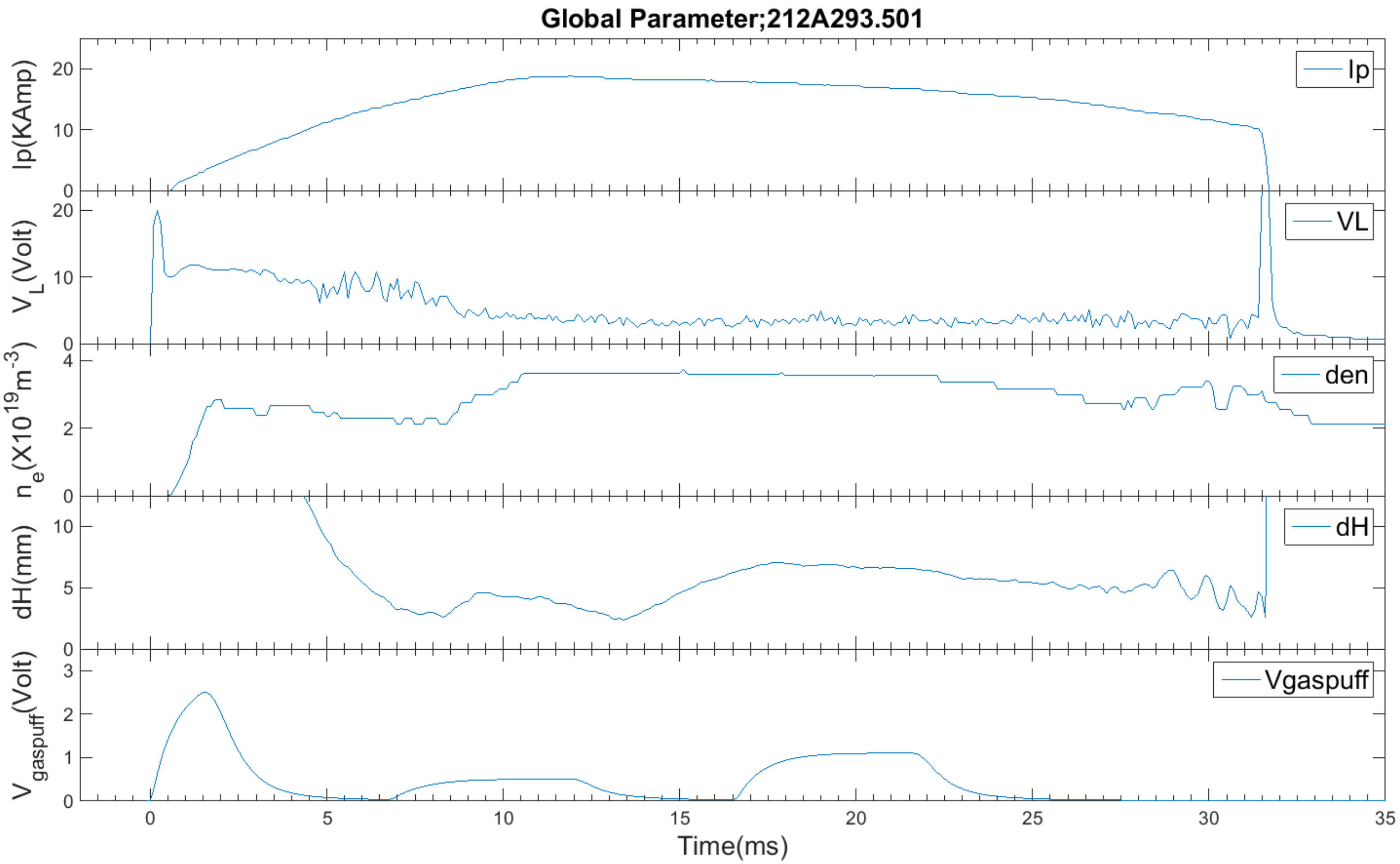

Figure 10.1: The global parameters of a typical STOR-M discharge

Here, I_p stands for the plasma current in the toroidal direction. The plasma current increases from 0 ms to 10 ms, and this period is called the ramp-up region. After 10 ms, the current is kept more or less constant for about 10 ms. This part of the discharge is called the flat-top region. I_p gradually decreases and comes to a relatively quick halt around 33 ms. V_L is the loop voltage taken across one loop in the toroidal direction. Together with the plasma current, loop voltage indicates the power dissipated by the plasma. V_L decreases in the ramp-up region and assumes a steady value around 3 V from the flat-top region onward. In the figure, n_e indicates the number density of electrons averaged over diameter of the plasma column. In the flat top region, n_e is constant around $4 \times 10^{19}\ m^{-3}$. The horizontal displacement of the plasma column from the geometrical center of the chamber is indicated by dH. The figure shows that, from 5 ms onward, the displacement is kept around 5 mm, which is about 4 % of the shortest minor radius of the limiter (Fig. 5.1). This indicates that the plasma column is confined around the center of the vacuum chamber through the discharge. $C_{gaspuff}$ indicates the pulses used to inject hydrogen gas into the chamber. Gas puff pulses can be changed to modify the plasma density to some extent.

After setting up "clean" plasmas, our next challenge was to adjust the probe locations such that all the probe tips were on the same magnetic surface, i.e., the surface of constant pressure. This requires the measurement of ion saturation current and electron temperature at each location. We found, however, that applying sweeping voltage simultaneously at multiple probe locations degraded the plasma. Therefore, we used the assumption that the temperature was same at each probe location and adjusted the probe locations such that the values of ion saturation current at the four locations were close to each other. An example of optimized locations of the four probe systems are shown in Fig. 10.2. The figure shows the cross sections of two toroidal locations where Langmuir probe systems are inserted. The gray area indicates the area occupied by the limiter (Fig. 5.2). Note that the two probe system at the radial locations (Radial 1 and Radial 2) were located more than 1 centimetre away from the center than Top and Bottom probe systems. At each of the shown locations, we measured floating potential and ion saturation current.

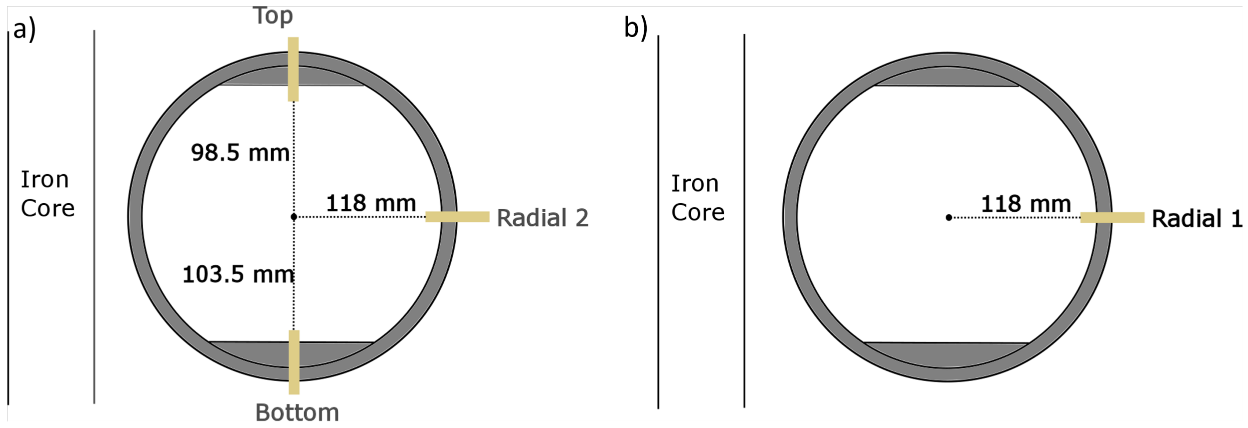

Figure 10.2: Radial locations of the Langmuir probe systems

The raw and smoothed (over 0.1 ms) signals of ion saturation current at the four locations are shown in Fig. 10.3. The raw signals contain a spectrum of frequencies, including noise (Fig. 10.3.a). In order to compared the average values of ion saturation current, each signal was smoothed by running mean method with time window of 0.1 ms (Fig. 10.3.b). The smooth signals indicate that that the values of ion saturation current at the four locations stay within about 15 mA from each other in the time window from 8 ms to 23 ms. As noted above, the locations of the two radial probes were further away from the center than those of the Tom and Bottom probes, yet the ion saturation current values of the four locations were close to each other. A possible explanation for this result is that, if the shape of the plasma column was circular, then there would be some room in the horizontal direction for the plasma column to move.

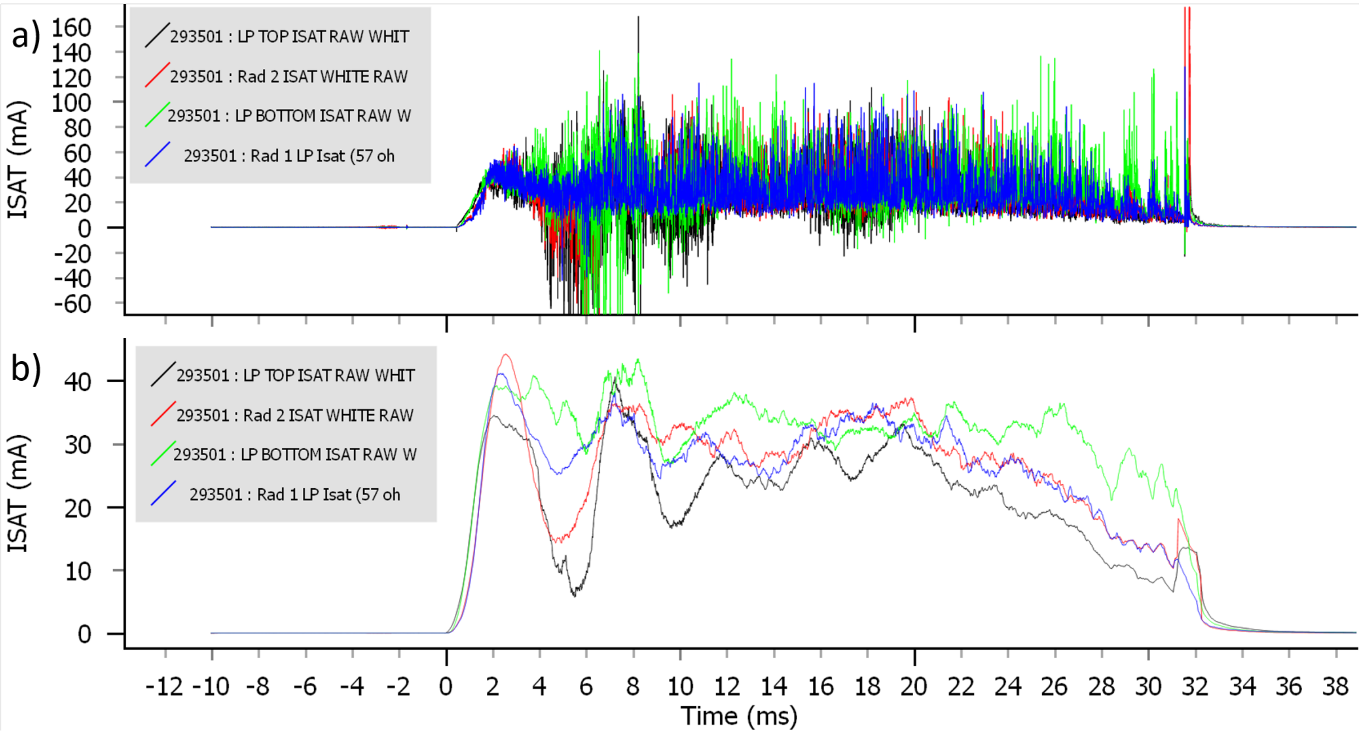

Figure 10.3: Raw and smoothed (over 0.1 ms) signals of ion saturation current at four locations.

This situation is shown in Fig. 10.4.a. In this scenario, the plasma column can move toward the radial probes (outward) so that the plasma densities (thus ion saturation current) at the four locations are similar. Another possibility is that the plasma column may take an elliptical shape. This is shown in Fig. 10.4.b. In this case, the plasma edge elongates in the horizontal direction, which would explain the fact that the radial probes, though situated farther from the center, had ion saturation current values similar to those of Top and Bottom probes.

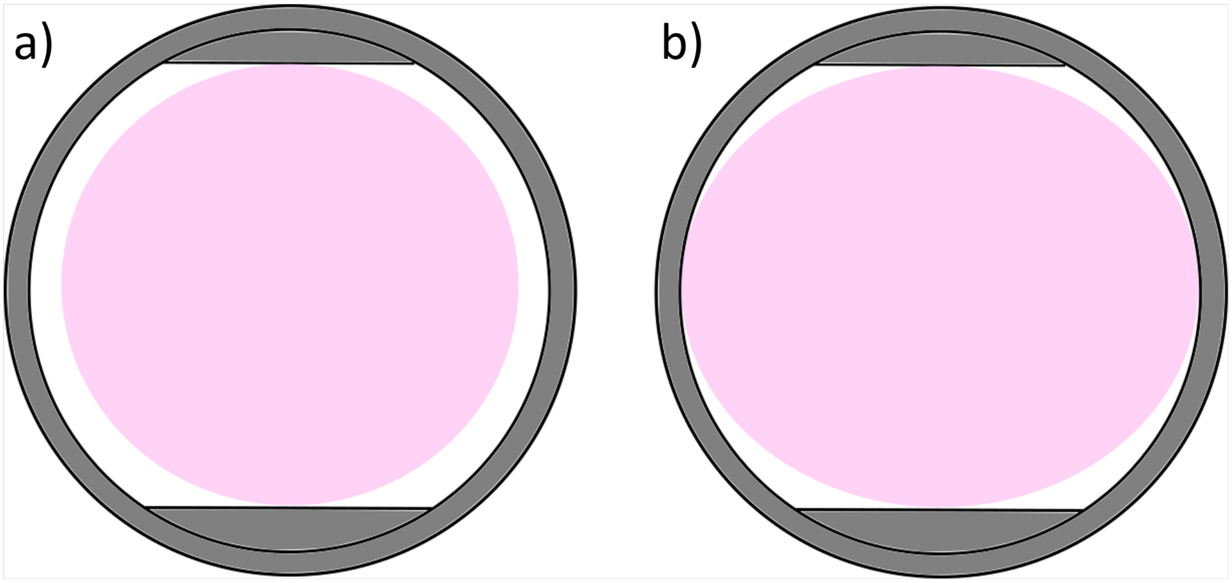

Figure 10.4: Possible shapes of plasma column.

The same analysis was done for floating potential (Fig. 10.5). As shown in the Fig. 10.5.b, the floating potential at any location was negative for most of the discharge. Unlike ion saturation current, floating potential varied from location to location. Around 10 ms, the differences between Top probe and the other probes were more than double. After the flat-top region, the floating potential values stayed close to each other until the end of the discharge.

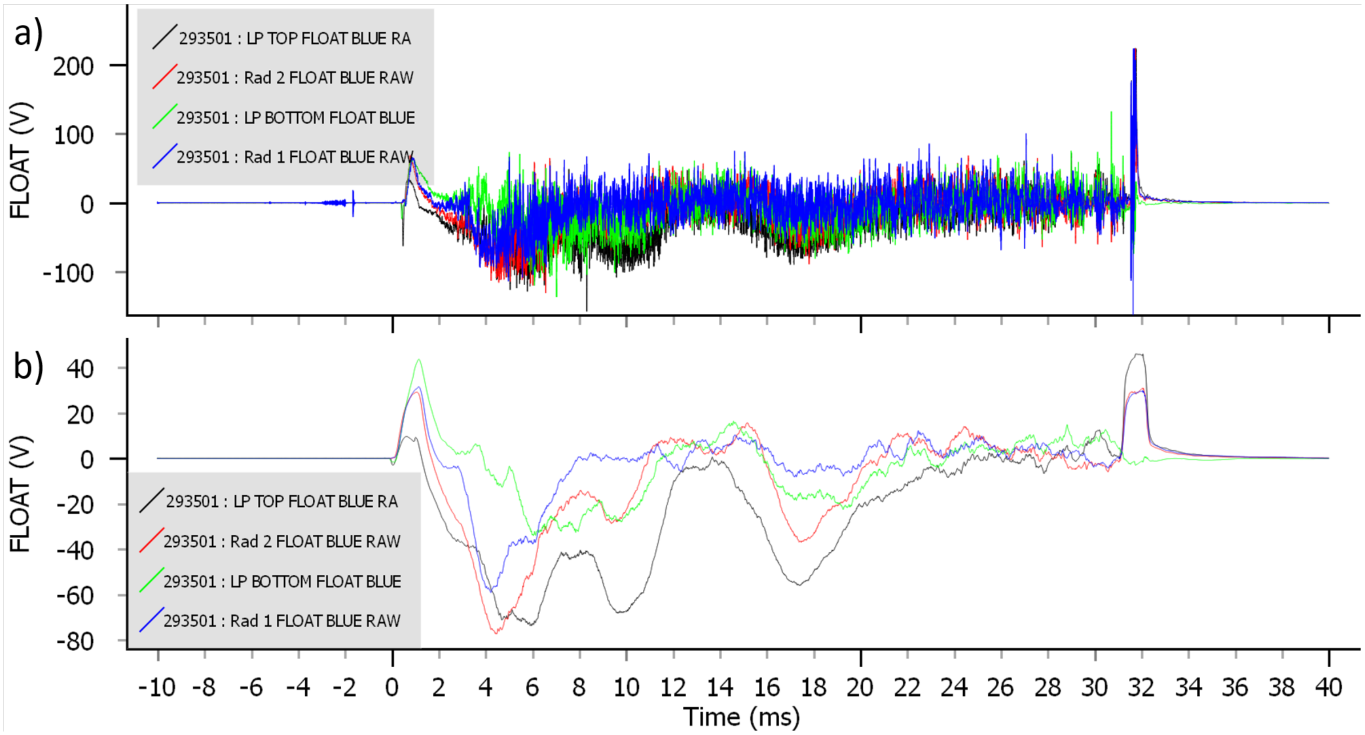

Figure 10.5: Raw and smoothed (over 0.1 ms) signals of floating potential at four locations.

10.2 Spectral Analysis

Having established that the four probes were approximately on the same magnetic surface, we analysed the frequency components in the signals of ion saturation current and floating potential. Using the signal processing methods introduced in chapter 7, this section discusses the power spectral densities and cross spectral densities of the signals for ion saturation current and floating potential.

10.2.1 Spectral Analysis for Ion Saturation Current

In this subsection, the spectral analysis for the ion saturation current signals is discussed. The normalized power spectral densities of ion saturation current at the four locations are shown in Fig. 10.6. Fig. 10.6.a shows the raw signals and the time window (in blue) for which the power spectral densities were calculated. Fig. 10.6.b indicates that the dominant peak is around 30 kHz. A zoomed spectrum is shown in Fig. 10.6.c. The figure indicates that, while the power spectral densities of ion saturation current at Top probe and Bottom probe are high, those at Radial 1 and Radial 2 are low. This result verifies one of the features of GAM (Eq. 4.3.13), i.e., the dependence of the magnitude of density fluctuation on the poloidal angle ($\theta = 0$ at the radial locations).

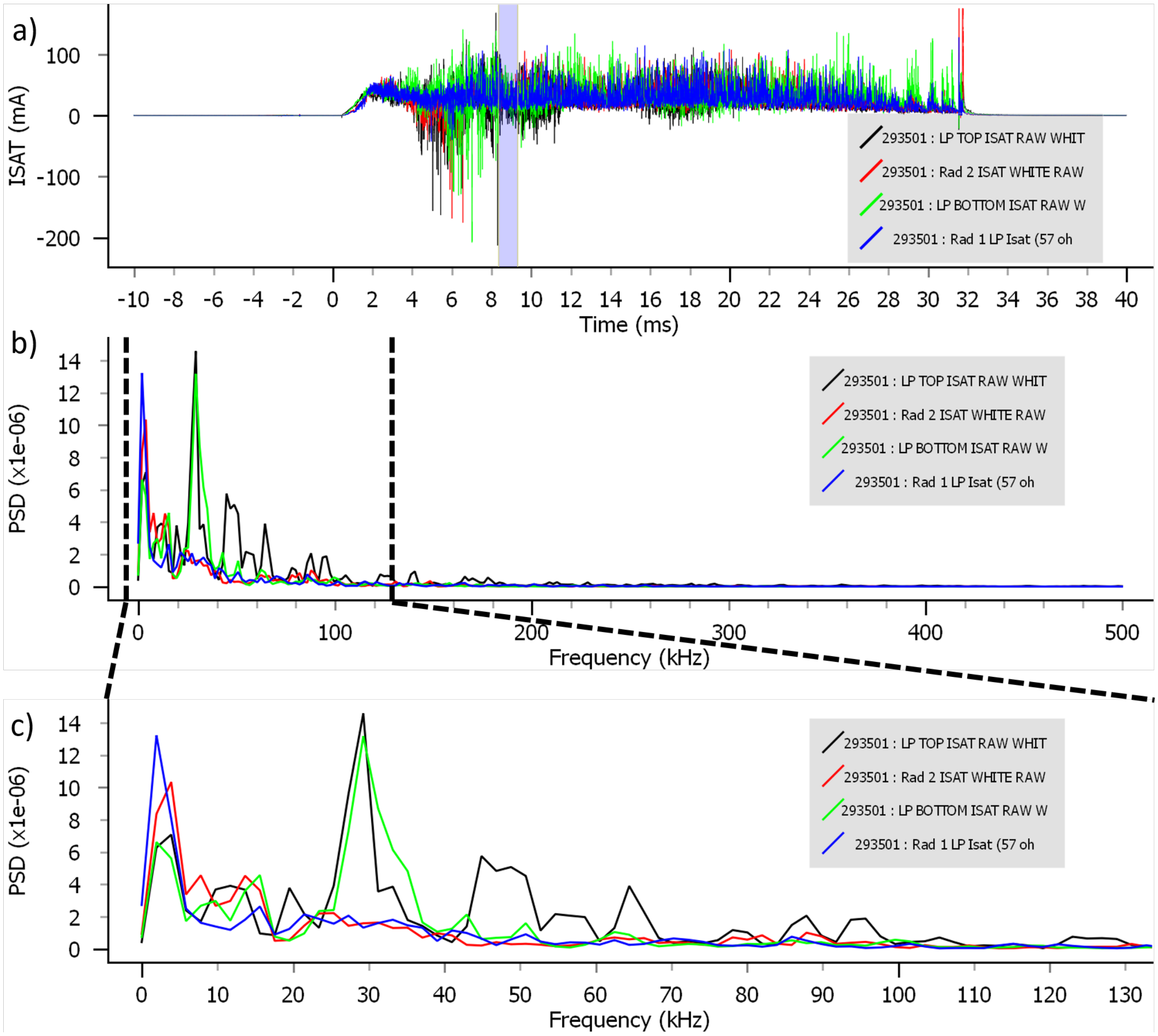

Figure 10.6: Normalized power spectral density of ion saturation current at the four locations around 9 ms.

The above feature of ion saturation current was not found in other time windows. For example, around 14 ms, there was not even a peak around 30 kHz at any probe location (Fig. 10.7). In many STOR-M discharges, the signature shown in Fig. 10.6 was often found around 9 ms, which is the end of ramp-up region and beginning of the flat-top region.

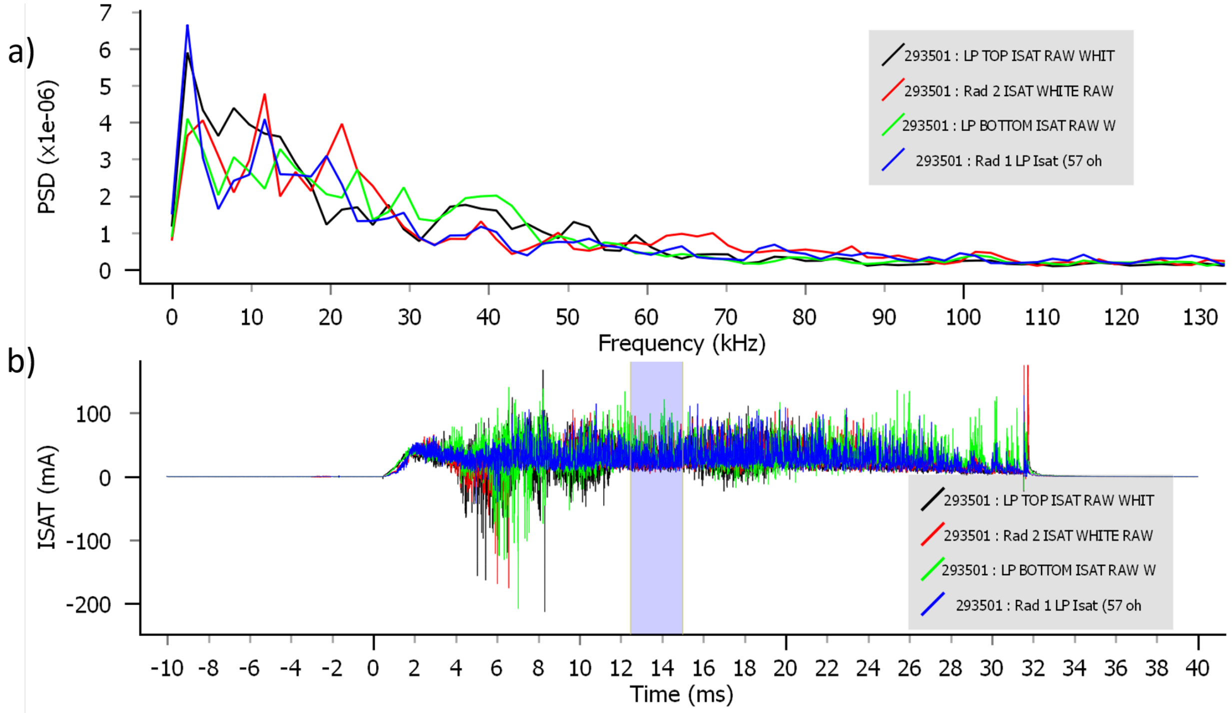

Figure 10.7: Normalized power spectral density of ion saturation current at the four locations around 14 ms.

We now focus on the time region around 9 ms, in which a signature of GAM was found in the previous analysis on the spectral power densities of ion saturation current. For all the cross spectral analysis, the number of Fast Fourier Transform was 512, which corresponds to a frequency resolution of about 2 kHz. To further analyse the 30 kHz peak found in Fig. 10.6, we compare pairs of the ion saturation current signals and analyse their cross spectral parameters. The cross spectral analysis of ion saturation current signals of Top and Bottom probes is shown in Fig. 10.8. Fig. 10.8.d shows the raw signals of ion saturation current at the Top and Bottom probes and the time window (in blue) for which the cross spectral analysis was done. Fig. 10.8.a shows the magnitude of cross spectral density (CSD), which indicates a clear peak around 30 kHz. This suggests that the frequency component of 30 kHz is dominant in both signals. Fig. 10.8.b shows the coherence (Coh) for the Top and Bottom ion saturation current signals. A local peak around 30 kHz is also present in the coherence spectrum. This shows that the phase difference between the two signals are relatively constant for the frequency 30 kHz. The corresponding phase is around -0.9π (Fig. 10.8.c), which suggests the poloidal mode number of $m = 1, 3, 5, \ldots$.

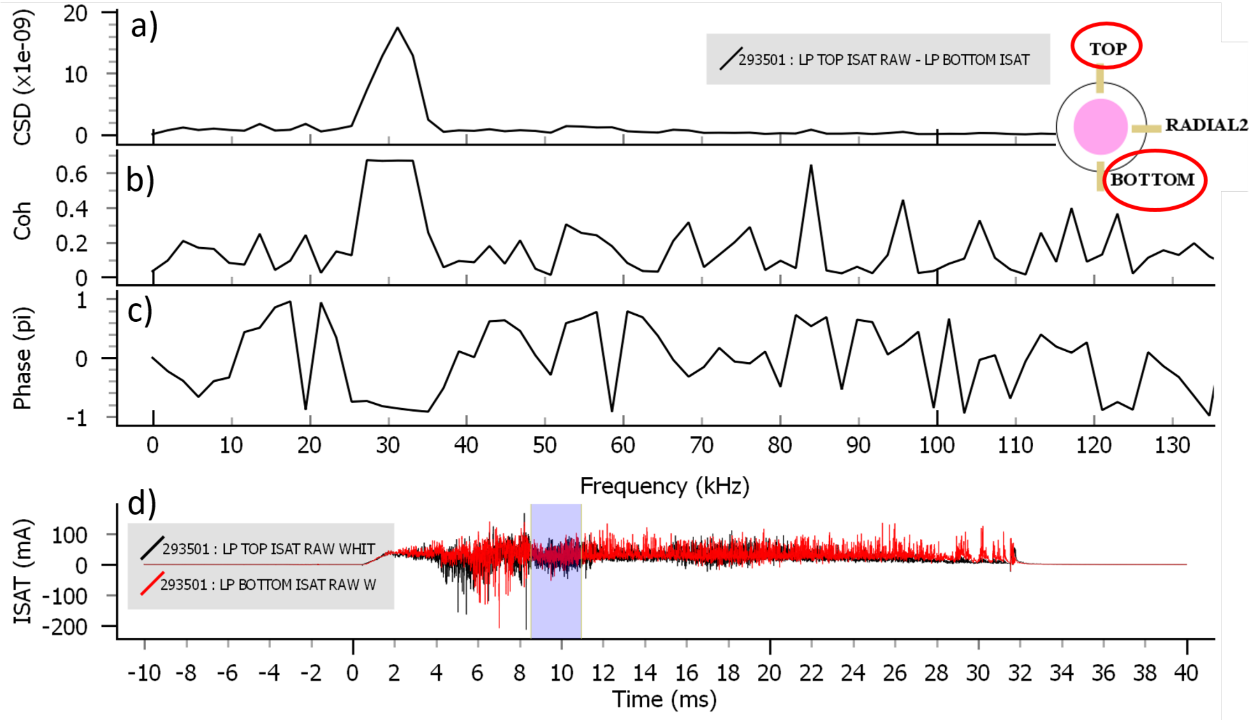

Figure 10.8: Cross spectral analysis of ion saturation current between Top probe and Bottom probe.

The same analysis is done for the ion saturation signals at Top and Radial 2 (Fig. 10.9). Fig. 10.9.d shows the raw signals and the time window. The dominant peak in cross spectral density and coherence is found around 30 kHz (Fig. 10.9.a and .b). The corresponding phase is nearly -0.5π (Fig. 10.9.c). Together with the phase between ion saturation current signals at Top probe and Bottom probe, this implies the poloidal mode number $m = 1$.

As for the toroidal number of the 30 kHz mode in ion saturation current signals, it was difficult to explicitly determine the toroidal number since the normalized spectral power densities at Raidial 1 and 2 are both relatively low. A clearer determination of the toroidal number would be possible if there were more probe systems inserted in the toroidal location where Radial 1 is situated. In this experiment, however, the discussion on the toroidal mode number is confined to the fact that the power spectral densities at Radial 1 and Radial 2 were both low. This implies that the $sin\theta$ dependence of ion saturation current (or density) fluctuation may also be the case for the toroidal location where Radial 1 probe is located.

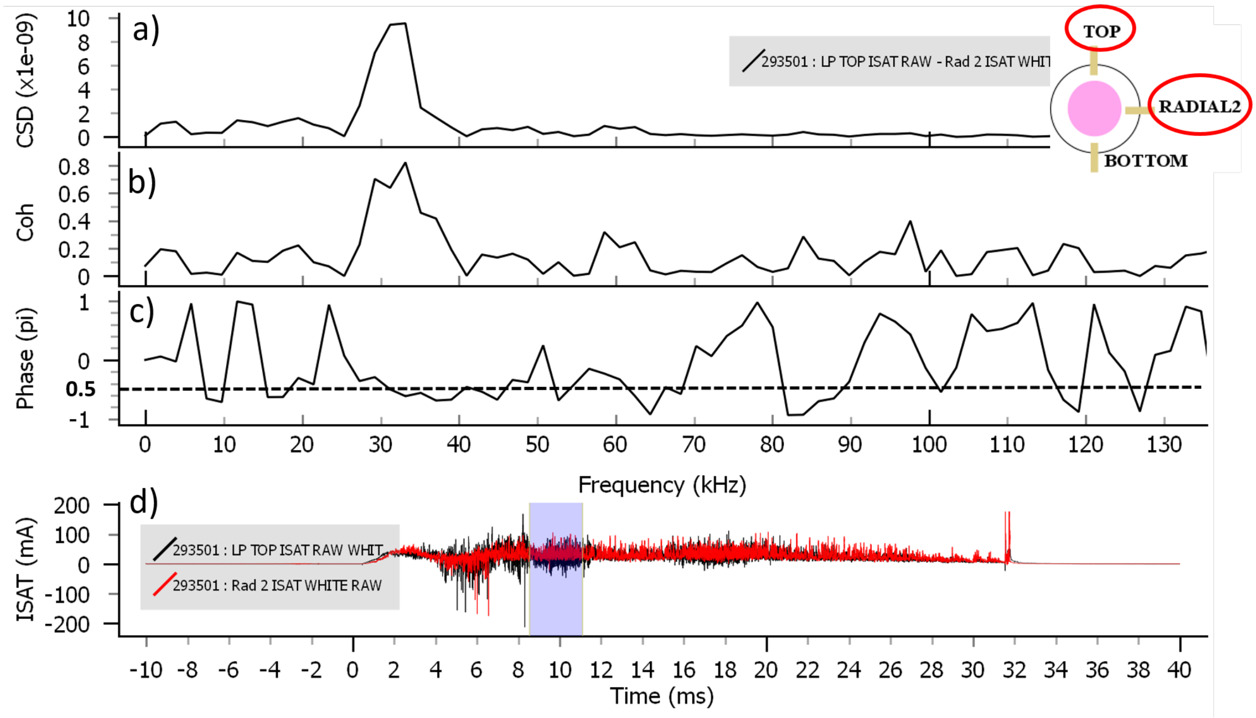

Figure 10.9: Cross spectral analysis of ion saturation current between Top and Radial 2.

10.2.2 Spectral Analysis for Floating Potential

This subsection shows the spectral analysis for the floating potential signals for the time period of interest, i.e., around 9 ms. The power spectral densities of floating at the four probe locations are shown in Fig. 10.10. The same time window was taken for calculating the power spectral densities (Fig. 10.10.a). Though not dominant, local peaks are found around 30 kHz (Fig. 10.10.b). A zoomed picture (Fig. 10.10.c) shows a profile similar to that in Fig. 10.6.c, though the density at Radial 2 is not significantly lower than those at Tom or Bottom.

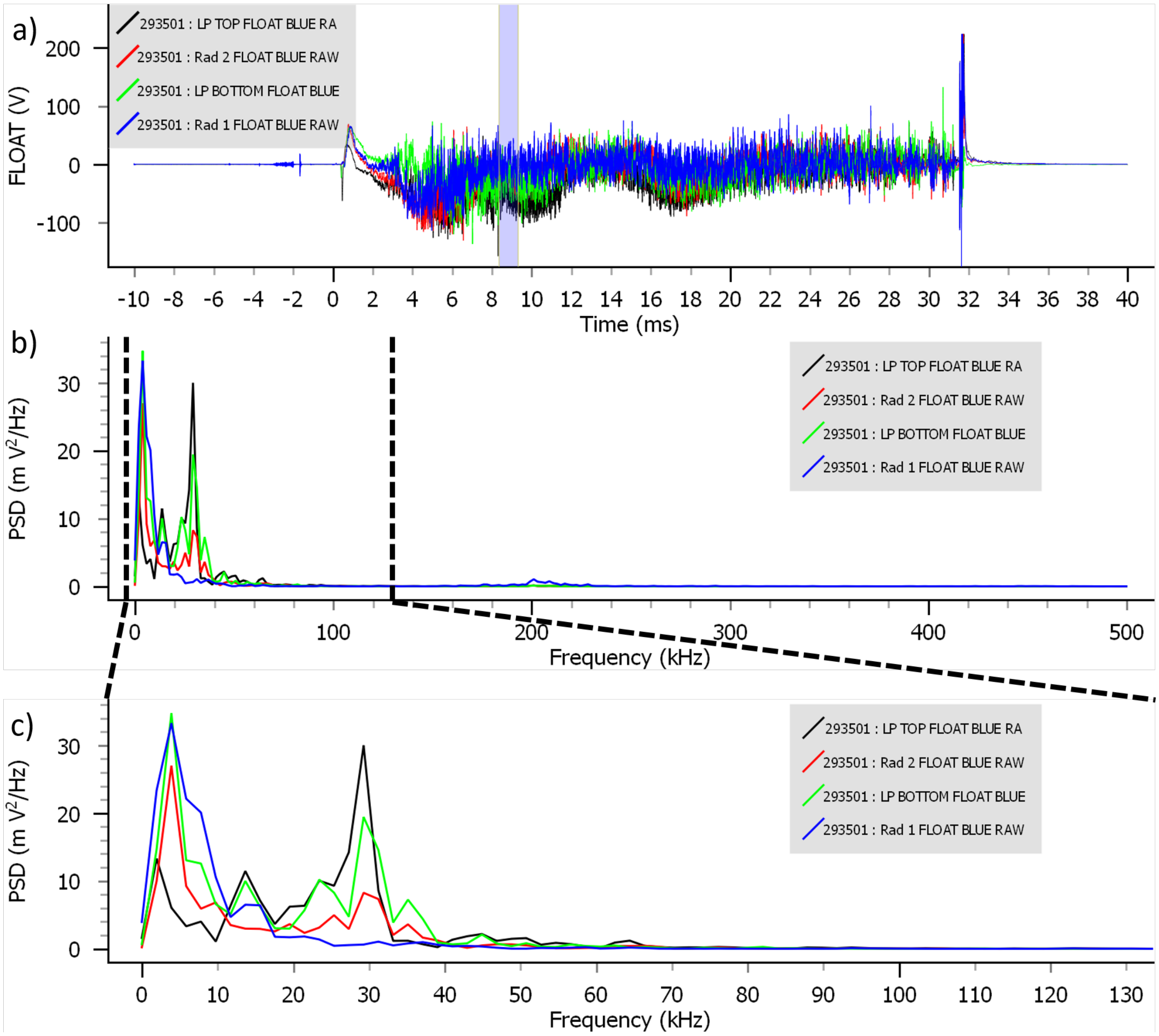

Figure 10.10: Power spectral density of floating potential at the four locations.

The cross spectral analysis for the floating potential signals at Tom and Bottom is shown in Fig. 10.11. The same time window as in Fig. 10.8.d was selected (Fig. 10.11.d). The dominant peak around 30 kHz was found in the cross spectral density (Fig. 10.11.a) and in coherence (Fig. 10.11.b). The corresponding phase was nearly 09π (Fig. 10.11.c), which suggests the poloidal mode number of $m = 1, 3, 5, ...$ This is not what one would expect from GAM oscillation as floating potential in GAM is expected to have a poloidal mode number of $m = 0$. This could be a due to drift mode, which is characterized by poloidal mode numbers

1 or higher. Another explanation would be the noise. Compared to the measurement of ion saturation current, measuring floating potential was subject higher noise because of the high impedance to satisfy the condition of $I_{probe} \simeq 0$. In The resistor values in Fig. 9.2 are set as low as possible without compromising the above condition. However, the signal-to-noise ratio for the floating potential was still high compared to that in measurements of ion saturation current.

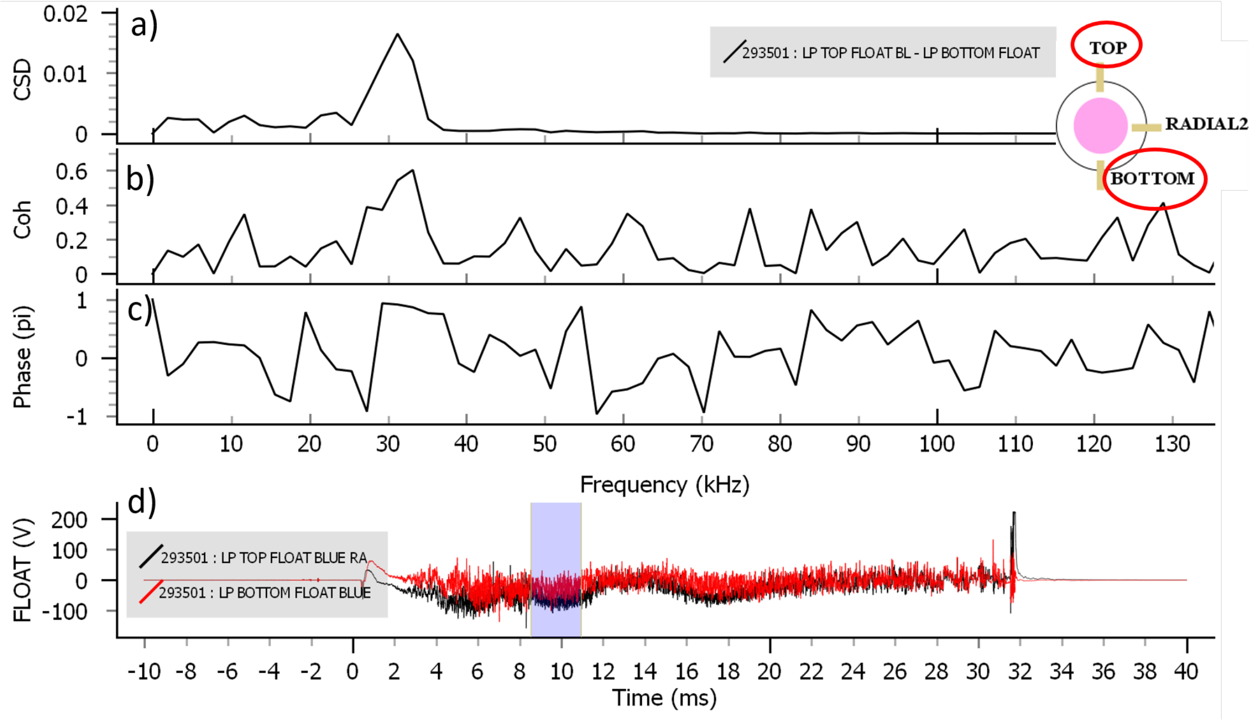

Figure 10.11: Cross spectral analysis of floating potential between Top probe and Bottom probe.

10.3 Comparison with Theoretical GAM Frequency

The last section showed that there was a local peak around 30 kHz in both ion saturation current and floating potential signals in the time window around 9 ms. To compared with this frequency to the theoretical values, this section shows the electron temperature obtained from the I-V characteristic curve. Since there was no I-V characteristic measurement taken in the discharge (# 293501) for which the above analyses were made, we chose a discharge (# 293644) with similar parameters. Moreover, it was difficult to apply the sweeping voltage at multiple locations as doing so shortened the discharges. Therefore, we took a I-V characteristics measurement at Radial 2 probe, where the measurement did not cause a significant effect on the plasma.

The signals (smoothed over 0.1 ms) of probe voltage and current signals, obtained from the apparatus shown in Fig. 9.4, are shown in Fig. 10.12. The sweeping frequency was 500 Hz, which produced a pair of I-V characteristic curves in 2 ms. We chose the time window for which the signature of GAM was often observed (in blue) and calculated the electron temperature according to Eq. 6.4.4. The resulting electron temperature turned out to be $T_e \simeq 23$ eV, which is a reasonable value for the edge of the plasma discharge in the STOR-M tokamak.

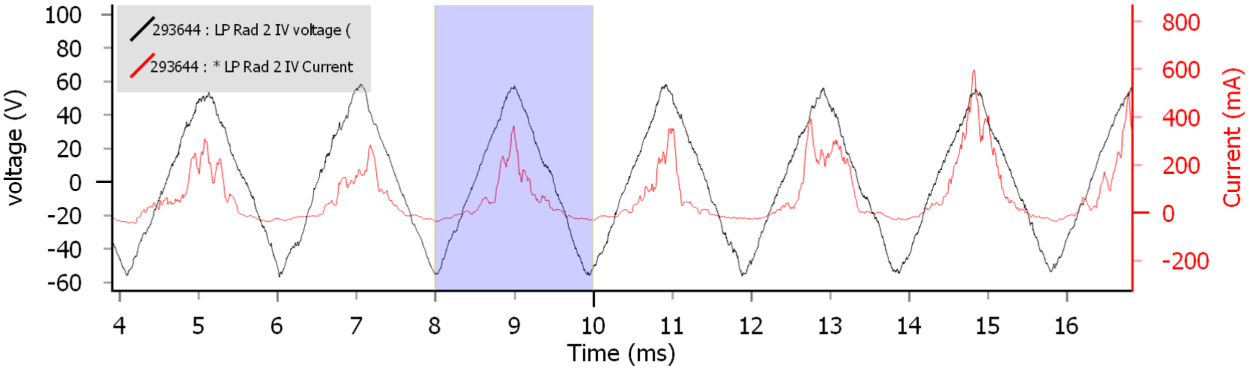

Figure 10.12: Smoothed (over 0.1 ms) signals of probe current and voltage for electron temperature measurement.

Based on the electron temperature obtained from the I-V characteristics, we calculated the theoretical GAM frequencies, both in fluid and kinetic models. In calculating the frequency, some assumptions were made. First, the ion temperature was assumed to be same was the electron temperature. Second, q at the edge in the STOR-M tokamak was assumed to be $q \gg 1$. Lastly, the ion acoustic speed was expressed as $C_s = \sqrt{(T_e + T_i)/m_i}$. Based on the above assumptions, the theoretical GAM frequency is

$$f_{GAM1} = \frac{C_s}{2\pi R}\sqrt{2 + \frac{1}{q^2}} \simeq \frac{\sqrt{2(T_e + T_i)/m_i}}{2\pi R} = 33 \text{ kHz} \tag{10.3.1}$$

in the fluid model (Eq. 4.3.20). According to the kinetic model (Eq. 10.3.2), the predicted GAM frequency is

$$f_{GAM2} = \frac{\sqrt{2\left(T_e + \frac{7}{4}T_i\right)/m_i}}{2\pi R} = 38\text{ kHz} \tag{10.3.2}$$

Accordingly, the frequency of the oscillation found in the experiment seems to match with the GAM frequency based on the fluid model. This is another indication that the oscillation found can be GAM.

Chapter 11

Conclusion and Future Work

The aim of our study was to experimentally detect GAM in the STOR-M tokamak. This chapter makes conclusions from the results and indicates future works that should follow this study.

11.1 Conclusions

In our experimental studies, we used a set of Langmuir probes in order observe a potential GAM in plasmas created in the STOR-M tokamak. The probe locations were adjusted such that ion saturation current signals at the different probe locations were similar. At these locations we measured floating potential and ion saturation current. Around 9 ms, which is the end of ramp-up region and the beginning of the flat-top region, we found a dominant peak around 30 kHz in the power spectral densities of ion saturation current. The ion saturation current signals showed the $sin\theta$ dependence of the oscillation amplitude, which is one of the characteristics of GAM. Furthermore, the cross spectral analysis on the ion saturation current signals suggested the poloidal mode number of $m = 1$. As for the floating potential signals, while 30 kHz peak was present around 9 ms, the cross spectral analysis indicated the poloidal mode number of $m = 1$, which is not expected for GAM. In comparison to the theoretical calculations of GAM frequency, the frequency predicted by the fluid model matched with the experimental results. Based on the above findings, it is concluded that the plasmas in the STOR-M tokamak has a signature of GAM. A further investigation can lead to a more definitive identification of GAM.

11.2 Future Work

Our experimental study indicated the signature of GAM in the STOR-M tokamak. In order to verify its existence more definitively, however, further efforts must be made. First, it was difficult to study the toroidal mode number of the oscillation as the amplitudes of the oscillation at the radial locations were low. In order to overcome this problem, there needs to be more Langmuir probes, preferably located at the top and bottom in a poloidal plane at another toroidal location. This would help identify the toroidal mode number.

Second, flow measurement in addition to probe measurements will confirm the existence of GAM. GAM is characterized by a oscillating poloidal flow due to $\mathbf{E} \times \mathbf{B}$ drift. A diagnostics techniques for flow measurement such as Mach probes will contribute to detecting the oscillating flow.

Third, noise must be reduced. In this study, we struggled with noise in the Langmuir probe measurements, particularly for floating potential. Improving the signal-to-noise ratio would show clearer picture of the mode.

Chapter 12

Bibliography

[1] International Energy Agency, "Key World Energy Statistics 2014." http://www.iea.org/publications/freepublications/publication/keyworld2014.pdf, 2014.

[2] U.S. Energy Information Administration, "International Energy Outlook 2014." http://www.eia.gov/forecasts/ieo/pdf/0484%282014%29.pdf, 2014.

[3] Rajendra Pachauri et al., "Climate Change 2014 Synthesis Report." https://www.ipcc.ch/pdf/assessment-report/ar5/syr/SYR_AR5_FINAL_full.pdf, 2014.

[4] J.-L. Basdevant, J. Rich, and M. Spiro, *Fundamentals In Nuclear Physics*. New York: Springer-Verlag, 2005.

[5] G. McCracken and P. Stott, *Fusion: The Energy of theUniverse*. ACADEMIC PRESS, 2005.

[6] D. Bodansky, *Nuclear energy principles, practices, and prospects*. Springer, 2004.

[7] J. Mahaffey, *Atomic Accidents: A History Of Nuclear Meltdowns And Disasters*. Pegasus Books, 2014.

[8] J. P. Freidberg, *Plasma Physics and Fusion Energy*. Cambridge University Press, 1st ed., Feb. 2007.

[9] J. Wesson, *Tokamaks*. Oxford; New York: Oxford University Press, 4th ed., Nov. 2011.

[10] F. F. Chen, *An Indispensable Truth: How Fusion Power Can Save the Planet*. Springer, 2011.

[11] Culham Centre for Fusion Energy, "Jet." http://www.ccfe.ac.uk/jet.aspx, Jul 2012.

[12] ITER, "Progress in fusion." https://www.iter.org/sci/beyonditer, May 2015.

[13] I. Caldas, F. Marcus, A. Batista, R. Viana, S. Lopes, M. Heller, Z. Guimaraes-Filho, P. Morrison, and W. Horton, "Turbulence induced transport in tokamaks," in *Plasma and Fusion Science(AIP Conference Proceedings Volume 875)*, vol. 875, pp. 341–346, 2006.

[14] N. Winsor, J. L. Johnson, and J. M. Dawson, "Geodesic acoustic waves in hydromagnetic systems," *Physics of Fluids (1958-1988)*, vol. 11, no. 11, pp. 2448–2450, 1968.

[15] A. Fujisawa, T. Ido, A. Shimizu, S. Okamura, K. Matsuoka, H. Iguchi, Y. Hamada, H. Nakano, S. Ohshima, K. Itoh, and others, "Experimental progress on zonal flow physics in toroidal plasmas," *Nuclear Fusion*, vol. 47, no. 10, p. S718, 2007.

[16] J. A. Bittencourt, *Fundamentals of Plasma Physics*. New York: Springer, 3rd ed., June 2004.

[17] J. P. Freidberg, *Ideal MHD*. New York: Cambridge University Press, Aug. 2014.

[18] F. F. Chen, *Introduction to Plasma Physics and Controlled Fusion: Volume 1: Plasma Physics*. New York: Springer, 2nd ed., May 2006.

[19] A. Hirose, "Note 6: Drift mode." University Lecture, University of Saskatchewan, 2015.

[20] A. Hirose, "Note 7: Itg mode." University Lecture, University of Saskatchewan, 2015.

[21] P. Diamond, S. Itoh, K. Itoh, and T. Hahm, "Zonal flows in plasma," *Plasma Physics and Controlled Fusion*, vol. 47, no. 5, p. R35, 2005.

[22] T. S. Hahm, K. Burrell, Z. Lin, R. Nazikian, and E. Synakowski, "Zonal flow measurements concept i," *Plasma Physics and Controlled Fusion*, vol. 42, no. 5A, p. A205, 2000.

[23] A. Hirose, "Plasma waves note 8: Geodesic acoustic mode." University Lecture, University of Saskatchewan, 2013.

[24] G. Wang, W. Peebles, T. Rhodes, M. Austin, Z. Yan, G. McKee, R. La Haye, K. Burrell, E. Doyle, J. Hillesheim, *et al.*, "Multi-field characteristics and eigenmode spatial structure of geodesic acoustic modes in diii-d l-mode plasmas," *Physics of Plasmas (1994-present)*, vol. 20, no. 9, p. 092501, 2013.

[25] M. Shats and W. Solomon, "Experimental evidence of self-regulation of fluctuations by time-varying flows," *Physical review letters*, vol. 88, no. 4, p. 045001, 2002.

[26] Y. Nagashima, K. Itoh, S. Itoh, K. Hoshino, A. Fujisawa, A. Ejiri, Y. Takase, M. Yagi, K. Shinohara, K. Uehara, *et al.*, "Observation of coherent bicoherence and biphase in potential fluctuations around geodesic acoustic mode frequency on jft-2m," *Plasma physics and controlled fusion*, vol. 48, no. 5A, p. A377, 2006.

[27] G. R. McKee, R. J. Fonck, M. Jakubowski, K. H. Burrell, K. Hallatschek, R. A. Moyer, D. L. Rudakov, W. Nevins, G. D. Porter, P. Schoch, *et al.*, "Experimental characterization of coherent, radially-sheared zonal flows in the diii-d tokamak," *Physics of Plasmas (1994-present)*, vol. 10, no. 5, pp. 1712–1719, 2003.

[28] K. Zhao, J. Dong, L. Yan, W. Hong, T. Lan, A. Liu, J. Qian, J. Cheng, D. Yu, Y. Huang, *et al.*, "Characteristics of geodesic acoustic mode zonal flow and ambient turbulence at the edge of the hl-2a tokamak plasmas," *Physics of Plasmas (1994-present)*, vol. 14, no. 12, p. 122301, 2007.

[29] T. Lan, J. Wu, H. Shen, T. Deng, A. Liu, J. Xie, H. Li, W. Liu, C. Yu, Y. Sun, *et al.*, "The measurement of geodesic acoustic mode magnetic field oscillations in j-text tokamak," in *APS Meeting Abstracts*, vol. 1, p. 3003, 2014.

[30] J. Hillesheim, W. Peebles, T. Carter, L. Schmitz, and T. Rhodes, "Experimental investigation of geodesic acoustic mode spatial structure, intermittency, and interaction with turbulence in the diii-d tokamak," *Physics of Plasmas (1994-present)*, vol. 19, no. 2, p. 022301, 2012.

[31] Z. Gao, “Collisional damping of the geodesic acoustic mode,” *Physics of Plasmas (1994-present)*, vol. 20, no. 3, p. 032501, 2013.

[32] Z. Qiu, L. Chen, and F. Zonca, “Nonlinear excitation of geodesic acoustic mode by collisionless trapped electron mode,” *Nuclear Fusion*, vol. 54, no. 3, p. 033010, 2014.

[33] M. Hubeny, “Edge plasma properties of ohmic discharges with resonant magnetic perturbations in the stor-m tokamak,” Master’s thesis, University of Saskatchewan, 2012.

[34] Y. Ding, “Investigation of resistive geodesic acoustic mode in the edge of stor-m tokamak,” Master’s thesis, University of Saskatchewan, 2013.

[35] “Progress report,” tech. rep., Plasma Physics Laboratory, University of Saskathcewan, Saskatoon, Saskatchewan, 1996.

[36] W. Zhang, C. Xiao, and A. Hirose, “Plasma autobiasing during ohmic h-mode in the stor-m tokamak,” *Physics of Fluids B: Plasma Physics (1989-1993)*, vol. 5, no. 11, pp. 3961–3968, 1993.

[37] O. Mitarai, A. Hirose, and H. M. Skarsgard, “Ignition access condition based on the generalized saddle point in a magnetic fusion reactor,” *Fusion Science and Technology*, vol. 20, no. 2, pp. 208–221, 1991.

[38] S. Sen, C. Xiao, A. Hirose, and R. Cairns, “Role of parallel flow in the improved mode on the stor-m tokamak,” *Physical review letters*, vol. 88, no. 18, p. 185001, 2002.

[39] Y. Nagashima, K. Hoshino, A. Ejiri, K. Shinohara, Y. Takase, K. Tsuzuki, K. Uehara, H. Kawashima, H. Ogawa, T. Ido, and others, “Observation of nonlinear coupling between small-poloidal wave-number potential fluctuations and turbulent potential fluctuations in ohmically heated plasmas in the jft-2m tokamak,” *Physical review letters*, vol. 95, no. 9, p. 095002, 2005.

[40] I. H. Hutchinson, *Principles of Plasma Diagnostics.* Cambridge University Press, 2nd ed., 2005.

[41] W. A. Salem, “A first look at parital differential equations.” University Lecture, University of Saskatchewan, 2012.

[42] J. Proakis and D. Manolakis, *Digital Signal Processing*. Prentice Hall international editions, Pearson Prentice Hall, 2007.

[43] P. D. Welch, “The use of fast fourier transform for the estimation of power spectra: A method based on time averaging over short, modified periodograms,” *IEEE Transactions on audio and electroacoustics*, vol. 15, no. 2, pp. 70–73, 1967.

[44] H. Ott, *Electromagnetic Compatibility Engineering*. Wiley, 2011.

[45] Texas Instruments, *High Common-Mode Voltage Difference Amplifier*, 7 2012. Data Sheet.

[46] Avago Technology, *High-Linearity Analog Optocouplers*, 7 2014. Data Sheet.

[47] R. Taylor, M. Brown, B. Fried, H. Grote, J. Liberati, G. Morales, P. Pribyl, D. Darrow, and M. Ono, “H-mode behavior induced by cross-field currents in a tokamak,” *Physical review letters*, vol. 63, no. 21, p. 2365, 1989.

[48] R. Weynants, G. Van Oost, G. Bertschinger, J. Boedo, P. Brys, T. Delvigne, K. Dippel, F. Durodie, H. Euringer, K. Finken, *et al.*, “Confinement and profile changes induced by the presence of positive or negative radial electric fields in the edge of the textor tokamak,” *Nuclear Fusion*, vol. 32, no. 5, p. 837, 1992.

[49] C. Xiao and A. Hirose, “The role of plasma biasing in the h-modes in the stor-m tokamak,” *Contributions to Plasma Physics*, vol. 40, no. 1-2, pp. 184–189, 2000.

[50] Riverbank Computing Limited, “What is pyqt?.” `https://riverbankcomputing.com/software/pyqt/intro`, 2016.

[51] Luke Campagnola, “Pyqtgraph - scientific graphics and gui library for python.” `http://www.pyqtgraph.org/`, 2011.